UNIVERSIDADE FEDERAL DO CEARÁ
CENTRO DE TECNOLOGIA
DEPARTAMENTO DE ENGENHARIA METALÚRGICA E DE MATERIAIS
PROGRAMA DE PÓS-GRADUAÇÃO EM ENGENHARIA E CIÊNCIA DE MATERIAIS

EMERSON EDILSON BARROS DE SOUZA

MODELLING AND SIMULATION OF COKE AND PCI COMBUSTION IN AN INDUSTRIAL BLAST FURNACE RACEWAY

FORTALEZA

2020

EMERSON EDILSON BARROS DE SOUZA

MODELLING AND SIMULATION OF COKE AND PCI COMBUSTION IN AN INDUSTRIAL BLAST FURNACE RACEWAY

Dissertação submetida ao Programa de Pós-Graduação em Engenharia e Ciência de Materiais da Universidade Federal do Ceará como requisito parcial à obtenção do título de Mestre em Engenharia e Ciência de Materiais. Área de Concentração: Processos de transformação e degradação dos materiais.

Orientador: Prof. Dr. Francisco Marcondes

Fortaleza

2020

Dados Internacionais de Catalogação na Publicação
Universidade Federal do Ceará
Biblioteca Universitária
Gerada automaticamente pelo módulo Catalog, mediante os dados fornecidos pelo(a) autor(a)

D32m de Souza, Emerson Edilson Barros.
MODELLING AND SIMULATION OF COKE AND PCI COMBUSTION IN AN INDUSTRIAL BLAST FURNACE RACEWAY / Emerson Edilson Barros de Souza. – 2021.
142 f. : il. color.

Dissertação (mestrado) – Universidade Federal do Ceará, Centro de Tecnologia, Programa de Pós-Graduação em Engenharia e Ciência de Materiais, Fortaleza, 2021.
Orientação: Prof. Dr. Francisco Marcondes.

1. Raceway. 2. Combustão. 3. Coque. 4. Carvão Pulverizado. 5. Taxa de Reação. I. Título.
CDD 620.11

EMERSON EDILSON BARROS DE SOUZA

MODELLING AND SIMULATION OF COKE AND PCI COMBUSTION IN AN INDUSTRIAL BLAST FURNACE RACEWAY

Dissertação submetida ao Programa de Pós-Graduação em Engenharia e Ciência de Materiais da Universidade Federal do Ceará como requisito parcial à obtenção do título de Mestre em Engenharia e Ciência de Materiais. Área de Concentração: Processos de transformação e degradação dos materiais.

Aprovada em: 18/03/2020.

BANCA EXAMINADORA

_____

Prof. Dr. Francisco Marcondes (Orientador)
Universidade Federal do Ceará (UFC)

_____

Prof. Dr. José Adilson de Castro
Universidade Federal Fluminense (UFF)

_____

Prof. Dr. Janaína Gonçalves Maria da Silva Machado
Universidade Federal do Ceará (UFC)

To my parents

ACKNOWLEDGEMENTS

I would like to thank my family, my parents Francisca Ribeiro and Francisco Ediuson for their support in every step of my life, without their guidance and foundation nothing would be possible. Special thanks to my girlfriend Ana Olivia Viana, for which partnership, advice, and support during the bad and good moments were fundamental.

I am very grateful to my supervisor, Francisco Marcondes, with whom I had the opportunity to work. His fundamental experience during this research, advice, support, help during my internship and review of this text, and all his collaboration during the development of this thesis. To professor José Adilson, who always answered all my doubts no matter the time, always being very kind and professional during all the phases of this study. To professors Cleiton Carvalho and Janaina Machado, who great help allowed me to develop my internship, giving support until the end.

To my coworkers that became friends during my internship, Gabriel Aranha, Diego Vieira, Rodolfo Ferreira, Pietro Cosentino, and Michel Lima, for their support, work discussions, advice, and friendship.

To my friends from the Computational Fluid Dynamics Laboratory (LDFC), Edilson Drummond, Ivens Costa, João Henrique, José Renê, Marcelo Menezes, Paulo Pimenta, who are excellent researches and great people and with who I had the opportunity to work and learn with. To all my friends from the department who were always present to give me support in anything that I need.

I must acknowledge the financial support provided by CNPq (The National Council of Technological and Scientific Development) to this research.

RESUMO

O alto-forno, caracterizado como um reator metalúrgico contracorrente, é o processo mais utilizado para a produção de ferro primário, ferro-gusa, no mundo. Em seu interior, o minério de ferro e os fluxos reagem entre si, formando ferro-gusa líquido e escória por meio de reações com os gases provenientes da combustão do coque, a principal fonte de combustível usada no processo. Como material indispensável na produção de energia química do forno, o coque se torna um fator importante no processo, interferindo diretamente tanto na composição final do ferro-gusa quanto no custo final do equipamento. Com isso em mente, o processo de injeção de carvão pulverizado é uma alternativa já usada pela maioria das indústrias siderúrgicas na redução de custos com coque. Para melhorar esse processo complexo, que envolve reações químicas, transferência de calor, transformação de fase e fluxo em altas temperaturas e velocidades, a Dinâmica dos Fluidos Computacional, um método consolidado de simulação de problemas de engenharia, tem uma base solida na análise de toda a cadeia de produção do alto-forno, agindo como uma ferramenta capaz de auxiliar a previsibilidade deste equipamento complexo. Neste estudo, as validações da formação de *raceway*, combustão de coque e carvão pulverizado foram estudadas e simuladas usando dados experimentais e numéricos da literatura. O software comercial ANSYS-FLUENT foi utilizado para resolver as equações de conservação que governam o problema. A combustão do coque e do carvão pulverizado foi simulada utilizando taxas de reação que consideraram a estrutura interna das partículas. As validações apresentaram resultados aceitáveis do ponto de vista de engenharia. Ao final, os modelos validados foram testados juntos utilizando condições de operação de um alto-forno retirados da literatura de um trabalho que utilizou modelo semelhante ao do presente estudo. Os resultados apresentados neste estudo cobriram as taxas de reação, campos de temperatura e escoamento, comportamento das partículas durante a combustão, e espécies químicas produzidas e consumidas durante o processo.

Palavras-chave: *Raceway*, Combustão, Coque, Carvão Pulverizado, Taxa de Reação.

ABSTRACT

The blast furnace, characterized as a countercurrent metallurgical reactor, is the most used process for the production of primary iron, pig iron, in the world. Inside it, iron ore and fluxes react with each other, forming liquid pig iron and slag through reactions with the gases that come from the combustion of coke, the main fuel source used in the process. As an indispensable material in the production of chemical energy of the furnace, coke becomes an important factor in the process, directly interfering both in the final composition of the pig iron and in the final cost of the equipment. With this in mind, the pulverized coal injection process comes as an alternative already used by most of the iron and steelmaking industries in reducing costs with coke. To understand this complex process, which involves chemical reactions, heat transfer, phase transformation, and flow at high temperatures and velocities, Computational Fluid Dynamics, a consolidated method of simulating engineering problems, has a solid base in the analyzes of all the blast furnace chain production, acting as a tool capable of assisting the predictability of this complex equipment. In this study, validations of the raceway formation, combustion of coke, and pulverized coal were studied and simulated using experimental and numerical data from the literature. The commercial software ANSYS-FLUENT was used to solve the conservation equations that govern the problem. The combustion models were simulated using kinetic reaction rates that considered the particle's internal structure. The validations presented acceptable results from an engineering view of point. In the end, the validated models were tested together using blast furnace operating conditions taken from a literature study that used a model similar to the one in the present work. The study will cover the reaction rates, temperature fields, flow fields, particle behavior during combustion, and chemical species produced and consumed during the process.

Keywords: Raceway, Combustion, Coke, Pulverized Coal, Reaction Rates.

LIST OF FIGURES

LIST OF TABLES

LIST OF SYMBOLS

Roman Symbols

a_1, a_2, a_3	Constants applied to the drag function
a	Arthur's constant
a	Absorbing coefficient [m^{-1}]
A	Pre-exponential factor [units vary]
A, B	Eddy Dissipation Model Empirical Constants
A_p	Surface area of the particle [m^2]
$c_{p,i}$	Specific heat of phase *i* [J/kg·K]
C_i	Species *i* concentration [kmol/m^3]
C	Linear anisotropic phase function coefficient
C_1, C_2	$k-\varepsilon$ Turbulence Model constants
$C_\mu, C_{1\varepsilon}, C_{3\varepsilon}$	$k-\varepsilon$ Turbulence Model constants
C_1	Diffusion rate coefficient [$m^3/K^{0.75}\cdot s$]
$\overline{d}$	Mean diameter [m]
$D_{m,i}$, $D_{T,i}$	thermal and mass diffusion coefficients for species *i*
D_0	Diffusion rate [m^2/s]
D_i^{eff}	Effective intra-particle diffusion coefficient for species *i* [m^2/s]
D_i^{bulk}	Bulk molecular diffusion coefficient [m^2/s]
$d_{lk}d_{kl}, d_{ij}$	Saffman deformation tensor [N/m^2]
E	Activation energy [J/kmol]
f_h	Fraction of heat absorbed by the particle
F_x	Additional forces term in particle force balance [N]
F_p	Sum of forces acting on a particle [N]
F_D	Drag force [N]
$\vec{F}$	Saffman lift force [N]

G_k	Generation of turbulence kinetic energy due to mean velocity gradients
G_b	Generation of turbulence kinetic energy due to buoyancy
G	Incident radiation [W/m^2]
$h_{f,i}$	Heat of formation of species i [J/kmol]
h_i	Enthalpy of phase i [J/kg]
h	Convective heat transfer coefficient [W/m^2·K]
H_{reac_r}	Enthalpy of reaction relative to reaction r [J/kg]
I	Radiative intensity [W/m^2·Sr]
l_e	Turbulent eddy length scale [m]
$\overrightarrow{J_i}$	Diffusion flux of specie i [kg/m^2·s]
k	Turbulent kinetic energy [J/kg or m^2/s^2]
k	Chemical reaction rate
k_B	Stefan-Boltzmann constant [5.67 × 10^{-8} W/m^2·K^4]
k_i	Thermal conductivity of phase i [W/m·K]
k_i	Kinetic rate constant of species i [various]
K	Saffman force constant
m_v	Volatile yield [kg]
$m_{p,0}$	Initial particle mass [kg]
m_a	Ash mass [kg]
$M_{w,i}$	Molecular weight of species i [kg/kmol]
M_i	Molecular Weight [kg/kmol]
n	Refractive index
N_g	Number of species in the gas phase
N	Apparent order of reaction
Nu	Nusselt number
N_R	Total number of reactions
P_n	Bulk partial pressure [Pa]

P_i	Partial pressure of specie *i* [-]
Pr	Prandtl number
Q_R	Radiative heat flux energy [W/m^2]
Q_{gs} , Q_{sg}	Heat exchange between the gas phase and solid phase [W]
R	Universal gas constant [J/kmol·K] [cm^3·atm/K·kmol]
R_i	Total rate of production of species *i* [kmol/m^3·s]
R_i	Reaction rate for reaction *i* [(kmol/m^3·s)]
R_i	Rate of particle surface species depletion [kg/s]
R_{Fr}	Finite Rate model reaction rate [kmol/m^3·s]
R_{Edd}	Eddy Dissipation Model reaction rate [kmol/m^3·s]
$R_{i,r}$	Net rate of production of species *i* [kmol/m^3·s]
$R_{i,r}$	Rate of particle species depletion [kg/m^2·s]
$\hat{R}_{i,r}$	Molar rate of creation/destruction of species *i* in reaction *r* [kmol/s]
S , S_{ij} , S_{ji}	Mean strain rates
S_ϕ , S_k , S_ε , S_{gs}	Source Term
S_i	Rate of creation of species *i* relative to the discrete phase
Sc	Schmidt number
Sh	Sherwood number
T	Temperature [K]
T_L	Fluid Lagrangian integral time [s]
u_p	Particle Velocity [m/s]
u	Velocity [m/s]
$\overline{u}$, u'	Mean and fluctuating velocity components [m/s]
v	Saffman kinetic viscosity [kg/m·s]
$v'_{i,r}$, $v''_{i,r}$	Stoichiometric coefficient for reactant *i*, in the reaction *r*
V_i	Specific volume of phase *i* [m^3]
Y_i	Mass fraction of species *i*

Y_d	Mass fraction of the particles greater than *d*
Y_M	Dissipation rate due to fluctuating dilatation in compressible flow

Greek Symbols

α	Spread parameter
α_i	Volume fraction of phase *i*
β	Temperature exponent
ε	Turbulence dissipation rate [m^2/s^3]
ε_p	Particle emissivity
ϕ	Flow variable [units vary]
ϕ_i	mass fraction of chemical species *i*
φ_i	Particle *i* shape factor
Γ	Diffusion coefficient
Γ_ϕ	Diffusion coefficient of the flow property [units vary]
η	Effectiveness factor
μ	Viscosity [kg/m·s]
μ_t	Turbulent viscosity [kg/m·s]
θ_R	Radiation temperature [K]
Θ	Thiele modulus
ρ_p	Density [kg/m^3]
$\hat{\rho}_i$	Effective density of phase *i* [kg/m^3]
σ_s	Scattering coefficient [m^{-1}]
σ_ε	Turbulent Prandtl number for ε
σ_k	Turbulent Prandtl number for *k*
τ_{cross}	Time for one particle to cross an eddy [s]
τ_p	Particle relaxation time [s]
τ_e	Turbulent eddy lifetime [s]
τ_i	Particle *i* pore tortuosity (*i* = coke or coal)

ζ	Normal distribution random number
ξ_i	Particle *i* porosity (*i* = coke or coal)
Ω	Solid angle [Sr]
Ω_{ij}	Diffusion collision integral of species *i* and *j*

Subscripts	
i	Species or phase
p	Particle
g	Gas
s	Solid
r	Reaction
Edd	Eddy Dissipation Model
Fr	Finite Rate model
ave	Average

LIST OF ABBREVIATIONS

CFD	Computational Fluid Dynamics.
CNPq	National Council of Technological and Scientific Development (Conselho Nacional de Desenvolvimento Científico e Tecnológico)
SEDEX	Foreigner Trade Secretariat (Secretaria de Comércio Exterior)
MDIC	Ministry of Economy (Ministério da Economia)
PCI	Pulverized Coal Injection
PC	Pulverized Coal
CSN	Companhia Siderurgica Nacional
CSP	Companhia Siderurgica do Pecém
VSB	Vallourec & Sumitomo Tubos do Brasil
RAFT	Raceway Adiabatic Flame Temperature
DPM	Discrete Particle Model
DEM	Discrete Element Method
HRA	Hydrogenous Reducing Agents
FVM	Finite Volume Method
DRW	Discrete Random Walk Model
RANS	Reynolds Averaged Navier-Stokes
RTE	Radiative Transport Equation
WSGGM	Weighted-Sum-of Gray-Gases Model
UDF	User-Defined Functions
COG	Coke Oven Gas

CONTENTS

1 INTRODUCTION

The blast furnace, responsible for reducing iron ore into hot metal, is the most traditional equipment in the manufacture of primary iron. The equipment is known as a process that produces/consumes a large number of resources, such as capital, due to the high investments required, raw material, given the exorbitant solid load it holds, and energy, by consuming and producing a large number of chemical reactions that occurs in its interior.

According to the 2020 Word Steel Association Report, Brazil is still in the 9th position on the rank of Major steel-producing countries in 2018 and 2019 with 32.2 million tons of crude steel production, behind countries like Turkey (1.5 million tons behind) and Germany (7.5 million tons behind), and above Iran, Italy and France in more than approximately 7 million tons. Brazil holds this position since 2004, with 32.9 million tons, when the position was taken by India with 38.1 million tons in 2004. It is proved that Brazil's position among the steel-producing countries has a global influence, and also, how stationary is its production since 2004, when the top countries like India (now second place with 111.2 million tons), Russia and South Korea, managed to increase their production.

Therefore, Brazil has a great potential to increase its participation in the global steel production, but of course, this improvement must be made strategically, considering the environmental and green economy new realities, which in practical terms, is the constant goal in emissions reduction and the materials reuse, a challenge especially for the iron and steel making (CAVALIERE, 2016).

To begin the study of how Brazil's steel capacity can be increased, it's convenient to look at its current state. Current Brazil's steel park mill can be seen in Figure 1.1.

Figure 1.1 – Brazil steel mill park

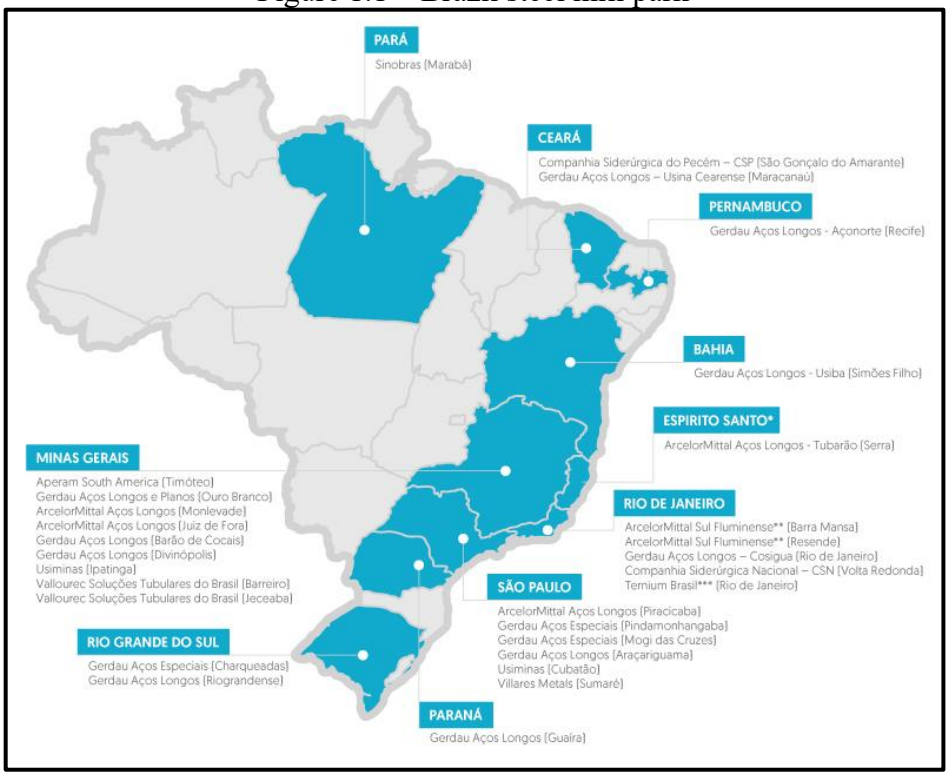

Source: BRASIL, 2018.

The Brazilian steel industry is represented by 14 private companies, controlled by 11 business groups, which operate 29 mills in 10 states (Brazil Steel Institute website). Recently, in 2017, the Ferroeste Group implemented the Green Long Steel Plant in Açailândia, Maranhão (which is not illustrated in Figure 1.1), giving Brazil 30 mills in total. One representation of such a steel park can be made in terms of the Foreign Trade Balance. Figure 1.2 illustrates the data up to 2019.

Figure 1.2 – Foreign Trade Balance of Steel Products

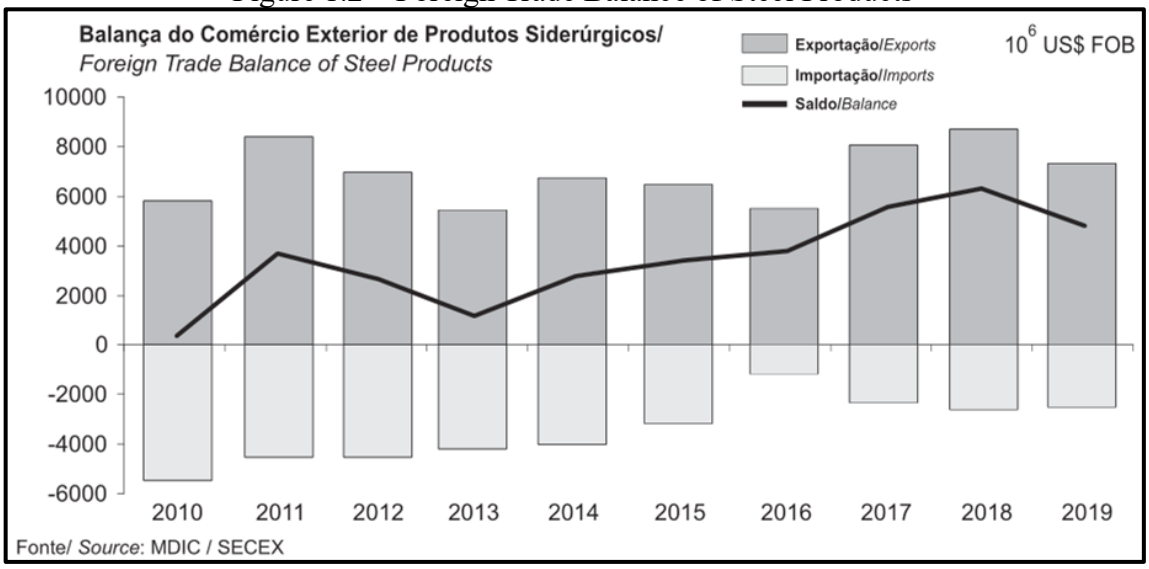

Source: BRASIL, 2020.

As one seen, on average, Brazil exports more than imports steel products. From 2013, exportations were in ramp-up, until it has an impact in 2019. Such exportations are mainly due to Semi-finished Products, more specifically slabs, responsible for in its majority to produce flat products (plates, sheets, shapes).

Now with a little understanding of the current steel mill park, one could start to look at improvement opportunities. With the semi-finished product's scenario in mind, to maintain the ramp-up exportations is important to have a good source of raw materials. In this case, in the integrated steel mills, where there is a blast furnace, the pig iron is the main source of iron for the slab's semi-finished product. The Brazilian total and by company production of pig iron from 2015 to 2019 can be seen in Table 1.

Table 1 – Brazil Pig Iron Production by Company from 2015 to 2019 (in 10^3 t)

Company	**2015**	**2016**	**2017**	**2018**	**2019**
Aço Verde Brasil	182	216	240	266	336
Aperam	473	500	452	462	454
ArcelorMittal Longos	1458	1451	1317	1474	1422
ArcelorMittal RJ	-	93	105	109	24
ArcelorMittal Tubarão	7406	7459	7487	7348	6613
CSN	4061	2951	4058	3787	2700
CSP		1295	2614	2967	2904
Gerdau	4475	4458	4385	4095	3807
Sinobras	122	121	122	112	134
Ternium Brasil	4366	4431	4519	4586	4384
Usiminas	4998	2999	2950	3100	3167
Vallourec	300	263	323	349	335
VSB	144	108	-	-	-
Total	**27985**	**26345**	**28572**	**28655**	**26280**

Source: BRASIL, 2020.

Brazil pig iron production has been following the same pattern from Figure 1.1, showing that the exportations are related to the blast furnace operations, with both indicators increasing from 2016 to 2018 and a strong decrease in 2019, related to the shutdown of Tubarão and CSN blast furnaces. The Brazilian ironmaking industry is also characterized by independent pig iron production, which has charcoal as its main fuel. Although not represented in the main

reports, is responsible on average for 4 thousand million tons from 2014 to 2018, absorbed mainly by domestic sales (SECRETARIA DE GEOLOGIA, 2019).

The blast furnace is a complex equipment that aggregates many processes, and because of that is a subject of continuous study. To cite, some of the challenges: control of the carbon footprint, make low iron ore grades economically viable, control hot metal silicon content, as the high-quality raw materials are becoming less and less available, cost of production, development of more efficient alternative ironmaking technologies, among many others. Filtering the alternatives, one can say that the recent research's main goals are concentrated in: decrease in coke use (coke rate), increase in productivity and efficiency, and reduction of dangerous emissions. In general, the blast furnace productivity depends on many parameters, and one that has a strong influence is the rate and degree of reduction, which is correlated to the coke reactivity and the burden composition.

Table 2 below depicts the coke rate and PCI usage in Brazil from 2014 to 2019.

Table 2 – Coke Rate and PCI in Blast Furnace (kg/t pig iron)

Input	**2014**	**2015**	**2016**	**2017**	**2018**	**2019**
Coke Rate	367	364	383	372	393	371
PCI (Pulverized coal Injection)	122	137	147	150	151	173

Source: BRASIL, 2020.

Table 2 shows that there is an increase in the use of the PCI (pulverized coal injection) in Brazil, which goes toward the technology update and global tendency of use of this fuel to reduce the coke rate.

The coke rate reduction is one of the actions that can be done to improve the competitiveness of the blast furnace process. From its extraction, during the mixture with other types of coals, to the coking stage at the coke oven station, the metallurgical coke is fundamental high-value fuel to the blast furnace process. The coke rate reduction tends in the long term to minimize environmental impacts, as it reduces CO_2 emissions (CAVALIERE, 2016). To balance the carbon source reduction, the pulverized coal is used and has been contributing to the coke economy in the last two decades, and efforts are made to increase its use worldwide.

According to past projections from the Steel Industry Technology Roadmap, in 2010, the pulverized coal that can be injected into the blast furnace has been limited to 113.4 to 136.07 kg/t of hot metal. The increase to 226.8 kg/t of hot metal would save 306 MJ/t of hot

metal of energy. One of the limitations is to increase the capacity of injection is the lack of precision of the prevision of the consequences. The report recommends that one way to overcome this lack of knowledge would be by the use of CFD models (Computer Fluid Dynamics) to simulate the PCI process and says that these initiatives are being made in cooperation with universities (VEHEC, 2010). Therefore, to understand the complex physical and chemical phenomena in the raceway zone and the PCI process, the CFD models are.

Computational Fluid Dynamics can be briefly defined as the use of numerical analysis and data structures to examine and solve problems that may include fluid flows, mass and heat transfer, turbulent regimes, radiation, chemical species in a vast variety of phenomena such as combustion. The problem solution is obtained in a computer simulation based on the approximate solution of governing equations (mass, momentum, energy, among other equations) after the definition of the boundary conditions. The CFD is a powerful tool due to its flexibility and viable cost-effectiveness, once experimental approaches can have high time/investment demand, hazardous conditions, and many other drawbacks. However, CFD cannot substitute the experiments but it can be used as a complementary tool to analyze complex problems, decreasing uncertainties, and give the first clue to a decision investment project.

The basic requirements to perform a CFD simulation are: problem design and geometry, the division of the domain in a mesh where the equations are going to be solved, approximate solution of the equations and results analysis, and visualization.

The present study will investigate the raceway cavity formation, coke, and pulverized coal combustions using the CFD simulation approach, by implementing a model formulation developed by DE CASTRO et al., 2011 in conjunction with the ANSYS-FLUENT software package, which will solve the flow equations that govern the physics of the problem.

2 OBJECTIVES

The present study objectives can be divided in:

2.1 General

Analysis and investigation of 3 blast furnace fundamental engineering process based on past literature experimental/numerical studies: raceway cavity formation using coke as a granular material, raceway combustion using coke as fuel material, pulverized coal injection combustion, and use the three models in one simulation using blast furnace boundary conditions.

2.2 Specifics

1. Validate the proposed model based on past literature results;
2. Adapt and apply a combustion model developed by DE CASTRO et al., 2011 to calculate coke and coal combustion reaction rates;
3. Present detailed analyzes of the simulations in terms of flow and temperature contour, turbulence field, reaction rates, species molar fraction, and particle variables.

3 LITERATURE REVIEW

3.1 Overview – the blast furnace

Blast furnaces are currently the main responsible for the production of pig iron (primary iron) and hot metal in the world. Figure 3.1 shows a schematic drawing of the blast furnace interior with some measurements.

Figure 3.1 – Structure of a blast furnace

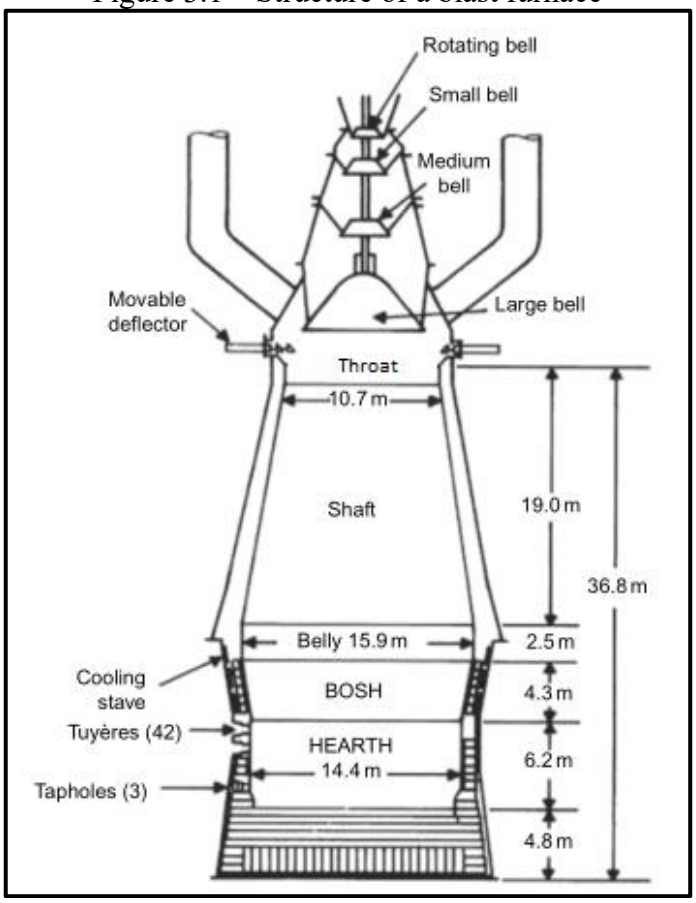

Source: SEETHARAMAN, 2013 (adapted).

The blast furnace is classified as a countercurrent reactor, where the gases rise through its interior while the load goes down all over the furnace. This metallurgical reactor has the objective of the production of the hot metal through the reduction of iron ore in the presence of coke or charcoal. Figure 3.2 provides an example of the blast furnace mass balance.

Figure 3.2 – Mass balance example used in an ironmaking blast furnace

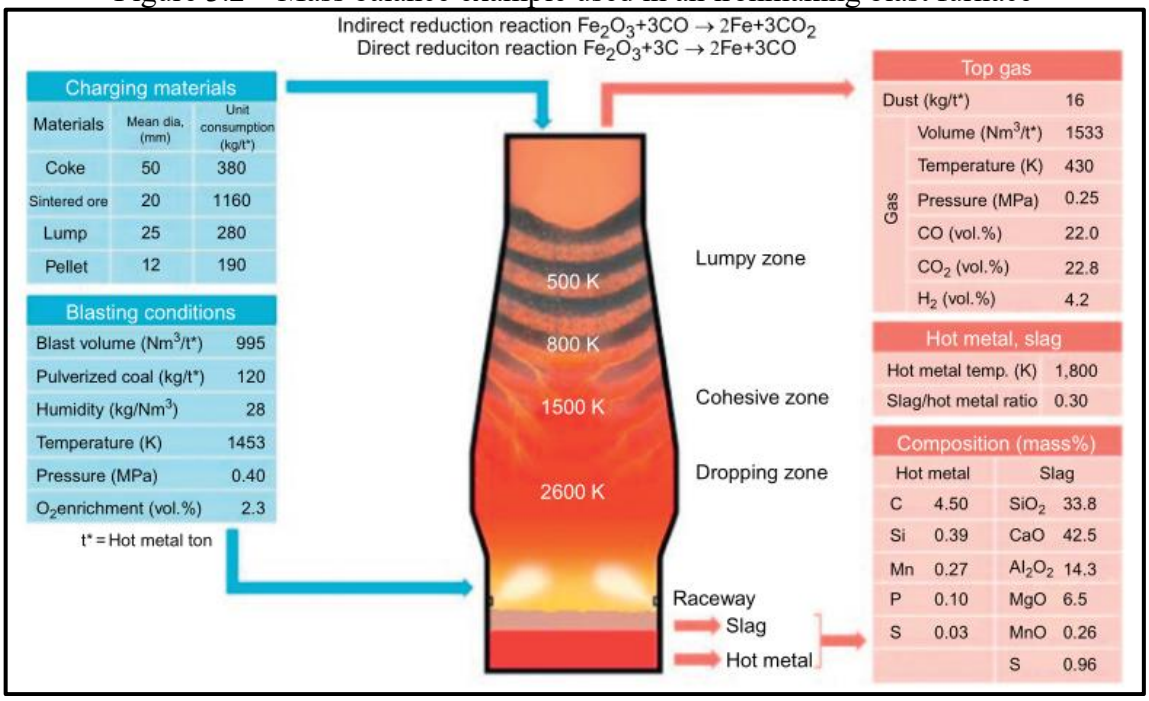

Source: SEETHARAMAN, 2013.

As can be seen in Figure 3.2, iron ore in sintered, lump and pellet forms, and metallurgical coke are loaded in alternate layers by the top of the furnace. These layers remain separated from each other until the heat and reducing gases supplied in the lower part of the furnace soften and melt the iron by chemical reactions and phase transformations. As a result, the main outputs obtained are the hot metal in the liquid phase, and the slag co-product. As the rector has a massive structure and a complex environment, during its process, the blast furnace can be divided into a series of zones with different temperatures and stages in which the burden can be found. Figure 3.3 below illustrates the main zones and Figure 3.4 the temperature profile.

Figure 3.3 – Zones in the blast furnace

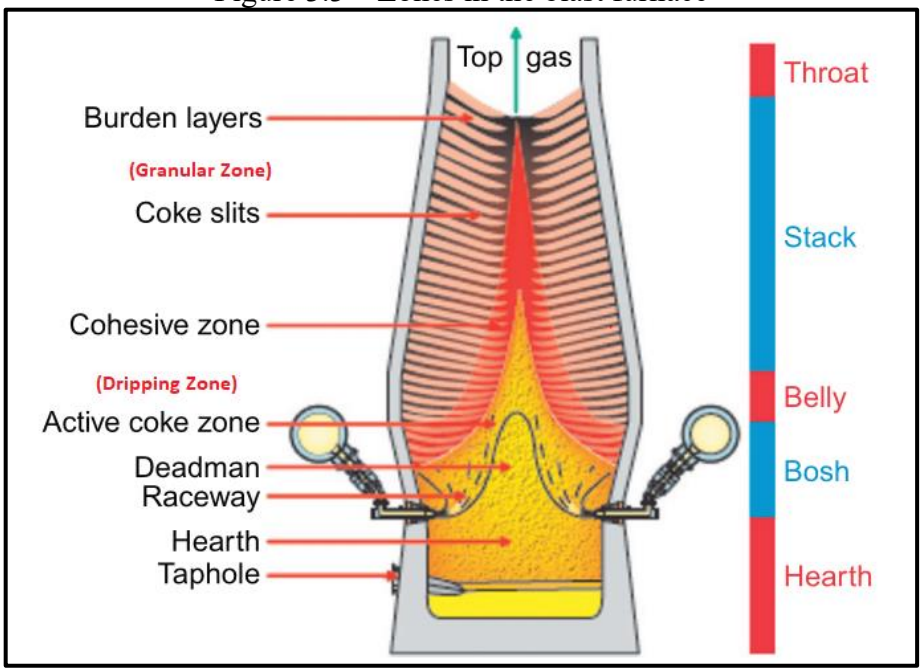

Source: GEERDES et al., 2015 (adapted).

Figure 3.4 – Temperature profile example in a blast furnace

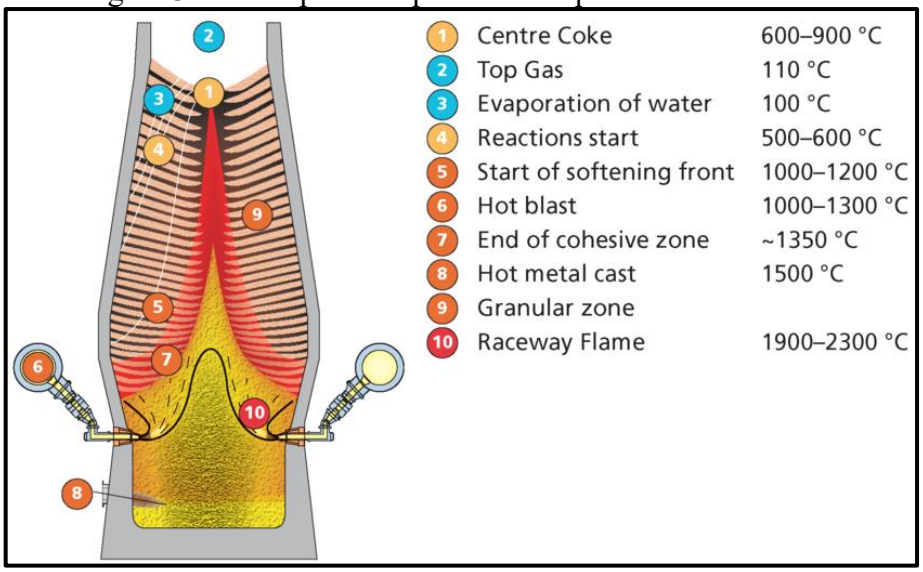

Source: GEERDES et al., 2015.

Observing the regions in Figure 3.3 and their temperature distribution in Figure 3.4, the main zones can be described as follows:

Granular Zone: where the burden remains solid and in a granular form organized in alternating layers. This zone is consumed as the materials keep descending to the lowers zones as the result of the softening/melting in the lower zones. Iron ore in this zone is being reduced (Fe_2O_3, Fe_3O_4, and FeO) due to the reactions with the gases (CO, CO_2, H_2, and H_2O), but remains in the solid state. The gases rise through the furnace thanks to the location, shape,

and extent of each zone, as well as the materials properties and their average size larger than the iron ore, thus providing a permeable bed.

Cohesive zone: where iron ore begins its process of softening-melting. This region has the most considerable resistance to the passage of gases since the burden is semi-fused, becoming cohesive and practically without porosity (impermeable). The permeability loss in the furnace causes the flow of the rising gases to be reduced, forcing them to continue around the cohesive layers until reaching the top regions. It also has the role of helping to withstand the load inside the oven, along with the structure of the walls.

Dripping Zone: a region with pre-formed liquid hot metal and slag flow between the solid reducer layers for deposition in the crucible, in the hearth zone. This zone is divided into two areas: active reducer (active coke) and the Deadman region. In such areas, the burden is composed mostly of coke. The portion of the reducer that moves towards the tuyere will be consumed by the combustion reactions, which will form the active coke region. The fraction of fuels in this zone that goes toward the tuyeres is deposited in column form above the slag and hot metal layers in the crucible.

Combustion Zone (Raceway): region right in front of the tuyeres where a cavity, partially empty, called raceway, extents due to the momentum created by the high flow rate blast injection and combustion reactions. In addition to the blast, pulverized coal (PC) and co-injection gases can also be used to enhance combustion. Figure 3.5 illustrates the lower zone of the blast furnace with PCI.

Figure 3.5 – The lower part of the blast furnace showing the combustion zone details

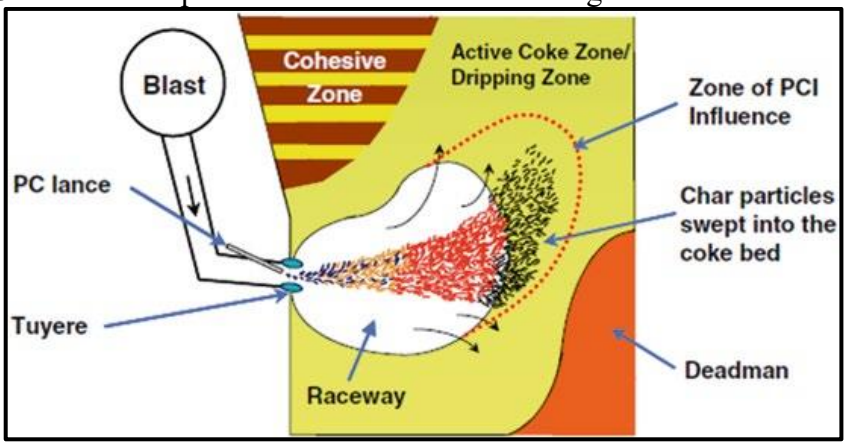

Source: CAVALIERE, 2016.

3.2 The raceway

The raceway cavity can be defined as a visible hot flame generated by the air blast that is blown into the blast furnace via the tuyeres at temperatures superior to 1250 °C. Figure 3.6 illustrates two views of the raceway.

Figure 3.6 – The raceway. Side view and an upper view of the blast furnace

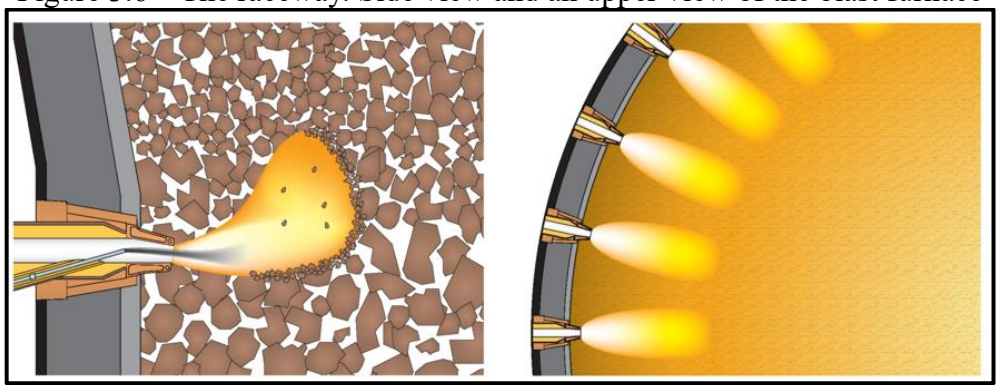

Source: GEERDES et al., 2015.

The coke particles near the raceway, observed on dissection of blast furnaces, in general, can be described as large diameters lumps just in front of the tuyere, surrounded by small coke particles. Further and below the small coke area, there is a space of low hollow made by coke dust of 5 mm or less, slag, and hot metal particles, with only big coke particles existing at the center of the furnace (JAPAN, 1987).

The temperature in these zones can reach the order of 2000 °C, which is difficult to measure without the proper considerations. To try to overcome this issue, a concept well accepted among the ironmaking community is the theoretical flame temperature, used as an indicator in blast furnace operations, Another concept is the raceway adiabatic flame temperature (RAFT) which is defined as the temperature that the raceway reaches as soon as all C, O_2, and H_2O are converted to CO and H_2 (CAVALIERE, 2016). These indicators can be calculated from a heat balance near the raceway using the blast conditions inputs in a theoretical expression, which as many versions (JAPAN, 1987).

Another way of quantitatively study the raceway region is to measure the gas composition generated by the reactions. In an operation that involves the PCI, Figure 3.7 illustrates the raceway cavity, a typical gas composition curve, and a coal particle reaction.

Figure 3.7 – Gas composition and PC particle reaction at the raceway

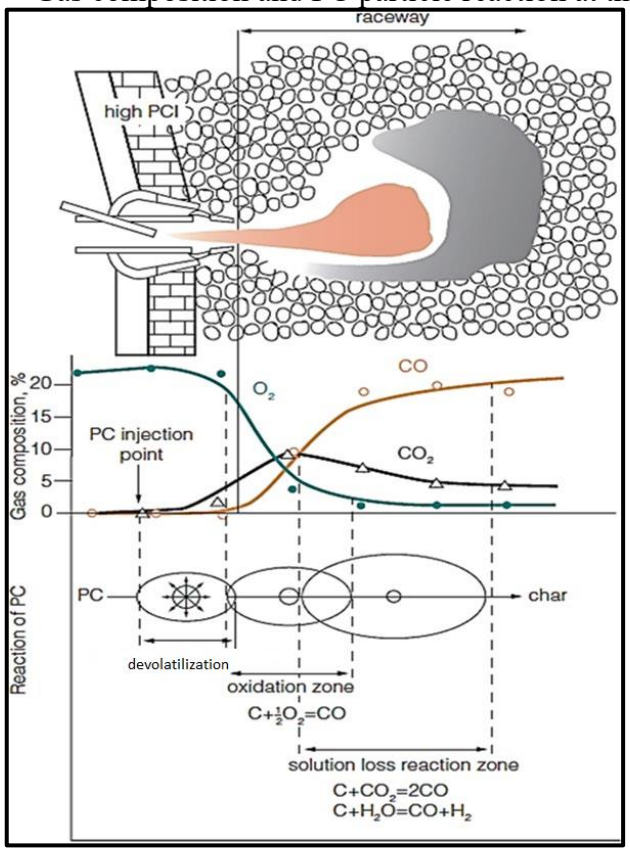

Source: CAVALIERE, 2016 (adapted).

The main reactions involving the carbon from coke and the coal, in this region, are:

(1) $C_{(s)} + O_{2(g)} \rightarrow CO_{2(g)}$ $\Delta H^0 = -393.5$ kJ/mol

(2) $C_{(s)} + 0.5O_{2(g)} \rightarrow CO_{(g)}$ $\Delta H^0 = -110.6$ kJ/mol

(3) $C_{(s)} + CO_{2(g)} \rightarrow 2CO_{(g)}$ $\Delta H^0 = +172.5$ kJ/mol

(4) $C_{(s)} + H_2O_{(g)} \rightarrow CO_{(g)} + H_{2(g)}$ $\Delta H^0 = +131.3$ kJ/mol

One can notice that CO_2 is the first gas to be generated during the combustion and releases much more heat than the conversion to CO, which one may prefer if the thermal efficiency is desired. But at high temperatures, the CO_2 becomes very unstable if compared to the CO. With that, the famous Boudouard Reaction, also known as the Solution Loss Reaction or Gasification Reaction, makes the CO the only stable oxide of carbon and this gas passes through a bed of coke. The humidity from the blast and coal also reacts to form H_2 and CO (GHOSH et al., 2008).

3.3 Pulverized Coal Injection system

The PCI technology was developed around the 19th century. One example of its first use is dated in Japan in 1981 on the Oita 1 Blast Furnace of Nippon Steel, after the second oil crisis (ISHII, 2000). With the increasing consumption of fossil fuels and the rising steel demand, the cost of coke production has increased considerably. One of the main costs is the decrease in the coke oven equipment life. To deal with the impact, industries have introduced PCI technology to reduce the coke rate. Figure 3.8 shows the impact of PCI technology on the coke rate in Japan.

Figure 3.8 – Coke rate decreasing by year in Japan after the PCI operation start

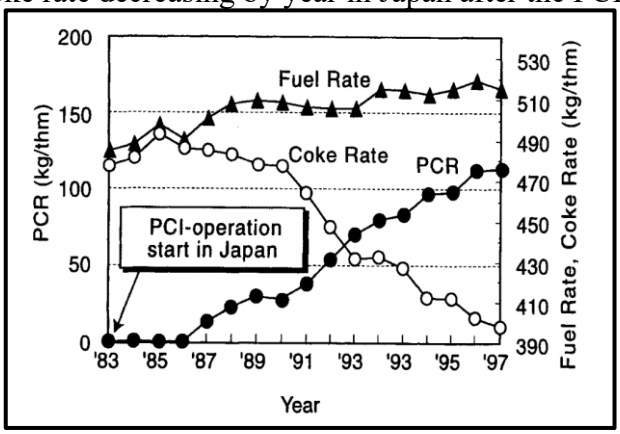

Source: ISHII, 2000.

The operation consists of a lance that injects pulverized coal (no-coking coal) through the blowpipe at the same time the hot blast blows. The coal injection direction is given by the lance carrier gas (normally N_2) but also suffers acceleration by the blast jet and burns inside the raceway cavity. Unburnt coal particles may accumulate in a layer by the raceway boundaries called Bird's nest. Figure 3.9 outlines the PCI in operation.

Figure 3.9 – The raceway cavity and PCI injection scheme and operation

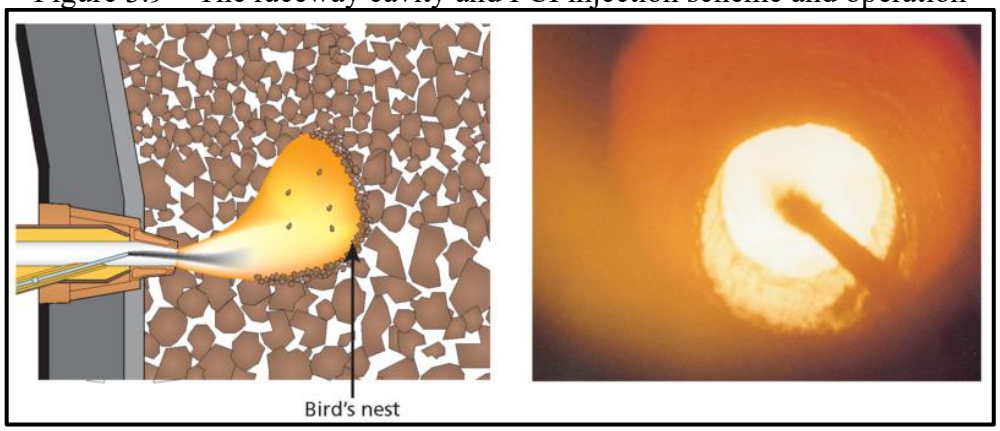

Source: GEERDES et al., 2015.

Some advantages and disadvantages of using PCI in blast furnaces, according to CAVALIERE, 2016, and SHIOZAWA, 2013 are:

Benefits

Monetary / Productive

1. The coal type used for PCI is lower cost than coke coal (approximately U$$ 100/t) and does not add coking costs;
2. PCI can replace about 25-40% by volume of coke. The cost reduction can reach $ 75 M/year) considering the blast furnace production and the PCI installation costs;
3. Coke loading time can be reduced, which means increased ore loading time, which in theory would increase productivity;
4. Coke battery life can be extended by slowing production.

Operational

1. An additional tool to control the blast furnace operation, as the reactor is in most parts sealed at the lower region;
2. Response time to injection changes is faster (less than 2 hours) than coke load rate changes (greater than 6 hours);
3. It is possible to apply other solid materials than coal, such as plastics, biomass, charcoal, among other inputs;
4. The PCI technology could lead to further improvements (co-injection gas such as H_2 and coke oven gas).

Environmental

1. Reduction of environmental impacts, given that coke plants, are characterized by their high polluting potential;
2. The US Environmental Protection Agency and the Joint Research Centre of the European Commission both classified the PCI technology as one of the best available ironmaking technologies point forward to energy-saving, CO_2 emission reduction, and fuel switch from coke to coal or hydrocarbons.

Disadvantages

Optimization / Operational

1. High testing costs associated with conditions of the coal used (grinding, characterization, volatile, and ash content);
2. High rate PCI operations can decrease the permeability by the accumulation of unburned fines between the combustion zone and the dead man, the Bird's nest;
3. Optimizations are trial and error, as numerical predictions may not be efficient or not applicable;
4. It can increase the ore/coke ratio which intensifies the gas flow at the walls, increasing the head loss, wall degradation, and reduce the quality of the burden descent;
5. An increase in the ore/coke ratio could results in reduced coke layer thickness, making it vulnerable to higher burden loads;
6. Can decrease the flame temperature reducing the melting rate potential at the cohesive zone;
7. Cause an increase in the combustion gas which increases the overall gas volume elevating the pressure drop at the lower part;
8. May alter the distribution of heat and gas supply on the raceway, as well as coke and iron ore consumption, reducing operating efficiency.

3.4 Coal combustion process

When coal particles start the process of combustion, in a more controlled environment, the particles follow three main well-defined steps, which can further be more subdivided, but for the sake of simplicity, they may be classified as particle preheating, volatile combustion, and char combustion. Figure 3.10 plots these steps by the particle temperature.

Figure 3.10 – Coal particle combustion process

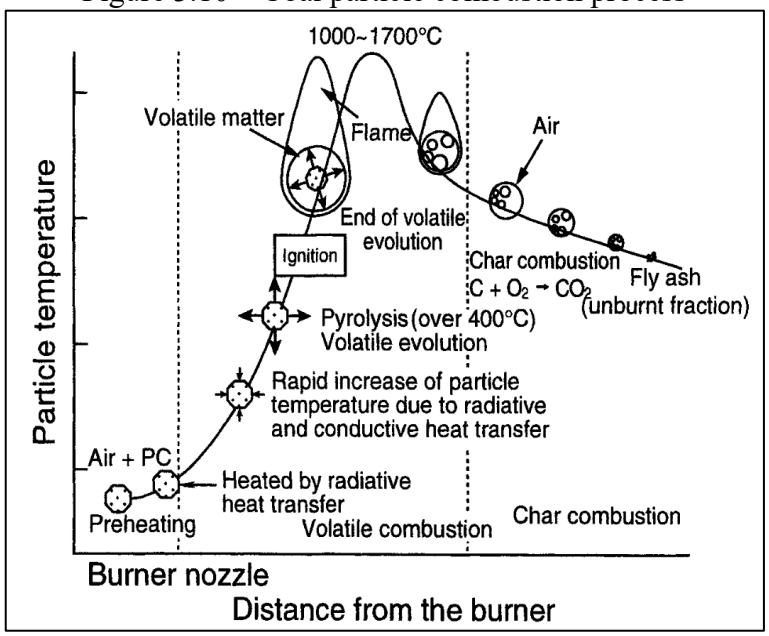

Source: ISHII, 2000.

First, particles start being preheated up, mainly by radiation, a step also called inert heating. This step takes place as long as the particle is below the devolatilization vaporization temperature (ALGANASH, 2015).

Then, the pyrolysis and devolatilization process occurs when coal reaches a devolatilization temperature that can vary from 400 to 550 °C, approximately. It represents the release of the moisture and volatile matter entrapped within the coal. The volatile matter can be considered as a hydrocarbon molecule that can be represented by $C_xH_yO_wN_z$ (Sulfur may be present) and promotes energy for the system through its combustion. The forms of heat transfer acting at the second step could be radiative and conductive heat transfer, which helps the ignition of the particle and its surface combustion.

At the end of the volatile release, the flame is well placed in the particle and the char combustion takes place. In this last step occurs the oxidation of the surface involving solid carbon (char). As a result of this process, there is an inert residue of complete combustion of the coal particle, called ash.

The devolatilization of a coal particle is temperature-related, which means higher temperatures aids in achieving higher rates of devolatilization. The char combustion is both temperature and oxygen diffusion dependent, as the combustion reaction needs the particle surface to be at a high temperature and properly surrounded by oxygen. There are many other factors related to the properties of the coal that can be measured and interferer with coal combustion, properties that affect the mass transfer, and chemical reactions. To cite some properties: macerals, specific surface area, pore size, and internal structure, the content of

volatile matter, and many others (ISHII, 2000). Figure 3.11 illustrates a sketch of the coal internal structure.

Figure 3.11 – Coal particle and its porous structure

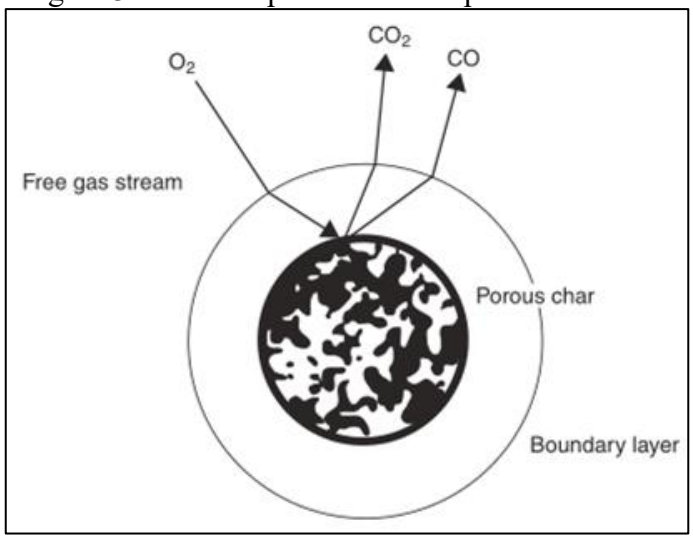

Source: OSBORNE, 2013.

There are proper procedures to evaluate coal combustion, which are interested in validating models and collect results as the burnout of the coal. Burnout measures the efficiency of coal combustion, and includes, directly or indirectly, the combustion time and the particle diameter. One example in which burnout can be measured is in types of equipment called test rigs. Figure 3.12 illustrates one example of this experiment.

Figure 3.12 – Test rig example in CanmetENERGY-Ottawa

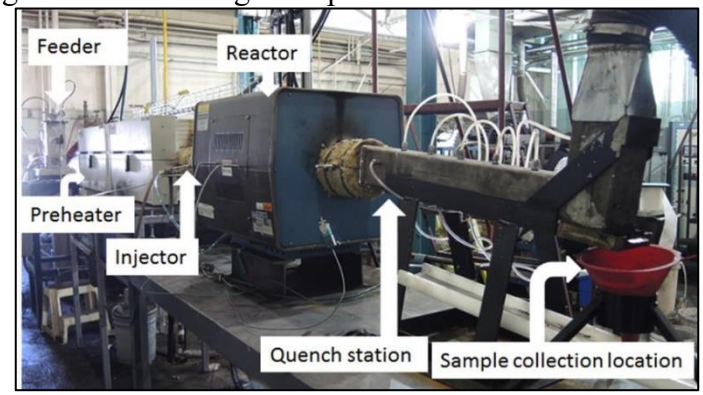

Source: RAY et al., 2015.

Such an experiment in the study from Figure 3.12 calculates the coal burnout from ash content of the parent coals and the collected char samples after the combustion process. The burnout is then calculated as the ratio of mass loss to the total combustibles present in the parent coal (RAY et al., 2015).

3.5 Raceway formation and combustion simulation studies

The studies to investigate the raceway formation, quantitatively, are dated from the 1950s. These studies can be classified in many different ways, for example, cold or hot models, experimental or numerical simulation, or both, among others (JAPAN, 1987). Nowadays, the raceway role in blast furnaces, its shape and size, how it distributes the reducing gases and energy to the lower parts of the furnace, the time-dependent factors as instability and accumulation of unburnt fines, including other subjects, are well known, but many investigations could still be done yet (KUANG et al., 2018, ABHALE et al., 2020).

Among the experimental studies, MOJAMDAR et al., 2018 used an experimental setup to replicate the moving bed and developed a detailed study of raceway size concerning different parameters such as gas velocity, bed height, and particle flow rate. The researchers confirmed the existence of cavity hysteresis phenomenon in a stationary packed bed, and that this effect is only valid for low particle flow rate in moving beds, and that if there are no frictional forces then there would not be any hysteresis in the system.

A study from MONDAL et al., 2005 developed a numerical model to predict the shape and size of the raceway by the blast air injected in an actual blast furnace geometry through the tuyeres. The blast furnace was considered a packed coke bed following an Eulerian-Eulerian approach, as an interpenetrating continuum. The study evaluated the influences of air blast velocity, initial porosity of the coke bed, and the bed height on the shape and size of the raceway. It was found that these parameters affected the raceway shape and size, increasing or decreasing.

Using a similar formulation from the study of Mondal, more recently, SAFRONOV et al., 2017 developed a 3D transient numerical model to predict the shape and size of the raceway, in which the effect of the cohesive zone on the raceway geometry was also taken into account, and the actor's results were in reasonable agreement with experimental data.

Beyond the formation, raceway combustion is also a field of study. The concern at this step is to understand the reactions that happen at high temperatures. The result of this quantification can be represented by the composition distribution of gases in the raceway, which are on its most part, CO_2, CO, H_2., where the gas species production/destruction is calculated by the reaction rate model used.

WU et al., 2019 reported a study in which the raceway formation and combustion with PCI were coupled based on data exchanging between the steps. First, the raceway shape, based on the volume fraction distribution is calculated, without the effects of reactions, then the

combustion process can take place. After the combustion with the first obtained raceway shape, the results of particle mass loss and temperature are stored and used to calculate source terms of the mass and momentum equations in a new raceway shape simulation. This process is put in a loop until the cavity formation reaches convergence. There are other works, from the same study group, which used a similar approach of calculating the raceway shape and size in conjunction with the combustion (OKOSUN et al., 2017, OKOSUN et al., 2016, FU et al., 2011, ZHOU, 2008)

As counter-examples, one can cite the works from MAIER et al., 2014 and SHEN et al., 2011 which developed approach consists of simulating the raceway shape and then use as a constant porosity profile, not being altered by the combustion.

The cited works used similar models to calculate the coke rate combustion. The reaction model used in these studies is to consider an intrinsic model (SMITH, 1982), which combines the chemical reactions and gas transport through parameters such as particle shape factor, reactivity, and pore structure (particle porosity and pore tortuosity). These parameters combine themselves in expressions that simulate the particle's internal structure (Thiele modulus and effective intra-particle diffusion equations). The present study will use the kinetic reaction equations developed by DE CASTRO et al., 2011 to supply such physical and thermophysical parameters for the coke and PCI rate combustion reactions.

3.6 Pulverized coal injection simulation studies

To model the PCI process, many studies appeal to the use of the discrete particle model (DPM) to track the coal particles. The model uses a Lagrangian approach to represent individuals or assembly of particles and their interaction with the fluid phase, but the interaction between the particles is simplified or not considered. There are models in which is used the discrete element method (DEM) as well, a method that describes more detailed particle's interaction with each other. Although the last method is more computationally expensive, with the increase of speed of calculus, the method is still in full use, but in most of the cases, to model the burden distribution of blast furnaces, where the forces particle-particle and particle-wall are more demanding (ABHALE et al., 2020, KUANG et al., 2018).

Among the coal combustion studies, there are those in which the focus is the coal combustion in a controlled environment, as in test rigs or burners, where the combustibility of the coal using different mixtures is investigated, or those studies that are interested in evaluating the coal combustion with some co-injections in a proper blast furnace condition, that is, in a raceway combustion situation.

In an experimental and numerical study, MURAO et al., 2019 investigated the influence of hydrogenous reducing agents (HRA) in conjunction with pulverized coal for a small-scale combustion furnace and a 3D numerical simulation. The simulation used an Eulerian-Lagrangian approach for gas and coal particles. The numerical and experimental were then compared and were in good agreement.

In two separate works but from the same study group, (WIJAYANTA et al., 2014b, WIJAYANTA et al., 2014a), a tuyere/raceway geometry was used to investigate the possibility of injecting pulverized biochar instead of conventional pulverized coal, which is a potential novel use for the numerical models of PCI.

For a class of blast furnace geometry models, LI et al., 2014 investigated the coal injection considering an unchanged raceway shape during the coal combustion with the burnout rate as the evaluation indicator. The orthogonal experiments found that pulverized coal, the injection rate, the oxygen enrichment rate, the blast temperature, the spraying gun type, the blast volume, and the angle, are the most influencing parameters on the burnout rate.

As described for coke combustion in the previous section, the present study will consider the kinetic rates equations developed from the of DE CASTRO et al., 2011.

4 MODELS FORMULATION

In this section, the governing equations for the models used in the present study will be described in detail.

First, the raceway formation model, which used the granular model will be presented. This model was applied to the coke and gas phase during the cavity profile calculation through the concept of the volume fraction and drag force.

The pulverized coal phase modeling will be covered. The coal particles were treated as a discrete phase, which is influenced by the flow field, but their influence on the former is limited to the source terms.

Among the other sections, auxiliary models were also included, as the $k - \varepsilon$ turbulence model, radiation, and phase properties.

Lastly, the combustion model formulation used will be described in detail, with the parameters and reaction constant that were considered.

4.1 Raceway formation

Raceway formation was simulated using a transient Eulerian approach. This approach describes the flow as a whole, without following the particles, but describing the field of properties (mass, density, velocity, pressure) as a function of position and time (VERSTEEG et al., 2007). For multiphase flows, the Eulerian approach treats the phases mathematically as continuous interpenetrating domains. This required the selection of a method to model the gas phase motion interacting with the coke particles, initially motionless in the domain.

To model the interaction of the mixture gas-coke, the granular model was used to describe the flow behavior of the fluid-solid mixture. In this model, solid-phase stresses are derived by an analogy between the random particle motion arising from particle-particle collisions and the thermal motion of molecules in a gas, taking into account the inelastic behavior of the granular phase. As is the case with gas, the intensity of particle velocity fluctuations determines the solid phase stresses, viscosity, and pressure (SYAMLAL et al., 1989).

As a multiphase simulation, the volume of one phase cannot be occupied by the other phases, the concept of volumetric fraction, α, must be inserted into the conservation equations. These volume fractions are assumed to be continuous functions of space and time, and their sum is equal to one:

$$\sum \alpha_i = 1 \tag{1}$$

where i is the index identifying each phase (i = gas (g), solid (coke) (s)). With the volume fraction definition, one must also define the volume of phase and the effective density of phase i concepts:

$$V_i = \int_V \alpha_i dV \tag{2}$$

$$\hat{\rho}_i = \alpha_i \rho_i \tag{3}$$

The conservation equations for each phase are then derived to obtain a set of expressions, which have a similar structure for the gas and coke phases. The Equation (4) is the transport equation for a generic property ϕ:

$$\frac{\partial(\alpha_i \rho_i \phi_i)}{\partial t} + \nabla \cdot \left(\alpha_i \rho_i \phi_i \overrightarrow{U_i}\right) = \nabla \cdot \left(\Gamma_\phi \nabla \phi_i\right) + S_\phi \tag{4}$$

where ρ_i is the phase i density, ϕ_i is the property evaluated for phase i in each conservative equation and can assume different units, $\overrightarrow{U_i}$ is the velocity vector relative to each phase i in directions x, y, and z of the cartesian coordinate system. The variable Γ_ϕ is the appropriate diffusion coefficient that transports the considered property ϕ. The last term S_ϕ is the source term, which can assume different features dependent on the equation to be solved.

In other words, the Equation (4) can be expressed as:

$$\begin{bmatrix}\text{Rate of increase}\\ \text{of } \phi \text{ of fluid}\\ \text{element}\\ \text{(rate of change)}\end{bmatrix} + \begin{bmatrix}\text{Net rate of flow}\\ \text{of } \phi \text{ out of}\\ \text{fluid element}\\ \text{(convective term)}\end{bmatrix} = \begin{bmatrix}\text{Rate of increase}\\ \text{of } \phi \text{ due to}\\ \text{diffusion}\\ \text{(diffusive term)}\end{bmatrix} + \begin{bmatrix}\text{Rate of increase}\\ \text{of } \phi \text{ due to}\\ \text{sources}\\ \text{(source term)}\end{bmatrix}$$

The Equation (4) can be used as a starting point to develop computational procedures for the Finite Volume Method (FVM), which consists of its integration over the control volume and time to produce the mass, momentum, and energy conservation equations (MALISKA, 2017).

In the present study, for the raceway formation simulation, the energy equation will not be considered. This assumption was also used by other authors in previous works (MA, 2017, OKOSUN, 2018, WU et al., 2019).

The mass conservation equation, or continuity equation, with the volumetric fraction term, can be expressed as:

$$\frac{\partial\left(\alpha_i\rho_i\right)}{\partial t}+\nabla\cdot\left(\alpha_i\rho_i\overrightarrow{U_i}\right)=0 \tag{5}$$

The Equation (6) describes the conservation of momentum phase *i*:

$$\frac{\partial\left(\alpha_i\rho_i\overrightarrow{U_i}\right)}{\partial t}+\nabla\cdot\left(\alpha_i\rho_i\overrightarrow{U_i}\overrightarrow{U_i}\right)=-\alpha_i\nabla P+\nabla\cdot\overline{\overline{\tau}}_i+\alpha_i\rho_i\vec{g}+K_{ij}\left(\overrightarrow{U_i}-\overrightarrow{U_j}\right) \tag{6}$$

where P is the pressure, $\overline{\overline{\tau}}_i$ is the stress tensor, $\vec{g}$ is the acceleration of gravity, and K_{ij} is defined as the momentum transfer coefficient between the gas and solid granular phases (SYAMLAL et al., 1989).

The stress tensor $\overline{\overline{\tau}}_i$ can be expressed as:

$$\overline{\overline{\tau}}_i=\alpha_i\mu_i\left(\nabla\overrightarrow{U_i}+\nabla\overrightarrow{U_i^T}\right)+\alpha_i\left(\lambda_i-\frac{2}{3}\mu\right)\left(\nabla\cdot\overrightarrow{U_i}\right)\overline{\overline{I}} \tag{7}$$

where μ_i and λ_i are the shear and bulk viscosities, respectively. $\overline{\overline{I}}$ is defined as the unit tensor.

The momentum transfer coefficient in the last term of the Equation (6) can be defined as:

$$K_{gs}=\frac{\alpha_s\rho_s f}{\tau_s} \tag{8}$$

where $K_{gs}=K_{sg}\,.\,\tau_s$ is the particle relaxation time and f is defined according to the equation proposed by the Syamlal-O'Brien drag model.

The particle relaxation time τ_s is expressed as:

$$\tau_s = \frac{\alpha_s d_s^{\,2}}{18\mu_g} \tag{9}$$

where d_s is the diameter of the solid granular particle.

The factor f proposed by the Syamlal-O'Brien is expressed by:

$$f = \frac{C_D \,\mathrm{Re}_s\, \alpha_s}{24 v_{rs}^2} \tag{10}$$

where C_D is the drag function expressed by DALLAVALLE, 1948, Re_s is the Reynolds number for the granular phase, and v_{rs} is the correlation for the solid phase terminal velocity.

The drag function C_D can be expressed as:

$$C_D = \left(0.63 + \frac{4.8}{\sqrt{\mathrm{Re}_s / v_{rs}}} \right)^2 \tag{11}$$

The Reynolds number Re_s is expressed by:

$$\mathrm{Re}_s = \frac{\rho_g d_s \left| \overrightarrow{U_s} - \overrightarrow{U_g} \right|}{\mu_g} \tag{12}$$

The correlation v_{rs} for the solid phase terminal velocity, valid for individual or groups of particles, is defined according to GARSIDE et al., 1977:

$$v_{rs} = 0.5\left(A - 0.06\,\mathrm{Re}_s + \sqrt{(0.06\,\mathrm{Re}_s)^2 + 0.12\,\mathrm{Re}_s(2B - A) + A^2} \right) \tag{13}$$

where the constants *A* and *B* are expressed as:

$$A = \alpha_g^{4.14} \tag{14}$$

$$B = \begin{cases} 0.8\alpha_g^{1.28} & \text{se } \alpha_g \le 0.85 \\ \alpha_g^{2.65} & \text{se } \alpha_g > 0.85 \end{cases} \tag{15}$$

Substituting Equations (9), (10) and (11) in the Equation (8), the result is:

$$K_{gs} = \frac{3\alpha_s \alpha_g \rho_g}{4 v_{rs}^2 d_s} C_D \left(\frac{\mathrm{Re}_s}{v_{rs}} \right) \left| \overrightarrow{U_s} - \overrightarrow{U_g} \right| \tag{16}$$

The indexes switch $K_{sg} = K_{gs}$ produces the corresponding gas/solid terms.

4.2 Pulverized coal – discrete particle model

Pulverized coal particles are treated as a discrete secondary phase solved numerically based on the Lagrangian approach. The trajectories of coal particles are calculated through the integration of the force balance acting on a particle, based on Newton's second law (ANSYS, 2017b). The force balance for a particle in the *x*-direction can be seen in the Equation (17) below:

$$m_p \frac{du_p}{dt} = \sum F_p = F_D \left(u - u_p \right) + \frac{g_x \left(\rho_p - \rho \right)}{\rho_p} + F_x \tag{17}$$

Figure 4.1 – Interaction between discrete and continuous phases

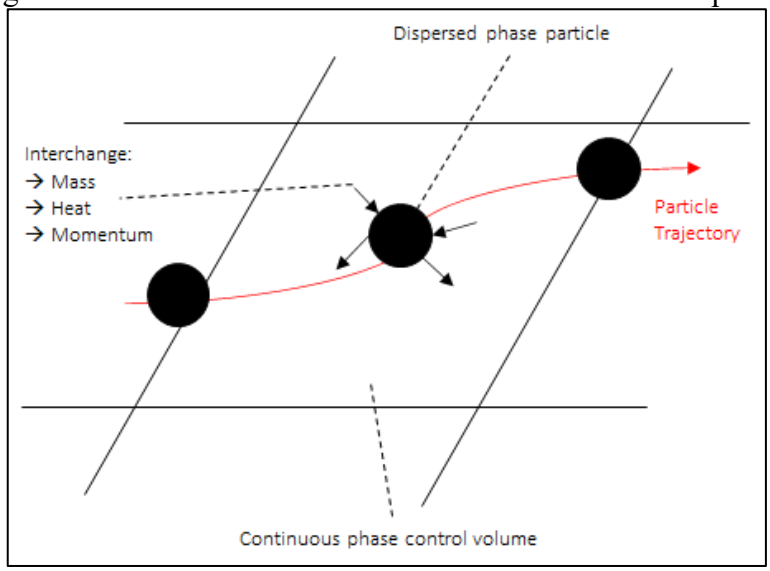

Source: ALGANASH, 2015 (adapted).

where m_p and u_p are respectively the particle mass and velocity. The variable F_p is relative to the different forces acting on the particle with density ρ_p in a fluid of velocity u and density ρ, which in the present study where considered the drag force, F_D, the acceleration gravity, g_x, and the lift force included in the term of the additional force F_x.

The drag force F_D can be expressed as:

$$F_D = \frac{18\mu}{\rho_p d_p^2} \frac{C_D \, \mathrm{Re}_p}{24} \tag{18}$$

where μ is the viscosity and Re_p is Reynolds number based on the particle diameter and the relative velocity calculated similarly to Equation (12).

The term C_D in the drag force is the drag coefficient for the particle, which in the present study was considered spherical and is described by the expression originated from the work of MORSI et al., 2006:

$$C_D = a_1 + \frac{a_2}{\mathrm{Re}_p} + \frac{a_3}{\mathrm{Re}_p^2} \tag{19}$$

where a_1, a_2, and a_3 are constants that apply over several ranges of Re_p.

The lift force in the term F_x is described by the expression developed by SAFFMAN, 1965 and is included to count the lift due to shear stress. The expression applied to the model is based on a generalization of Saffman expression for three-dimensional shear fields from the work of LI et al., 1992 and can be seen in the Equation (20) below:

$$\overrightarrow{F} = \frac{2Kv^{1/2}\rho d_{ij}}{\rho_p d_p \left(d_{lk} d_{kl}\right)^{1/4}} \left(\vec{u} - \overrightarrow{u_p}\right) \tag{20}$$

where K = 2.594, v is the kinetic viscosity and d_{ij} is the deformation tensor given by $d_{ij} = \left(u_{ij} + u_{ji}\right)/2$.

4.2.1 Discrete random walk model

As the PCI operation occurs in a turbulent system, one must take into account the effects of the stochastic change in velocity, the misalignment of particles and fluid trajectories random fluctuating velocity inherent in such a regime. The present study used the discrete random walk model (DRW) (GOSMAN et al., 1983) approach to calculate the interaction of the particles and turbulent eddy generated by the velocity fluctuations.

This model uses the effects of turbulence on the particle path by applying the concept of mean gas phase velocity and fluctuating velocity in the particle trajectory expressions, Equations (17) to (20). The instantaneous local value of the velocity of the mixture gas-phase is given by:

$$u = \bar{u} + u' \tag{21}$$

which in the present work will be calculated using the realizable $k-\varepsilon$ turbulence model. The mean velocity $\bar{u}$ is calculated by the Favre averaged Navier-Stokes equations for the gas phase (VERSTEEG et al., 2007) and u' is the fluctuating velocity that follows a Gaussian probability distribution emerged from the stochastic turbulent eddy concept, given by:

$$u' = \zeta\sqrt{\overline{u'^2}} \tag{22}$$

$$\sqrt{\overline{u'^2}} = \sqrt{2k/3} \tag{23}$$

where ζ is a normal distributed random number.

Substituting the fluctuating velocity in the gas-phase velocity, Equation (21):

$$u = \bar{u} + \zeta\sqrt{2k/3} \tag{24}$$

where k is the turbulent kinetic energy provided by the $k-\varepsilon$ turbulence model. This velocity is applied in the particle interaction with the turbulence eddy, and the time required to cross it while it still existing within the system.

The characteristic lifetime of the turbulence eddy is defined as:

$$\tau_e = 2T_L \tag{25}$$

where T_L is the fluid Lagrangian integral time, that using the $k-\varepsilon$ model is given by:

$$T_L = 0.30\frac{k}{\varepsilon} \tag{26}$$

The time necessary for the particle to cross an eddy is given by:

$$\tau_{\text{cross}} = -\tau_p \log\left(1 - \frac{l_e}{\tau_p \left|u - u_p\right|}\right) \tag{27}$$

where τ_p is the particle relaxation time, l_e is the eddy length scale. The time of interaction of the particle with the gas phase is the minimum value of the eddy lifetime, τ_e, and the time required to cross the eddy, τ_{cross} (BERMUDEZ et al., 2010).

4.3 $k - \varepsilon$ Turbulence model

The $k - \varepsilon$ model is a classical, decent, and usual description of turbulence, and it was used in the present study. It allows the effects of transport of turbulence properties by convection and diffusion and for production and destruction of turbulence (VERSTEEG et al., 2007). This model was also used in many other works related to the subject of coal combustion with satisfactory results being reported (GU et al., 2010).

Two transport equations, one for the turbulent kinetic energy k and another for the rate of dissipation of turbulent kinetic energy ε, are solved. The two equations are presented below.

$$\frac{\partial}{\partial t}(\rho k) + \frac{\partial}{\partial x_i}(\rho k u_i) = \frac{\partial}{\partial x_j}\left[\left(\mu + \frac{\mu_t}{\sigma_k}\right)\frac{\partial k}{\partial x_j}\right] + G_k + G_b - \rho\varepsilon - Y_M + S_k \tag{28}$$

$$\frac{\partial}{\partial t}(\rho \varepsilon) + \frac{\partial}{\partial x_i}(\rho \varepsilon u_i) = \frac{\partial}{\partial x_j}\left[\left(\mu + \frac{\mu_t}{\sigma_\varepsilon}\right)\frac{\partial \varepsilon}{\partial x_j}\right] + C_{1\varepsilon}\frac{\varepsilon}{k}(G_k + C_{3\varepsilon}G_b) - C_{2\varepsilon}\rho\frac{\varepsilon^2}{k} + S_\varepsilon \tag{29}$$

With constants: $G_{1\varepsilon} = 1.44$, $C_2 = 1.92$, $\sigma_k = 1.0$, and $\sigma_\varepsilon = 1.3$. The terms S_ε and S_k are source terms that can be added. The variables σ_k and σ_ε are the turbulent Prandtl numbers for k and ε, respectively. The G_k is the generation of turbulent kinetic energy term due to the mean velocity gradients and G_b is the turbulent kinetic energy generated by buoyancy. Y_M is the dissipation rate term due to fluctuating dilatation in compressible flow. Y_M and G_b were not considered in the present study.

The turbulent viscosity, or eddy viscosity, emerged from the Reynolds stress term, introduced to close the Reynolds Average Navier-Stokes equations (RANS) after applying the Favre-time-averaging operation is defined as:

$$\mu_t = \rho C_\mu \frac{k^2}{\varepsilon} \tag{30}$$

where C_{μ} = 0.09.

4.4 Coke heat transfer

The coke heat transfer simulation was done following a transient two-dimensional approach, with a time step of 10^{-3} s (recommend for eulerian granular flows, ANSYS, 2017b). To achieve a high-temperature domain within a short simulation time, an assumption was made concerning the properties of thermal conductivity and specific heat, which were set to 1.7 W/(m·K) and 8.5 J/(kg·K), respectively. This arbitrary treatment was also employed by HOU et al., 2015, which developed a CFD-DEM numerical model to simulate a transient coke heat transfer.

The next set of expressions will cover the energy equation used in the coke combustion simulation. This simulation was done after the raceway cavity shape was simulated, and the volume fraction distribution achieved. Then, the volume fraction was kept constant during the combustion reactions. The terms of convection-advection, conduction, heat transfer between the gas and coke, and reactions (gas-gas and gas-coke), were considered. The conservation of energy in terms of enthalpy can be expressed as follows:

$$\frac{\partial\left(\alpha_i \rho_i h_i\right)}{\partial t} + \nabla \cdot \left(\alpha_i \rho_i h_i \overline{U_i}\right) = \nabla \cdot \left(k_i \nabla T\right) + Q_{gs} + S_{gs} \tag{31}$$

where S_{gs} represent the source term that includes sources of enthalpy due to chemical reactions or radiation. The enthalpy h_i of phase *i* is defined as:

$$h_i = \int_{T_0}^{T} c_{p,i} dT + \Delta h_{f,i} \tag{32}$$

where $c_{p,i}$ is the specific heat of phase *i* and $h_{f,i}$ the heat of formation. The heat exchange between the phases can be expressed as:

$$Q_{gs} = Q_{sg} = h\left(T_g - T_s\right) \tag{33}$$

where the convective heat transfer h is described as:

$$h = \frac{k_g \mathrm{Nu}_s}{d_s} \tag{34}$$

which k_g is the thermal conductivity of the gas phase. The Nusselt number relative to the granular phase, Nu_s, is calculated according to the model proposed by GUNN, 1978:

$$\mathrm{Nu}_s = \left(7 - 10\alpha_g + 5\alpha_g^2\right)\left(1 + 0.7\,\mathrm{Re}_s^{0.2}\,\mathrm{Pr}^{1/3}\right) + \left(1.33 - 2.4\alpha_s + 1.2\alpha_g^2\right)\mathrm{Re}_s^{0.7}\,\mathrm{Pr}^{1/3} \tag{35}$$

The Reynolds number can be determined using Equation (12). The Prandtl number of the continuous phase is calculated by:

$$\mathrm{Pr} = \frac{c_{p,g}\mu_g}{k_g} \tag{36}$$

4.5 Coal particles heat transfer

The coal particle temperature is modeled by the energy equation including convective heat transfer, radiative heat transfer, heat loss from devolatilization reaction in the particle, and the heat of char combustion heterogeneous reactions (ISHII, 2000, ANSYS, 2017b). The equation is the mathematical translation of Figure 3.10, which covers the stages of single-particle combustion: fuel heating and drying, devolatilization, and volatile and char combustion (as illustrated in Figure 3.10).

The heat balance for a particle of mass m_p and specific heat $c_{p,p}$ can be mathematically expressed as:

$$m_p c_{p,p} \frac{dT_p}{dt} = \sum \dot{Q}_p = hA_p\left(T_g - T_p\right) + A_p \varepsilon_p k_B \left(\theta_R^4 - T_p^4\right) - f_h \sum_{r=1}^{N} \frac{dm_p}{dt} H_{\mathrm{reac}_r} \tag{37}$$

In the convective heat transfer term, the heat transfer coefficient, *h*, is calculated using the correlation of Ranz and Marshall:

$$\mathrm{Nu} = \frac{hd_p}{k} = 2 + 0.6\,\mathrm{Re}_p^{1/2}\,\mathrm{Pr}^{1/3} \tag{38}$$

where Nu is the Nusselt number, k is the thermal conductivity of the continuous phase, Re_p is the Reynolds number, and Pr is the Prandtl number calculated by Equation (36).

In the radiation term, A_p is the particle superficial area, ε_p is the particle emissivity, k_B is the Stefan-Boltzman constant, and θ_R is the radiation temperature expressed as:

$$\theta_R = \left(\frac{G}{4k_B} \right)^{1/4} \tag{39}$$

where G is incident radiation, given by:

$$G = \int_{\Omega=4\pi} I d\Omega \tag{40}$$

where I is the radiation intensity and Ω is the solid angle.

The last term in the heat balance equation is relative to the surface reactions. H_{reac} is the enthalpy of each reaction r among N heterogeneous reactions including the heat gain due to char combustion reactions and the heat loss due to the gasification. f_h is the fraction of heat absorbed by the particle and is equals to 0.3.

4.6 Radiation model (P-1 model)

The present study modeled the radiation heat transfer using the P-1 radiation model (spherical harmonic method). The P-1 model is the first-order approximation of the radiative transport equation (RTE), necessary because of its complex solution (HOWELL et al., 2010). In the practice of pulverized coal injection, the radiative heat transfer is responsible for substantial energy for the reactions to take place. The P-1 model is well known and is used in several other studies because of its efficiency to simulate particle combustion due to the assumption of the DPM that the particles are thermally thin and tiny in size (SILAEN et al., 2010, MA et al., 2007, AJILKUMAR et al., 2009).

The radiation flux in the P-1 model is described as:

$$Q_R = -\frac{1}{3(a+\sigma_s) - C\sigma_s} \nabla G \tag{41}$$

where a is the absorption coefficient, determined by the weighted-sum-of gray-gases model (WSGGM), σ_s is the scattering coefficient, C is the linear anisotropic phase function coefficient, which is a property of the fluid (dictates the fraction of radiant energy scattered backward or forward) that ranges from -1 to 1, and G is the incident radiation, which is the sum of each radiation intensity from all the direction over the whole solid angle The term multiplying the derivative incident radiation is an alteration of the diffusivity to model the scattering effects:

$$\Gamma = -\frac{1}{3(a+\sigma_s)-C\sigma_s} \tag{42}$$

which results in:

$$Q_R = -\Gamma \nabla G \tag{43}$$

The transport equation for the incident radiation is given by:

$$\nabla \cdot (\Gamma \nabla G) = aG - 4an^2 k_B T^4 \tag{44}$$

where n is the refractive index of the medium and k_B is the Stefan-Boltzmann constant. One could combine the equations (43) and (44), resulting in:

$$\nabla \cdot Q_R = aG - 4an^2 k_B T^4 \tag{45}$$

4.7 Phase properties

The phase properties were chosen to follow the ones from the works of DE CASTRO et al., 2011, DE SOUZA BALTAZAR et al., 2006, and NOGAMI et al., 2004, as they are the reference works taken for the analysis of the combustion simulations.

4.7.1 Solid-phase

The coal specific heat was calculated using a carbon solid piecewise polynomial equation with two ranges of temperature from FLUENT database

The coke specific heat was modeled as:

$$c_p^{\text{coke}} = 2\times10^2 + 2T_s - 1\times10^{-3}T_s^2 + 1.7\times10^{-7}T_s^3 \tag{46}$$

The thermal conductivity of the coke was considered as:

$$k_s^{\text{coke}} = \left(-7.6\times10^{-1} + 6.3\times10^{-3}T_s\right)\left(1-\alpha_{\text{coke}}\right) \tag{47}$$

4.7.2 Gas-phase

The gas density was calculated using the ideal gas law as expressed below:

$$\rho_g = \frac{P_g}{RT_g}\sum Y_{i,g}M_{w,i} \tag{48}$$

where P_g is the pressure of the gas, R the gas constant, $Y_{i,g,}$ and $M_{w,i}$ are the mass fraction and molecular weight of the species i in the gas phase and T_g is the gas temperature. The pressure was prescribed at the inlet and outlet boundary conditions (atmospheric, 1 atm).

The gas mixture specific heat at a specific pressure is determined as a function of the species mass fraction Y_i by the mixture law:

$$c_p = \sum_i Y_i c_{p,i} \tag{49}$$

where each species c_p is calculated by polynomials functions and piecewise polynomial functions, depending on which chemical species are being considered using ANSYS, 2017b database.

The thermal conductivity of the gas is calculated using the kinetic theory:

$$k_g = \frac{15}{4}\frac{R}{M_w}\mu\left[\frac{4}{15}\frac{c_p M_w}{R}+\frac{1}{3}\right] \tag{50}$$

where μ is the computed viscosity.

The gas species viscosity is modeled using the kinetic theory as well:

$$\mu_i = 2.67\times10^{-6}\frac{\sqrt{M_{w,i}T_g}}{\sigma_i^2\Omega_i(T_i^*)} \tag{51}$$

where T_i^* is expressed as:

$$T_i^* = \frac{T_g}{\left(\varepsilon_i / k_B\right)} \tag{52}$$

where σ_i and ε_i are the Lennard-Jones characteristic length and energy parameter of the specie *i*, respectively, and k_B is the Boltzmann constant. The empirical expression Ω_i can be expressed as:

$$\Omega_i\left(T_i^*\right) = \frac{1.16145}{\left(T_i^*\right)^{0.14874}} + \frac{0.52487}{\exp\left(0.77320 T_i^*\right)} + \frac{2.16178}{\exp\left(2.4378 T_i^*\right)} \tag{53}$$

Using the species viscosity, the gas mixture viscosity is then calculated as:

$$\mu = \sum_i \left[\frac{X_i \mu_i}{\sum_j X_j \phi_{ij}} \right] \tag{54}$$

where X_i is the molar fraction of the species *i*. The parameter ϕ_{ij} is calculated as:

$$\phi_{ij} = \frac{\left[1 + \left(\frac{\mu_i}{\mu_j} \right)^{1/2} \left(\frac{M_{w,j}}{M_{w,i}} \right)^{1/4} \right]^2}{\left[8 \left(1 + \frac{M_{w,i}}{M_{w,j}} \right) \right]^{1/2}} \tag{55}$$

The gas species binary diffusivity is calculated by a modified Chapman-Enskog expression that is based on the kinetic theory and can be expressed as:

$$D_{ij} = 0.00188 \times \frac{\left[T_g^3 \left(\frac{1}{M_{w,i}} + \frac{1}{M_{w,j}} \right) \right]^{1/2}}{P_g \sigma_{ij}^2 \Omega_{ij}(T_{ij}^*)} \tag{56}$$

$$T_{ij}^* = \frac{T_g}{\left(\varepsilon / k_B\right)_{ij}} \tag{57}$$

$$\Omega_{ij}\left(T_{ij}^{*}\right)=\frac{1.06036}{\left(T_{ij}^{*}\right)^{0.15610}}+\frac{0.1930}{\exp\left(0.47635T_{ij}^{*}\right)}+\frac{1.03587}{\exp\left(1.52996T_{ij}^{*}\right)}+\frac{1.76474}{\exp\left(3.89411T_{ij}^{*}\right)} \quad (58)$$

$$\left(\varepsilon/k_B\right)_{ij}=\sqrt{\left(\varepsilon/k_B\right)_i\left(\varepsilon/k_B\right)_j} \quad (59)$$

$$\sigma_{ij}=\frac{\sigma_i+\sigma_j}{2} \quad (60)$$

4.8 Species transport

The conservation equation in the fluid phase for each species mass fraction, Y_i, through the solution of a convection-diffusion equation in a system has the general form:

$$\frac{\partial\left(\rho Y_i\right)}{\partial t}+\nabla\cdot\left(\rho\vec{U}Y_i\right)=-\nabla\cdot\vec{J_i}+R_i+S_i \quad (61)$$

where R_i is the net rate of production of species i by chemical reaction, S_i is the rate of creation/destruction relative to any species in the system (devolatilization species, in the case of the coal, for example). As the phenomenon occurs in a turbulent environment, the mass diffusion for the species i, $\vec{J_i}$, is defined as:

$$\vec{J_i}=-\left(\rho D_{m,i}+\frac{\mu_t}{\mathrm{Sc}_t}\right)\nabla Y_i \quad (62)$$

where μ_t is the turbulent viscosity, and $D_{m,i}$ is the mass diffusion coefficient for each species i in the gas phase. The Schmidt number Sc in the present study is given by:

$$\mathrm{Sc}_t=\frac{\mu_t}{\rho D_t}=0.7 \quad (63)$$

4.8.1 Gas-phase reactions

The reactions on the continuous gas phase, the combustion process, include chemical reactions that happen in a wide range of time scales. Such time scales are also affected by turbulence, which contributes to the complexity in modeling those variations in the fluxes

that varies from instantaneous to several seconds. Therefore, all effects involving turbulence/chemistry interaction need to be modeled. One model that includes these two interactions and is used in the present study is the Finite Rate/Eddy-Dissipation Model. This model calculates the value of the reaction rates for two different models (the Finite Rate model, and the Eddy Dissipation Model), and the resultant reaction rate is taken as the minimum of these two rates (ANSYS, 2017b). Such a relation can be expressed by:

$$R_i = \min\left(R_{\mathrm{Fr}}, R_{\mathrm{Edd}}\right) \tag{64}$$

The Eddy-Dissipation model is based on the assumption that the chemical reactions are extremely fast and controlled by turbulence (identified by the turbulence kinetic energy and dissipation rate ratio, the turbulence time scale, $k/\varepsilon > 0$, SPALDING, 1971), making the reaction rate of species be controlled by turbulent mixing, not requiring an ignition source to initiate combustion (non-temperature dependent) (MAGNUSSEN et al., 1977, MAGNUSSEN, 1981).

In the Finite-rate model, the effect of turbulence on the reaction rate kinetics is neglected, and the rates are determined by Arrhenius law (IRANNEZHAD, 2012). Effectively, the Finite-rate prevents reaction before the flame is being established. When the high temperature is reached, the eddy-dissipation rate is generally smaller than the Finite-rate, forcing the reactions to be mixing-limited controlled (ANSYS, 2017b).

4.8.1.1 Eddy dissipation model

In the Eddy Dissipation Model, the chemical reaction rate is governed by the large eddy mixing time scale, k/ε. The net rate, $R_{i,r}$, of production of species i due to reaction r, is given by the smaller of the two equations:

$$R_{i,r} = \min\left(R_{i,r\,(\mathrm{React})}, R_{i,r\,(\mathrm{Prod})}\right) \tag{65}$$

$$R_{i,r\,(\mathrm{React})} = v'_{i,r} M_{w,i} A \rho \frac{\varepsilon}{k} \min\left(\frac{Y_i}{v'_{i,r} M_{w,i}}\right) \tag{66}$$

$$R_{i,r\,(\mathrm{Prod})} = v'_{i,r} M_{w,i} A B \rho \frac{\varepsilon}{k} \left(\frac{\sum_p Y_p}{\sum_j^N v''_{j,r} M_{w,j}}\right) \tag{67}$$

where:

$M_{w,i}$ = molecular weight of species *i*;

Y_p = mass fraction of any product species, *p*;

Y_i = mass fraction of a particular reactant, *i*;

A = empirical constant equal to 4;

B = empirical constant equal to 0.5;

N = number of species;

$v'_{i,r}$ = stoichiometric coefficient for reactant *i*, in the reaction *r*;

$v''_{j,r}$ = stoichiometric coefficient for product species *j*, in reaction *r*.

4.8.1.2 Laminar finite-rate model

Using a simplified Laminar Finite-Rate Chemistry formulation (no reversible reactions and third body efficiencies), the chemical production rate, $R_{i,r}$, for species *i*, in a reaction *r*, can be expressed as:

$$R_{i,r} = k\left[C_{\mathrm{r}}\right]^{d}\left[C_{\mathrm{ox}}\right]^{e} \tag{68}$$

where:

k = forward rate constant;

C_{r} = molar concentration of reactant species;

C_{ox} = molar concentration of oxidant species;

d = rate exponent for reactant species

e = rate exponent for oxidant species.

The kinetic rate constant *k* is computed using Arrhenius expression:

$$k = AT^{\beta}\exp\left(-\frac{E}{RT}\right) \tag{69}$$

where:

A = pre-exponential (units vary);

β = temperature exponent (no unit);

E = activation energy (J/kmol);

R = gas constant (J/kmol.K);

T = gas temperature (K).

The volatiles combustion homogeneous reaction is going to be modeled as follows:

$$\text{Volatiles}_{(g)} + \nu'_1 O_{2(g)} \rightarrow \nu''_2 CO_{2(g)} + \nu''_3 H_2O_{(g)} + \nu''_4 N_{2(g)} \quad (70)$$

Two homogeneous reactions, the CO and H_2 combustion were also included:

$$CO_{(g)} + 0.5O_{2(g)} \rightarrow CO_{2(g)} \quad (71)$$

$$H_{2(g)} + 0.5O_{2(g)} \rightarrow H_2O_{(g)} \quad (72)$$

The reaction rates constants used are in Table 3 below:

Table 3 – Kinetic Constant of Homogeneous Reactions

Reaction	**Parameter**					
	A (Vary)	E (J/kmol)	β	d	e	Source
Volatiles + O_2	2.119×10^{11}	2.027×10^{8}	0	0.2	1.3	ANSYS, 2017c
CO combustion	1.3×10^{11}	1.26×10^{8}	0	1	0.5	HOWARD et al., 1973
H_2 combustion	540	1.51×10^{4}	0	1	1	PETERS, 1979

Source: (ALGANASH, 2015; GU et al., 2010).

4.9 Coal combustion steps

The present study used different models to calculate coal combustion during the passage of the particles through the reactor. The models were applied to the following heat and mass transfer steps: inert heating, water evaporation, coal devolatilization, and char surface combustion. Each step is applied when the particle reaches a specific temperature. With T_p as the particle temperature, one can divide each step in:

Inert heating: $T_p < T_{vap}$

Moisture evaporation: $T_{vap} < T_p < T_{devo}$

Coal devolatilization: $T_p > T_{devo}$

Char combustion: $T_p > T_{devo}$ after all volatile has been released

4.9.1 Inert heating

The first step occurs as soon as the particle is in contact with the high-temperature gas. It happens very fast and nearby the injector. The convective and radiative heat transfers are the main mechanisms that govern this step (Equation (37) without the H_{react} term). This phase also occurs when all the char is consumed and the ash is the main component in the particle.

4.9.2 Moisture evaporation

As the environment during coal combustion is characterized by high velocity and temperature gradients, plus the effect of turbulence, the water evaporation rate would not be controlled only by the diffusion mechanisms. Hence, the convective flow of the moisture from the coal wet surface to the gas phase becomes relevant, as the vaporization rates could vary from low to high rates (ANSYS, 2017b, SAZHIN, 2006). In this context, a convective/diffusive model was used to calculate the vaporization rates in the present study.

The moisture evaporation rate is calculated by:

$$\frac{dm_p}{dt} = k_c A_p \rho \ln\left(1 + B_m\right) \tag{73}$$

where k_c is the mass transfer coefficient, A_p is the particle surface area and B_m is the Spalding mass number.

The mass transfer coefficient is calculated using the Sherwood number for gas species given by:

$$\text{Sh} = \frac{k_c d_p}{D_{m,i}} = 2 + 0.6\,\text{Re}_p^{0.5}\,\text{Sc}^{1/3} \tag{74}$$

where $D_{m,i}$ is the diffusion coefficient of the moisture after the evaporation in the gas phase, d_p the particle diameter, Re_p the particle Reynolds number, and Sc the Schmidt number.

The Spalding mass number for the moisture surround the coal particle is expressed by:

$$B_m = \frac{Y_{i,s} - Y_{i,\infty}}{1 - Y_{i,s}} \tag{75}$$

where $Y_{i,s}$ and $Y_{i,\infty}$ are the moisture mass fraction at the surface of the particle and in the gas phase, respectively.

4.9.3 Coal devolatilization

The model used to describe the coal devolatilization rate was the single kinetic rate devolatilization model, which assumes that the rate of devolatilization is a first-order reaction, and depends on the amount of volatiles remaining in the particle (BADZIOCH et al., 1970). The expression below describes the rate of mass depletion of the coal particle:

$$-\frac{dm_p}{dt} = k\left[m_p - \left(1 - f_{v,0}\right)\left(1 - f_{w,0}\right)m_{p,0}\right] \tag{76}$$

where $f_{v,0}$ and $f_{w,0}$ are the mass fractions of volatile and liquid present in the particle initially, and m_p and $m_{p,0}$ are the particle mass after and before the devolatilization. The process is controlled by the kinetic rate constant k which follows the Arrhenius expression:

$$k = A\exp\left(-\frac{E}{RT_p}\right) \tag{77}$$

The constants used in the present study can be seen in Table 4 below:

Table 4 – Kinetic parameters used in the single rate devolatilization model

Constant	**Value**
***A* [s^{-1}]**	3.12×10^5
***E* [J/kmol]**	7.4×10^7

Source: BADZIOCH et al., 1970, ALGANASH, 2015.

4.9.4 Char and coke combustions

For the calculation of the reaction kinetics of char combustion (denomination used for the remaining mass after the gasification steps), the formulation applied in the work of DE CASTRO et al., 2011 was used. The reaction rates were implemented in the commercial software through external functions called user-defined functions (UDF), which supports the

programming languages C and C ++ (ANSYS, 2017a). Also, as the same reaction rates are applied for the coke simulation, the expressions in this section are valid for both cases.

The carbon in the coke and coal reacts with oxygen from the heated air partially producing $CO_{(g)}$ (Partial Combustion) and completely producing $CO_{2(g)}$ (Full Combustion), according to the equations:

Partial Combustion $$C_{(coke,pci)} + \frac{1}{2} O_{2(g)} \rightarrow CO_{(g)}$$

$$R_{CO} = \frac{a}{1+a} R_{ave} \tag{78}$$

Full Combustion $$C_{(coke,pci)} + O_{2(g)} \rightarrow CO_{2(g)}$$

$$R_{CO_2} = \frac{1}{1+a} R_{ave} \tag{79}$$

The parameter *a* in the reaction rate equation is called Arthur's constant (ARTHUR, 1951) and is represented by:

$$a = 2500 \exp\left(\frac{-12400}{1.918\ T_{ave}} \right) \tag{80}$$

The average temperature of the gas-particle is defined as:

$$T_{ave} = \frac{T_{coke,pci} + T_g}{2} \tag{81}$$

With this constant, the division term that multiplies the reaction rate varies between 0 and 1, which controls the production of CO and CO_2 according to the temperature. Figure 4.2 below shows how the ratio behaves in a given temperature range.

Figure 4.2 – Arthur Constant ratio

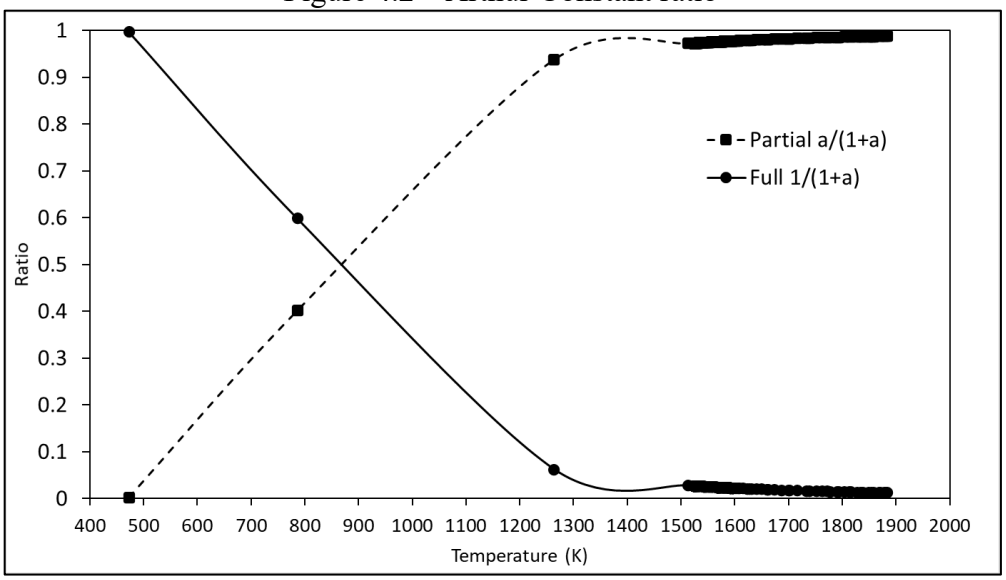

Source: author.

The overall rate of combustion for the Full and Partial reactions:

$$R_{\text{ave}} = \left(\frac{\alpha_g \rho_g \phi_{O_2}}{M_w^{O_2}} \right) \left\{ \frac{d_{\text{coke,pci}} \varphi_{\text{coke,pci}}}{A_{\text{coke,pci}} D_{O_2}^{\text{bulk}} \text{Sh}_{\text{coke,pci}}^{O_2}} + \frac{1}{\eta_{\text{ave}}^{O_2} k_{\text{ave}}} \right\}^{-1} \left[\frac{\text{kmol}}{\text{m}^3\text{s}} \right] \tag{82}$$

The Sherwood number is given by Equation (74) and the volumetric surface area of the particle is given by:

$$A_{\text{coke,pci}} = 6 \left(\frac{\alpha}{d\varphi} \right)_{\text{coke,pci}} \tag{83}$$

where φ is the particle shape factor and α the volume fraction.

The physical and chemical properties of the particle in the present model are influenced by the reactivity and pore structure, which will influence the overall reaction rate (CASTRO et al., 2005, BALTAZAR et al., 2006, TURKDOGAN, 1978). The model includes such properties in specific constants, η_{ave} and k_{ave} expressed as:

$$\eta_{\text{ave}}^{O_2} = \left(\frac{\frac{1}{\tanh(3\Theta)} - \frac{1}{3\Theta}}{\Theta} \right) \tag{84}$$

For the partial and full combustion reactions, the expression of k_{ave} is given by (MIYASAKA et al., 1968):

$$k_{ave} = RT_{ave} \exp\left(A - \frac{B}{T_{ave}} \right) \tag{85}$$

where R is the gas constant. The values of A and B are listed in Table 5.

The factor Θ is called the Thiele modulus (THIELE, 1939) and is expressed by:

$$\Theta = \frac{1}{6}(d_{coke,pci}\varphi_{coke,pci})\sqrt{\frac{k_{ave}}{D_{O_2}^{eff}}} \tag{86}$$

The intra-particle diffusion coefficient $D_{O_2}^{eff}$ is given by:

$$D_{O_2}^{eff} = \frac{\xi_{(coke,pci)}}{\tau_{(coke,pci)}} D_{O_2}^{bulk} \tag{87}$$

where the parameters $\xi_{(coke,pci)}$ and $\tau_{(coke,pci)}$ are respectively the particle's porosity and its tortuosity, which considered values were 0.7 and 0.8, following the Castro work. The bulk binary diffusion coefficient of oxygen is given by the kinetic theory, Equation (56), plus the turbulent term given by Equation (63).

The Solution Loss reaction rate is described using the diffusion mechanisms in mixtures and kinetic control (DE CASTRO et al., 2011, MACHADO et al., 2010), with the equation and rate described by:

Solution Loss $\qquad C_{(coke,pci)} + CO_{2(g)} \rightarrow 2CO_{(g)}$

$$R_{CO_2} = \left(\frac{\alpha_g \rho_g \phi_{CO_2}}{M_w^{CO_2}} \right) \left\{ \frac{d_{coke,pci}\varphi_{coke,pci}}{A_{coke,pci} D_{CO_2}^{bulk} \mathrm{Sh}_{coke,pci}^{CO_2}} + \frac{1}{\eta_{ave}^{CO_2} k_{CO_2}} \right\}^{-1} \left[\frac{\mathrm{kmol}}{\mathrm{m^3 s}} \right] \tag{88}$$

$$k_{CO_2} = \frac{k_1}{1 + k_2 P_{CO} + k_3 P_{CO_2}} \left(\rho \alpha \phi_C \right)_{(coke,pci)} 82.056 \times 10^{-3} T_g \tag{89}$$

where the formulation is similar to that presented for partial and full combustion. The parameters P_{CO} and P_{CO_2} are the partial pressures of CO and CO_2 gas species, respectively. Reaction constants, k_1, k_2, and k_3 are listed in Table 5. The partial pressure can be described in terms of the gas mixture properties expressed as (AUSTIN et al., 1997):

$$P_i = \frac{\rho_g R T_g}{M_{w,i}} \phi_i \tag{90}$$

The reaction rate due to water gas is described in a similar way to the solution loss reaction:

Water Gas $\qquad C_{(coke,pci)} + H_2O_{(g)} \rightarrow CO_{(g)} + H_{2(g)}$

$$R_{CO} = \left(\frac{\alpha_g \rho_g \phi_{H_2O}}{M_w^{H_2O}} \right) \left\{ \frac{d_{coke,pci} \varphi_{coke,pci}}{A_{coke,pci} D_{H_2O}^{bulk} Sh_{coke,pci}^{H_2O}} + \frac{1}{\eta_{ave}^{H_2O} k_{H_2O}} \right\}^{-1} \left[\frac{kmol}{m^3 s} \right] \tag{91}$$

$$k_{H_2O} = \frac{k_4}{1 + k_5 P_{CO} + k_6 P_{CO_2} + k_7 P_{H_2O}} \left(\rho \alpha \phi_C \right)_{(coke,pci)} 82.056 \times 10^{-3} T_g \tag{92}$$

For the coal combustion reactions, each particle is considered to be a reacting surface. The surface in the present study is considered to be constituted only by carbon. When the volatile content of the particle is completed depleted by the devolatilization, the char fraction begins to be consumed and converted to ash. In this process, the particle diameter and density can change during its passage through the reactor. For this reason, the final unit of the rate of particle surface species depletion must be kg/s. Therefore, the expressions above are multiplied by the particle volume and by the carbon molecular weight:

$$R_i^{surface} = R_i^{volumetric} M_w^{carbon} \frac{4}{3} \pi \frac{d_p^3}{8} \quad \left[\frac{kg}{s} \right] \tag{93}$$

The values for the kinetic rate constants are described in Table 5 below.

Table 5 – Parameters e kinetics rates constants used

Reaction	Pulverized Coal	Coke
$C_{(s)} + 0.5O_{2(g)} \rightarrow CO_{(g)}$ $C_{(s)} + O_{2(g)} \rightarrow CO_{2(g)}$	$k_{ave} = RT_{ave} \exp\left(8.784 - \frac{17260.8}{T_{ave}}\right)$	$k_{ave} = RT_{ave} \exp\left(8.89 - \frac{17980}{T_{ave}}\right)$
$C_{(s)} + CO_{2(g)} \rightarrow 2CO_{(g)}$	$k_1 = \exp\left(18.246 - \frac{24976.9}{T_{ave}}\right)$	$k_1 = \exp\left(15.78 - \frac{33392}{T_{ave}}\right)$
	$k_2 = \exp\left(-7.157 - \frac{9917.96}{T_{ave}}\right)$	$k_2 = \exp\left(-6.688 - \frac{10780}{T_{ave}}\right)$
	$k_3 = \exp\left(21.05 - \frac{47522.4}{T_{ave}}\right)$	$k_3 = \exp\left(31.615 - \frac{44372.4}{T_{ave}}\right)$
$C_{(coke,pci)} + H_2O_{(g)} \rightarrow CO_{(g)} + H_{2(g)}$	$k_4 = \exp\left(11.779 - \frac{32900}{T_{ave}}\right)$	$k_4 = \exp\left(16.65 - \frac{26320}{T_{ave}}\right)$
	$k_5 = 6.62$	$k_5 = 6.62$
	$k_6 = \exp\left(13.346 - \frac{18350}{T_{ave}}\right)$	$k_6 = \exp\left(13.346 - \frac{18350}{T_{ave}}\right)$
	$k_7 = \exp\left(35.244 - \frac{30143}{T_{ave}}\right)$	$k_7 = \exp\left(29.588 - \frac{36760}{T_{ave}}\right)$

Source: DE CASTRO et al., 2011.

5 METHODOLOGY AND BOUNDARY CONDITIONS

5.1 Raceway formation analysis

The work of RAJNEESH et al., 2004 was used to validate the raceway formation through the comparison of a correlation obtained from an experiment. The author evaluated the effect of various parameters using dimensional analysis and the π-theorem to obtain a correlation for the raceway depth. One experiment was designed to evaluate the depth of the raceway when gas is injected through a pipe into a domain filled with coke particles. The correlation equation and the experiment apparatus can be seen in Equation (94) and Figure 5.1 below:

$$D_r = 164\left(\frac{\rho_g v_b D_T^2}{\rho_{\text{eff}} g d_p H W}\right)^{0.8} \mu_w^{-0.25} D_T \tag{94}$$

Figure 5.1 – Scheme showing Rajneesh experimental device

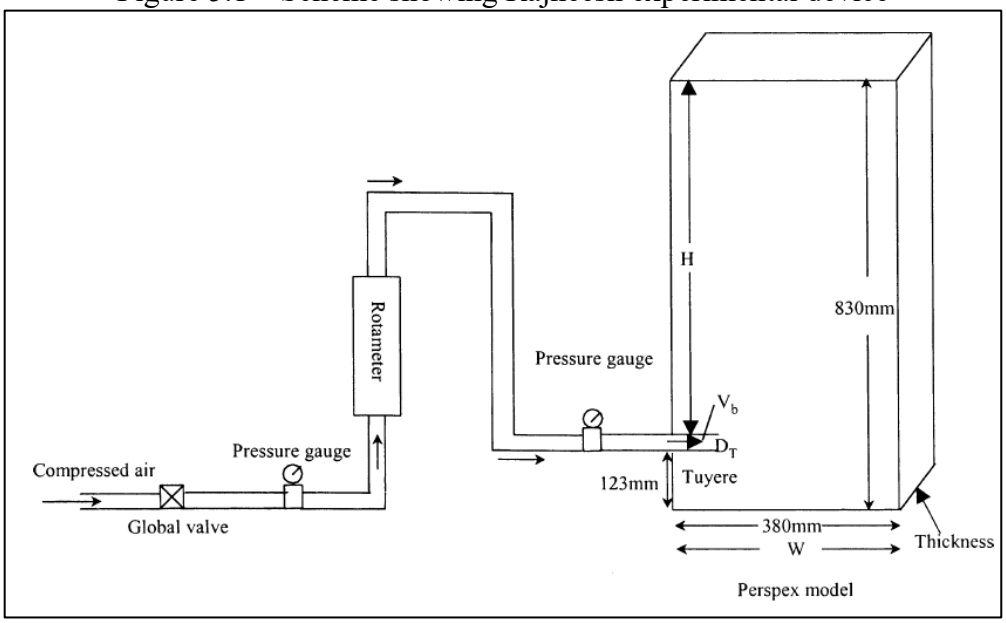

Source: RAJNEESH et al., 2004.

where D_r is the raceway depth, D_T is the tuyere diameter, ρ_{eff} is the effective density, ρ_g is the gas density, H is the bed height, W is bed width, d_p is the particle diameter, g is the acceleration due to gravity, v_b is the blast velocity, and μ_w is the wall friction coefficient. The effective density is calculated as:

$$\rho_{\text{eff}} = \rho_g \varepsilon + (1-\varepsilon)\rho_s \tag{95}$$

where ε is the void fraction of the bed and ρ_s is the density of the solid.

This approach of raceway depth analysis was already explored by numerous previous works (SELVARASU et al., 2006, WALKER et al., 2008, ZHOU, 2008, MA, 2017, OKOSUN et al., 2016, OKOSUN, 2018, WU et al., 2019). In those works, to be able to transfer the concept of the Eulerian Granular model to the simulation, the void fraction ε, or porosity, was converted to the unit minus the volume fraction, α, of the granular phase in the domain. Before the beginning of the simulation, the cell's within the domain were "filled" with coke volume fraction corresponding to the void fraction used by RAJNEESH et al., 2004, the void fraction of 0.5, makes the initial coke volume fraction domain start at 0.5. The present work considered a 2D approach of the domain. The measurement procedure can be seen in Figure 5.2.

Figure 5.2 – Procedure to measure the raceway depth after the simulation

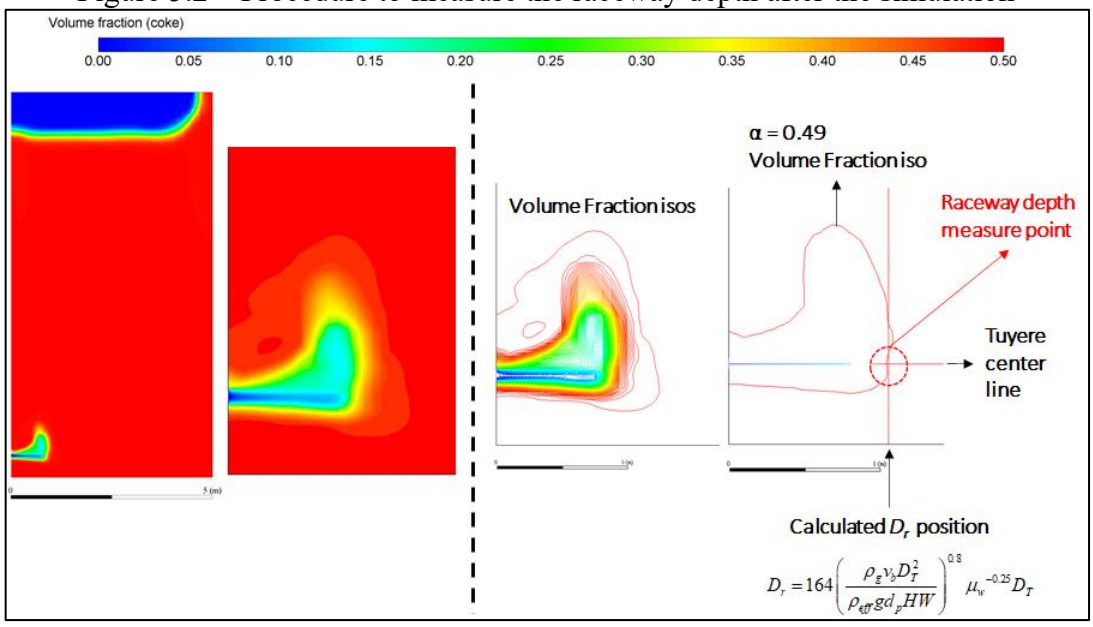

Source: author.

The left panel in Figure 5.2 illustrates the raceway shape simulation result for a determined setup. The right panel illustrates the volume fractions isolines and the chosen raceway depth point, which is the value of D_r calculated from Equation (95) and the tuyere center line intercept.

The geometry used can be seen in Figure 5.3 and a summary of the variables used in Equation (94) and (95) for the present study can be seen in Table 6.

Figure 5.3 – 2D geometry used in the raceway formation validation simulation

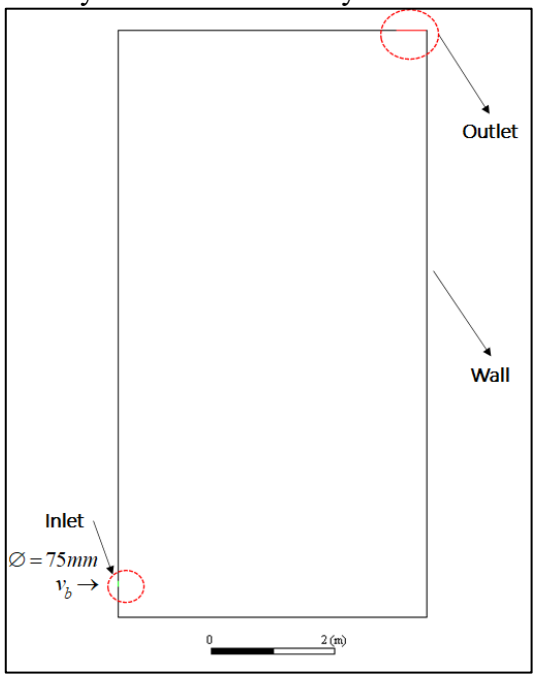

Source: author.

Table 6 – Parameters used in the raceway cavity formation simulation

Parameter	Unit	Values
Gas velocity variation (d_p = 30 mm)	m/s	150, 160, 170, 185, 200, 220
Coke diameter variation (v_b = 185 m/s)	mm	15, 20, 25, 30, 35, 38, 40
Void Fraction	-	0.5
Effective density	(kg/m^3)	350.3
Gas density	(kg/m^3)	0.6
Tuyere diameter	mm	75
Wall Fraction Coefficient	-	0.1
Bed height	m	8.4
Bed width	m	5

Source: author.

5.2 Raceway coke combustion analysis

The work of NOGAMI et al., 2004 was used to validate the coke combustion with a pre-simulated raceway cavity defined by the volume fraction of coke in the domain. Figure 5.4 illustrates the hot model device used by Nogami to study the combustion reactions

environment of the raceway and Figure 5.5 the geometry made at the symmetry place used in the present study.

Figure 5.4 – Nogami hot model experiment device scheme

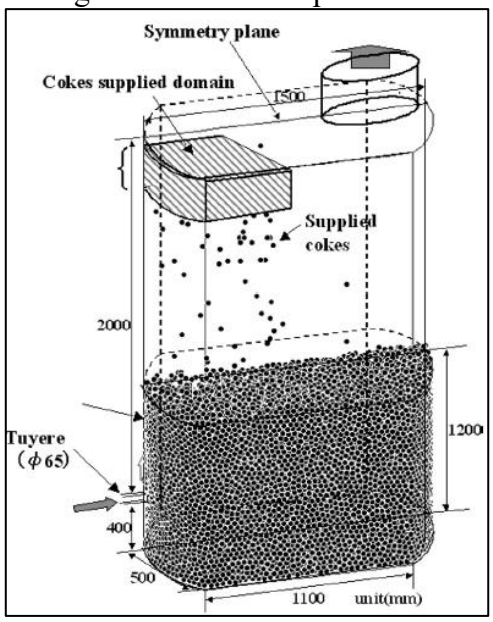

Source: NOGAMI et al., 2004.

Figure 5.5 – 2D geometry used in coke combustion

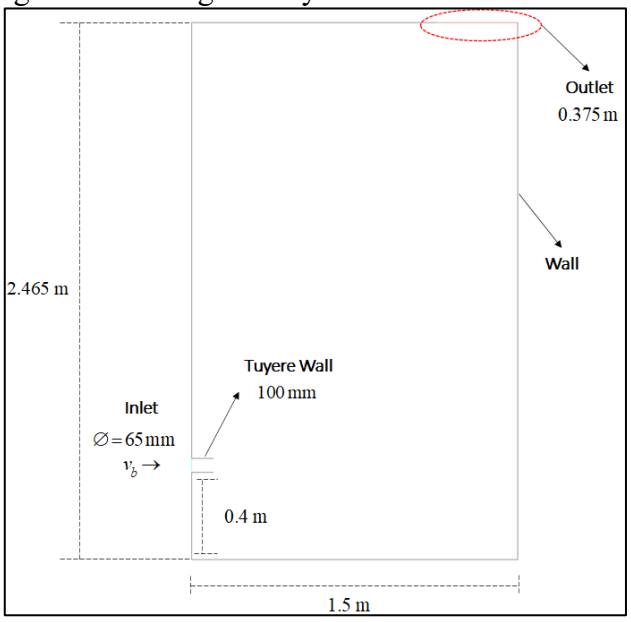

Source: author.

Nogami experiment consists of a domain filled with coke while a high-temperature blast injected through a tuyere supply enrichment oxygen to perform the coke combustion. Many works used Nogami hot model experiment to verify if their simulations provided proper results, including Zhou, Ma, Okoson, Wu, among others previously cited.

In the current study, the combustion was made after a raceway cavity has been formed. The energy equation is deactivated during this step. The cavity is defined as the result of the interaction between the coke bed and the high-speed blast injected through the tuyere. Figure 5.6 and Figure 5.7 below illustrate the raceway cavity applied, which is in agreement with Nogami and Zhou shapes (NOGAMI et al., 2004, ZHOU, 2008).

Figure 5.6 – Coke volume fraction used as a raceway in the combustion simulation

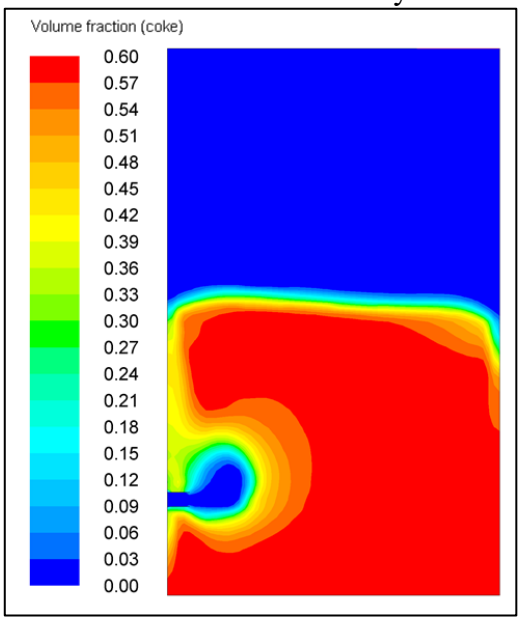

Source: author.

Figure 5.7 – Raceway cavity detail. The white dash line indicates x = 0.1 m to x = 1 m

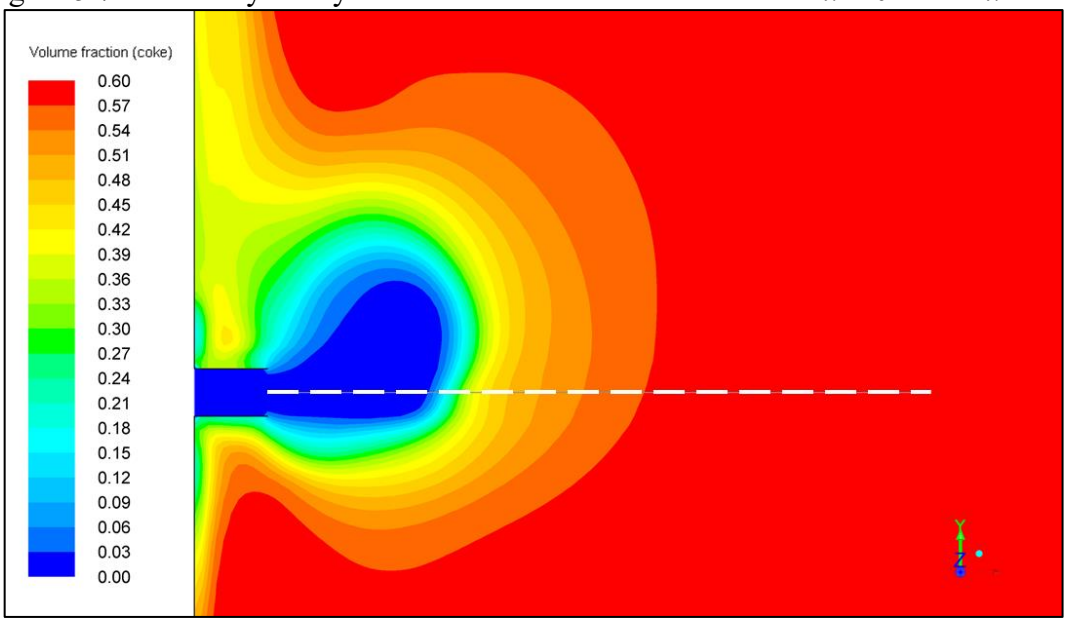

Source: author.

Figure 5.7 shows a zoom-in view of the raceway cavity simulated. One can observe the presence of one white dashed line at the center of the tuyere tip. This line marks the positions

from 0.1 to 1.0 meters and will be used to report the variables through plots in the results sections, as the next plot in Figure 5.8 below.

Figure 5.8 – Raceway cavity profile used in the analysis of the results

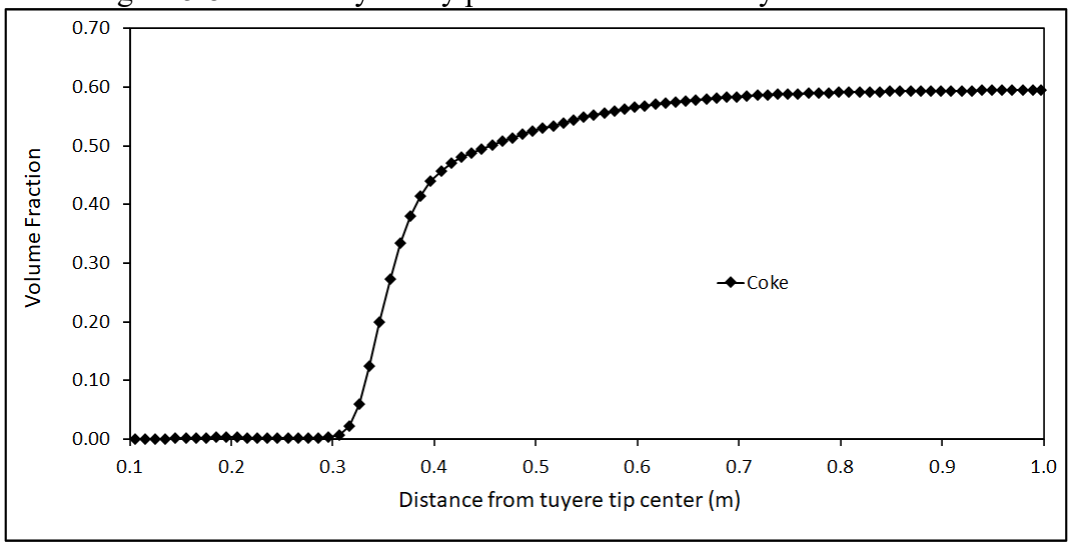

Source: author.

From the plot in Figure 5.8, one can observe that the coke volume fraction between the positions 0.3 and 0.4 meters is where there is a rapid increase, indicating that this is the position where the boundary was defined.

After the raceway formation, the volume fraction profile was saved and interpolated into a new simulation in which the energy equation is activated for the combustion. In the combustion simulation, the cavity is static, which is accomplished by the deactivation of the volume fraction equation.

From Table 7 to Table 9 the operating conditions, as well as the physical properties of coke, are described. As the present study split the combustion into Full and Partial combustion, the two reactions were considered. Also, for the homogeneous reactions, the eddy-dissipation model was used (section § 4.8.1.1), following Nogami`s work methodology.

Table 7 – Operating conditions for the 2D raceway combustion

Parameter	**Unit**	**Value**
Wind rate	Nm^3/h	700
Blast temperature	K	1073
Coke bed porosity	-	0.4
Coke bed volume fraction	-	0.6
Blast $\%O_2$	Mol/Mol	22
Blast $\%H_2O$	Mol/Mol	0.01

Source: NOGAMI et al., 2004 (adapted)

Table 8 – Coke physical properties

Parameter	**Coke**
Density (kg/m³)	1081
Shape Factor	0.7
Particle diameter (mm)	30
Thermal Conductivity	Equation (47)
Specific Heat	Equation (46)

Source: NOGAMI et al., 2004.

Table 9 – Reactions considered in raceway combustion

Homogeneous reactions (eddy-dissipation)
$CO_{(g)} + 0.5O_{2(g)} \rightarrow CO_{2(g)}$
$H_{2(g)} + 0.5O_{2(g)} \rightarrow H_2O_{(g)}$
Heterogeneous Reactions
$C_{(s)} + O_{2(g)} \rightarrow CO_{2(g)}$ (Full Combustion)
$C_{(s)} + 0.5O_{2(g)} \rightarrow CO_{(g)}$ (Partial Combustion)
$C_{(s)} + CO_{2(g)} \rightarrow 2CO_{(g)}$ (Solution Loss)
$C_{(s)} + H_2O_{(g)} \rightarrow CO_{(g)} + H_{2(g)}$ (Water Gas)

Source: NOGAMI et al., 2004.

5.3 Coal combustion analysis

The work from ZHANG et al., 2005 was used to validate the coal combustion model. Figure 5.9 illustrates the coal test rig apparatus.

Figure 5.9 – Coal Combustion device used by Zhang

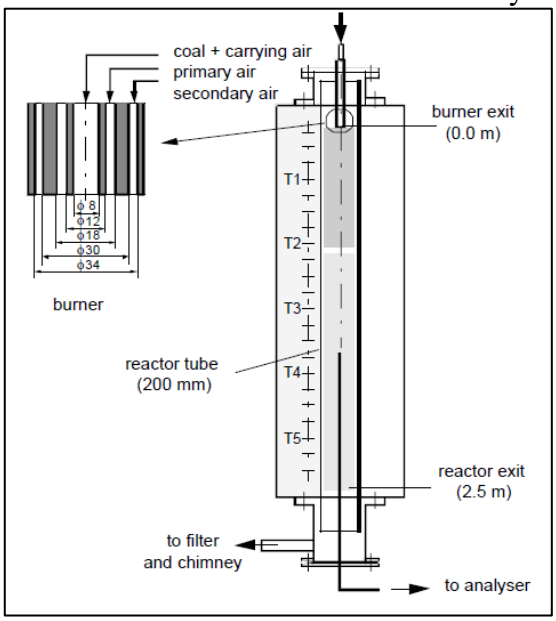

Source: ZHANG et al., 2005.

The experiment consists of a heated electrical reactor with five regulated heating zones. The reactor dimensions are 2.5 m long with a tube of 0.2 m diameter. The carrying air with pulverized coal enters the burner center, which is allied downward to make the particle fall due to gravity. The burner has a coaxial shape with 3 separate inlets that differentiate each other by their diameter, flow rate, and temperature in which the air is injected. This simulation was done using an axisymmetric 2D geometry from the center of the burner to the reactor exit. This type of geometry makes a rotation movement of one symmetry line that is allied to the *x*-axis. The axisymmetric approach of Zhang's experiment case was also used by the previously cited works, as well as other studies (WIJAYANTA et al., 2014a, WIJAYANTA et al., 2014b, ALGANASH et al., 2015).

Figure 5.10 illustrates the geometry used and Table 10 and Table 11 presents the operational conditions applied and reactions considered.

Figure 5.10 – 2D axisymmetric geometry used in the coal combustion analysis

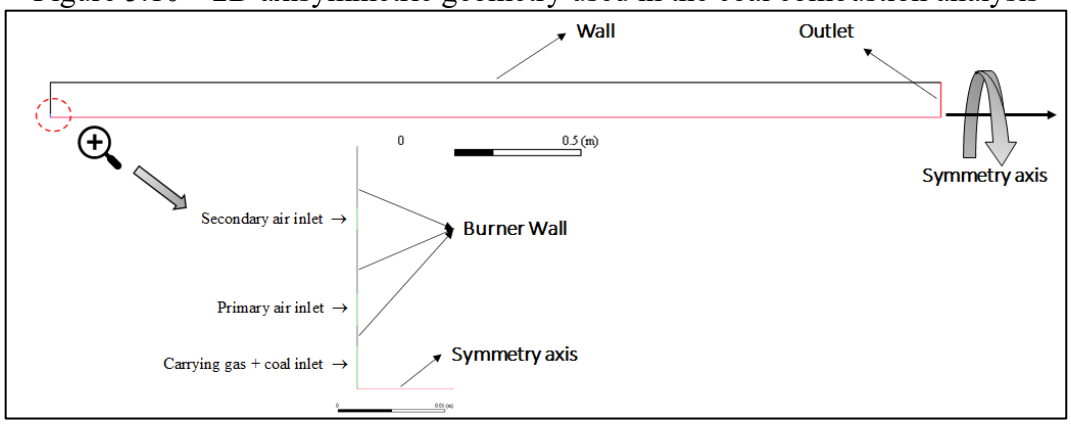

Source: author.

Table 10 – Coal combustion simulation parameters

Parameter	Unit	Value
Coal flow rate	kg/h	1
Wall temperature	K	1523
Coal carrying air flow rate	Nm^3/h	1.5
		0.000507
Carrying air temperature	K	473
Primary air flow rate	Nm^3/h	2.38
	kg/s	0.000902
Primary air temperature	K	523
Secondary air flow rate	Nm^3/h	5.33
	kg/s	0.0018
Secondary air temperature	K	623
Primary + secondary air flow rate	Nm^3/h	8
Coal size distribution (Mass Fraction)	µm	16 (30%), 52 (35%), 160 (25%), 350 (10%)
Devolatilization temperature	K	1200
Coal density	kg/m^3	1400

Source: ZHANG et al., 2005 (adapted).

Table 11 – Gas and Solid reactions applied

Homogeneous reactions
$Volatiles_{(g)} + \nu'_1 O_{2(g)} \rightarrow \nu''_2 CO_{2(g)} + \nu''_3 H_2O_{(g)} + \nu''_4 N_{2(g)}$
$H_{2(g)} + 0.5O_{2(g)} \rightarrow H_2O_{(g)}$
$CO_{(g)} + 0.5O_{2(g)} \rightarrow CO_{2(g)}$
Heterogeneous Reactions
$C_{(s)} + O_{2(g)} \rightarrow CO_{2(g)}$ (Full Combustion)
$C_{(s)} + 0.5O_{2(g)} \rightarrow CO_{(g)}$ (Partial Combustion)
$C_{(s)} + CO_{2(g)} \rightarrow 2CO_{(g)}$ (Solution Loss)
$C_{(s)} + H_2O_{(g)} \rightarrow CO_{(g)} + H_{2(g)}$ (Water Gas)

Source: author.

Table 12 – Coal analysis used

	Proximate Analysis, raw basis (%)				**Ultimate Analysis (%)**			
Coal	Moisture	Volatile	Ash	Fixed Carbon	C	H	N	O
1	1.57	30.46	6.67	62.87	78.9	4.9	1.3	7.6
2	1.69	31.94	10.74	57.32	74.2	4.4	1.2	8.2

Source: ZHANG et al., 2005.

5.3.1 Volatile molecular weight

The volatile molecular weight for the coals was calculated following the procedure described by ALGANASH, 2015.

The sum of each parameter for the proximate analysis of the coal 1 is expressed below:

$$\%moisture_{coal\ 1} + \%volatile_{coal\ 1} + \%ash_{coal\ 1} + \%FixedCarbon_{coal\ 1} = Total_{RawBasis}$$

$$1.57\% + 30.46\% + 6.67\% + 62.87\% = 101.6\%$$

Removing the ash and moisture percentages to be able to perform the calculus on a dry ash-free basis (DAF):

$$\%volatile_{coal\ 1} + \%FixedCarbon_{coal\ 1} = Total_{DAF}$$

$$30.46\% + 62.87\% = Total_{DAF}$$

$$\text{Total}_{\text{DAF}} = 93.33\%$$

Normalizing the values to 100%:

$$\%\text{volatile}_{\text{coal 1}}^{\text{Norm}} + \%\text{FixedCarbon}_{\text{coal 1}}^{\text{Norm}} = \%\text{Total}_{\text{DAF}}^{\text{Norm}}$$

$$\frac{\%\text{volatile}_{\text{coal 1}} \times 100}{\%\text{Total}_{\text{DAF}}} + \frac{\%\text{FixedCarbon}_{\text{coal 1}} \times 100}{\%\text{Total}_{\text{DAF}}} = 100\%$$

$$\frac{30.46\% \times 100}{93.33\%} + \frac{62.87\% \times 100}{93.33\%} = 100\%$$

$$32.64\% + 67.36\% = 100\%$$

Thus, the percentages of the volatile content and fixed carbon were obtained on a DAF basis.

The normalization of the proximate analysis for coal 1 is analogous to the one made for the ultimate analysis.

$$\%\text{C} + \%\text{H} + \%\text{O} + \%\text{N} = \%\text{Total}$$

$$78.9\% + 4.9\% + 1.3\% + 7.6\% = 93.3\%$$

Normalizing the values of the elements to 100%:

$$\frac{\%\text{C} \times 100}{\%\text{Total}} + \frac{\%\text{H} \times 100}{\%\text{Total}} + \frac{\%\text{O} \times 100}{\%\text{Total}} + \frac{\%\text{N} \times 100}{\%\text{Total}} = \%\text{Total}_{\text{Norm}}$$

$$\frac{78.9\% \times 100}{93.3\%} + \frac{4.9\% \times 100}{93.3\%} + \frac{1.3\% \times 100}{93.3\%} + \frac{7.6\% \times 100}{93.3\%} = 100\%$$

$$85.1\% + 5.3\% + 1.4\% + 8.2\% = 100\%$$

Considering a total mass of 1 gram of a mixture of carbon and volatile in a coal particle, the mass of volatile on a DAF basis is 0.32 gram. This value and the normalized proximate analysis could be used to calculate the relative proportion of elements in the volatile

mixture, released after the devolatilization. Assuming that all gases elements, hydrogen, oxygen, and nitrogen, will compose the volatile gas after the complete devolatilization with no losses, one can calculate the percentage of carbon by considering it a complement of the total mass released:

$$(\%\mathrm{C})M_w^{\mathrm{C}} + (\%\mathrm{H})M_w^{\mathrm{H}} + (\%\mathrm{O})M_w^{\mathrm{O}} + (\%\mathrm{N})M_w^{\mathrm{N}} = 0.32$$

$$\left(\frac{\mathrm{C}}{100}\right)\times 12 + \left(\frac{5.3}{100}\right)\times 1 + \left(\frac{8.2}{100}\right)\times 16 + \left(\frac{1.4}{100}\right)\times 14 = 0.32$$

$$\mathrm{C} = 0.178 = 17.8\%$$

Thus, the molecule of volatile matter in the gas phase mixture will have an elemental proportion of $C_{17.8}H_{5.3}N_{1.4}O_{8.2}$. Dividing each element percentage by its molecular weight results in $C_{1.478}H_{5.244}N_{0.1}O_{0.512}$. Normalizing using the carbon fraction present in the molecule as reference: $C_{1.478/1.478}H_{5.244/1.478}N_{0.1/1.478}O_{0.512/1.478}$. Finally, the molecular form of the volatile matter in coal 1 can be expressed as $CH_{3.548}N_{0.068}O_{0.347}$.

The calculation procedure performed for coal 2 will give a molecular formula of $CH_{2.964}N_{0.058}O_{0.348}$.

With the molecular formula, the molecular weight for coal 1 can then be calculated by:

$$M_w^{\text{Volatiles coal 1}} = M_w^{\mathrm{C}}\times 1 + M_w^{\mathrm{H}}\times 3.548 + M_w^{\mathrm{N}}\times 0.068 + M_w^{\mathrm{O}}\times 0.347$$

$$M_w^{\text{Volatiles coal 1}} = 12\times 1 + 1\times 3.548 + 14\times 0.068 + 16\times 0.347 = 22.0844\left[\frac{\mathrm{kg}}{\mathrm{kmol}}\right]$$

And for the coal 2:

$$M_w^{\text{Volatiles coal 2}} = M_w^{\mathrm{C}}\times 1 + M_w^{\mathrm{H}}\times 2.964 + M_w^{\mathrm{N}}\times 0.058 + M_w^{\mathrm{O}}\times 0.348$$

$$M_w^{\text{Volatiles coal 2}} = 12\times 1 + 1\times 2.964 + 14\times 0.058 + 16\times 0.348 = 21.3813\left[\frac{\mathrm{kg}}{\mathrm{kmol}}\right]$$

With the volatiles molecular weight, the coal calculator from FLUENT was used to balance the stoichiometric for the volatiles combustion reaction resulting in the equation below:

$$\text{Volatiles}_{(g)}^{\text{coal 1}} + 1.71O_{2(g)} \rightarrow CO_{2(g)} + 1.77H_2O_{(g)} + 0.034N_{2(g)}$$

$$\text{Volatiles}_{(g)}^{\text{coal 2}} + 1.567O_{2(g)} \rightarrow CO_{2(g)} + 1.482H_2O_{(g)} + 0.029N_{2(g)}$$

5.4 Coke and coal combustion

To test both models at the same time, the coke and coal combustions were submitted to a 2D blast furnace slice simulation. The operation and geometry parameters were taken from a literature work made by WU et al., 2019. The author used ANSYS-FLUENT to investigate in detail the effect of the PCI particle diameters coupled with coke combustion and raceway profile change.

The present work will use the fact that Wu also used the granular model to simulate the raceway cavity and perform a simplified computation to verify if the models that were validated in the present work would work in synergy when submitted to actual blast furnace operating conditions, and achieve a minimally set of satisfactory results. Figure 5.11 illustrates a scheme of the blast furnace coke bed and Deadman zone region from the reference literature work, and Figure 5.12 the adapted geometry used in the present study.

Figure 5.11 – Dimensions of the lower part of blast furnace

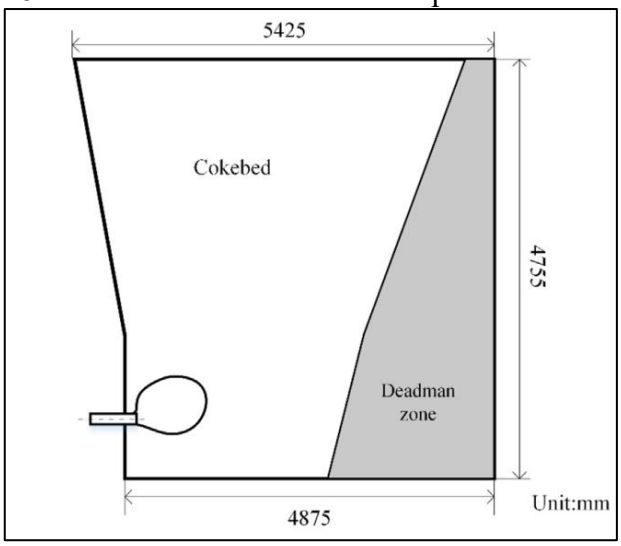

Source: WU et al., 2019

Figure 5.12 – Adapted dimensions from Wu study

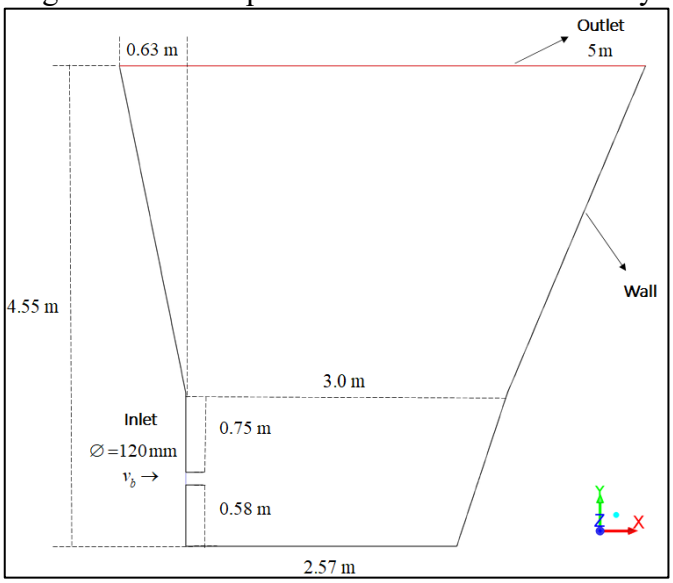

Source: author.

The adaptation tried to preserve to its maximum the original characteristics from Wu geometry, but some assumptions were made. Starting with the measurements presented in Figure 5.11, some approximations were taken and the distances are presented in Figure 5.12. The author considered only the cokebed region, and the boundary between it and the deadman zone was considered a wall. The present work also made use of such assumptions. The tuyere at the low part of the geometry was considered to have a wall that extends 160 mm towards the *x*-axis (similar to the one considered in Nogami validation geometry, Figure 5.5), which is not shown in Figure 5.12 to facilitate the view of the measurements near the inlet.

The mesh used at the coke and PCI combustion using Wu geometry can be seen in Figure 5.13 below.

Figure 5.13 – Mesh used on the coke and PCI combustion

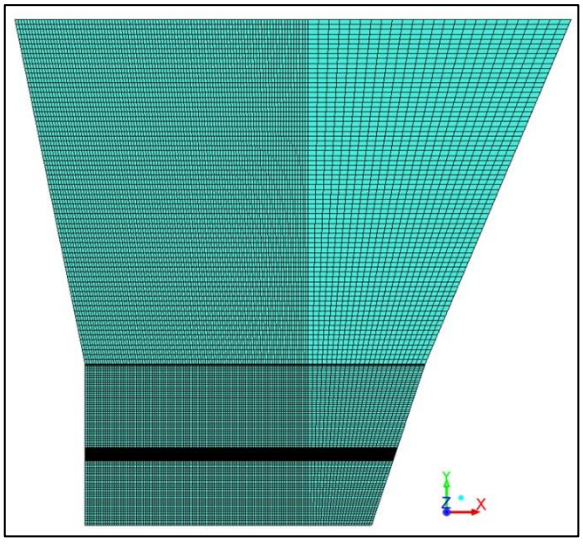

Source: author.

The grid was refined close to the gas inlet, where there is the majority of the gradients, and coarse at the outlet by the northeast. A total of 20856 quadrilateral elements, between uniform and non-uniform, were used.

As the objective of the simulation is to verify the coke and coal combustion reaction rates, the PCI lance was not considered in detail. The coal was considered to be injected from an inlet located at the center of the blast inlet through a slot width equal to the lance diameter, which is 14 mm. With this consideration, coal particles were also assumed to enter the domain at the same temperature as the blast.

The coal particle diameter distribution was considered to follow a Rosin-Rammler regression with the same parameters considered by Wu.

The model assumes that there is a relation between the resultant mass fraction and an exponential of the particle size, a mean diameter, and the spread parameter (RAO, 2016, ANSYS, 2017c). The relationship can be expressed as:

$$Y_d = \exp\left[-\left(\frac{d}{\overline{d}}\right)^{\alpha}\right] \tag{96}$$

where Y_d is the particle mass fraction for a particle diameter greater than d (retained fraction), $\overline{d}$ is the mean diameter, and α is the spread parameter. The spread parameter can be calculated using the expression and the previously fitted data:

$$\alpha = \frac{\ln\left(-\ln Y_d\right)}{\ln\left(d / \overline{d}\right)} \tag{97}$$

The regression was made using a fitting methodology proposed by DOLL, 2014, using Wu size distribution plot. Figure 5.14 below plots the diameter distribution obtained.

Figure 5.14 – Rosin-Rammler distribution

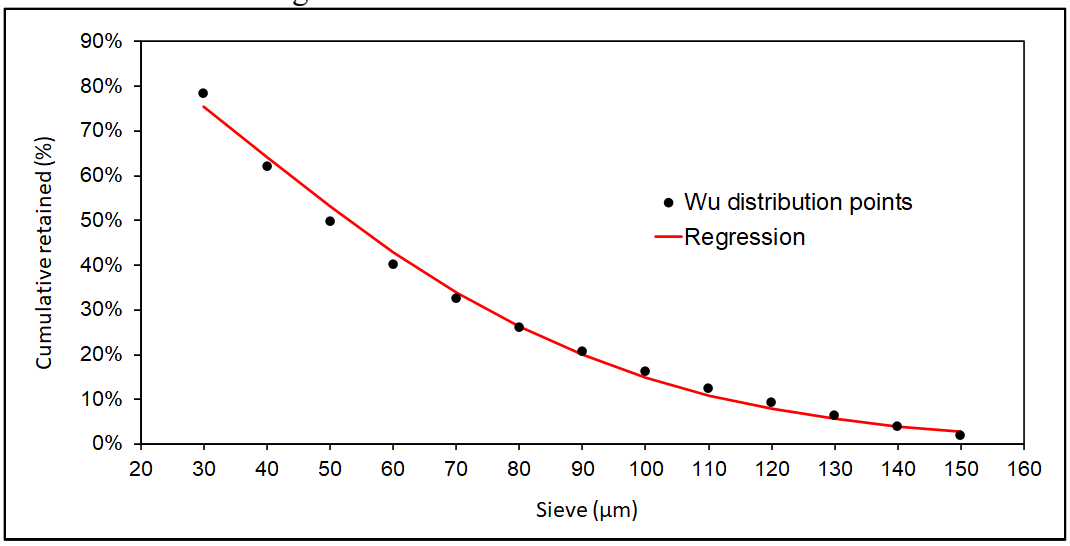

Source: author.

The raceway used for the blast furnace simulation was computed previously without the combustion influence. Initially, the cokebed started at a height of 2.5 meters and a volume fraction of 0.6.

The simulation was carried out similar to the Nogami validation. First, the domain is "filled" with coke, at a volume fraction equal to 0.6. After, the cavity is formed by the gas passage. Figure 5.15 below illustrates the cavity obtained.

Figure 5.15 – Coke volume fraction used as a raceway at the blast furnace combustion

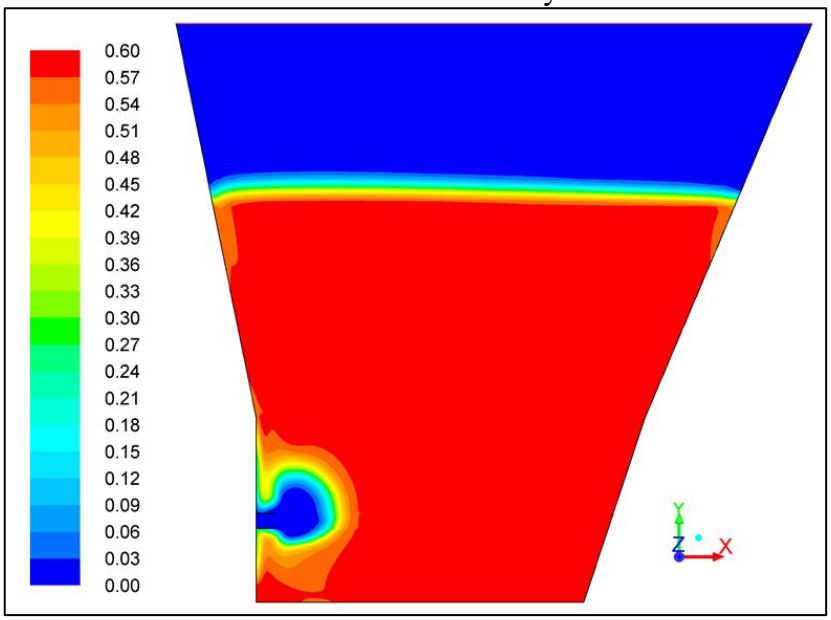

Source: author.

After the raceway profile has been obtained, the result is interpolated to a new simulation to be able and submit to the combustion process.

The main parameters used from the work of Wu can be seen in Table 13 to Table 15 below.

Table 13 – Operational parameters used at the blast furnace simulation

Parameter	Unit	Value
Number of tuyeres	-	26
Tuyere diameter	mm	120
Tuyere length	mm	160
Blast temperature	K	1408
Blast pressure	kPa	371
Blast rate	Nm^3/min	3800
Oxygen enrichment rate	wt%	3.5
Coal inlet	mm	14
PCI rate	Nm^3/min	800
Coke density	kg/m^3	900
Volatile Molecular Weight	kg/kmol	47.2

Source: WU et al., 2019 (adapted).

Table 14 – Coal analysis used at the blast furnace simulation

Proximate Analysis, raw basis (%)				Ultimate Analysis (%)			
Moisture	Volatile	Ash	Fixed Carbon	C	H	N	O
2.61	13.75	15.14	68.49	80.20	3.71	3.22	4.49

Source: WU et al., 2019 (adapted).

Table 15 – Rosin-Rammler parameters used at the blast furnace simulation

Parameter	Unit	Value
Mean diameter (OKOSUN, 2018)	μm	66.663
Min. diameter	μm	20
Max. diameter	μm	150
Spread Parameter	-	1.58564
Number of diameters	-	10

Source: WU et al., 2019 (adapted).

5.5 Numerical methods

The solution method for the cases in the present study used the academic version of ANSYS FLUENT 16.0 software, which uses the finite volume method. Because each case has its particularities, such as the number of equations, discretization, gradient option, 2D space, and solution strategy, the methodology of each case varied from one to another.

Although they possess differences, similarities are present. For all cases, the pressure-based segregated solver was used. This type of solver uses pressure-velocity coupling to solve the equations, one equation at a time (conservation of mass, momentum, energy, turbulence, radiation, chemical species). This approach manipulates the mass and momentum equations to obtain a pressure correction equation, which is used to compute the pressure field. After that, the fluxes, pressure, and velocity fields are updated. Then, additional equations are then solved sequentially, and the last step is the convergence check. Figure 5.16 below illustrates the steps.

Figure 5.16 – Scheme of the pressure-based solver approach

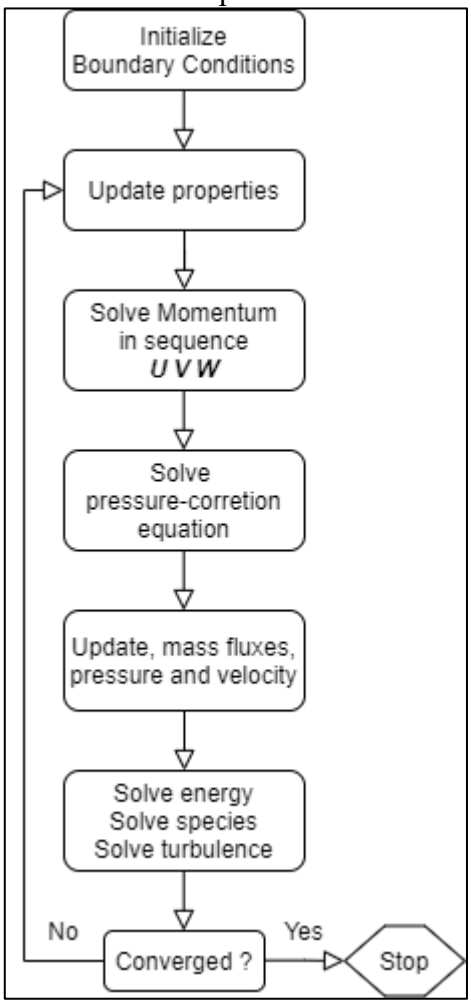

Source: ANSYS, 2017b (adapted).

For the pressure-velocity coupling, the SIMPLE (Semi-Implicit Method for Pressure linked equations) algorithm was used in all the cases. The SIMPLE algorithm makes use of the pressure-velocity coupling through algebraic manipulation to enforce mass conservation and to obtain the pressure field.

The discretization of species, energy, turbulence (k and ε), radiation, and momentum equations employed the upwind scheme. For the raceway formation and combustion, the first-order discretization was used, and for the coal combustion, the second-order discretization.

The gradients were evaluated using the Green-Gauss cell-based method for raceway formation and combustion, and the least square cell-based method was used for the coal combustion (ANSYS, 2017b).

The raceway formation simulation was carried out in a transient approach in a 2D planar space at the vertical symmetry plane of the domain. In all the cases, an ending time of 1 s was established. This was observed to be sufficient to achieve a low value of residuals (in an order of 10^{-5}) and a proper cavity shape. Default under-relaxation factors were used.

For the coke combustion reactions based on Nogami`s experiment, a transient approach in 2D planar at the vertical symmetry plane was also used. First, the simulation was carried out in a lower time-step, 0.01 s. After the flow field and reactions have been taken place with lower residuals (order of 10^{-4} in the continuity and 10^{-6} in the other equations), the time-step was increased to 0.1, 0.5, and 1 second, until the species field and temperature field converged and the values have been stabilized. Default under-relaxation factors were used.

The coal combustion simulation was carried out in a steady-state approach in an axisymmetric 2D space and had two steps. First, the flow field was initiated without particles, reactions, and radiation for 500 iterations. After, the second step was the introduction of the particles, reactions, and radiation. The second step proceeded for 500 iterations, where the convergence has been achieved with residuals in an order of 10^{-4}. Default under-relaxation factors were used.

Finally, the blast furnace simulation was done following the coke combustion simulation previously described, with the coal particles being injected at the start of the simulation, with a low time-step at first, progressing gradually until the solution was converged with residuals in order of 10^{-5}.

6 RESULTS AND DISCUSSION

6.1 Raceway formation

The results obtained from the CFD simulation and the raceway depth obtained from the Equation (94) for particle diameter variation using a constant gas velocity of 185 m/s can be seen in Figure 6.1.

Figure 6.1 – Raceway correlation and present study varying coke particle diameter

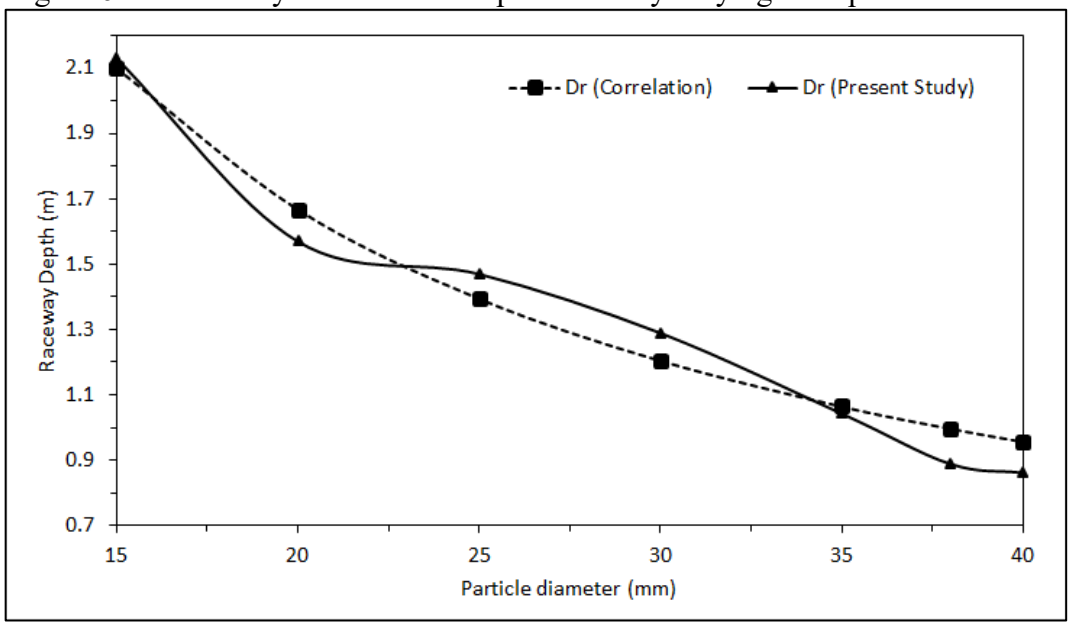

Source: author.

The maximum error observed had a value of 11% at a diameter of 38 mm and the minimum error of 2% at the diameters of 15 and 35 mm. The maximum depth obtained by the simulation was 2.13 m (15 mm particle diameter) and a minimum of 0.86 m (40 mm particle diameter).

One can notice that with diameter increase, the curve concavity changes signal from positive to negative. This could be related to the transient feature of the problem, which can change the shape of the raceway from diameter to diameter, changing the concavity of the curve. Figure 6.2 illustrates the fluidized bed after 1 second of the simulation.

Figure 6.2 – Volume fraction contour after 1 second. Coke particles diameter variation. a) 15, b) 20, c) 25, d) 30, e) 35, f) 40, in mm

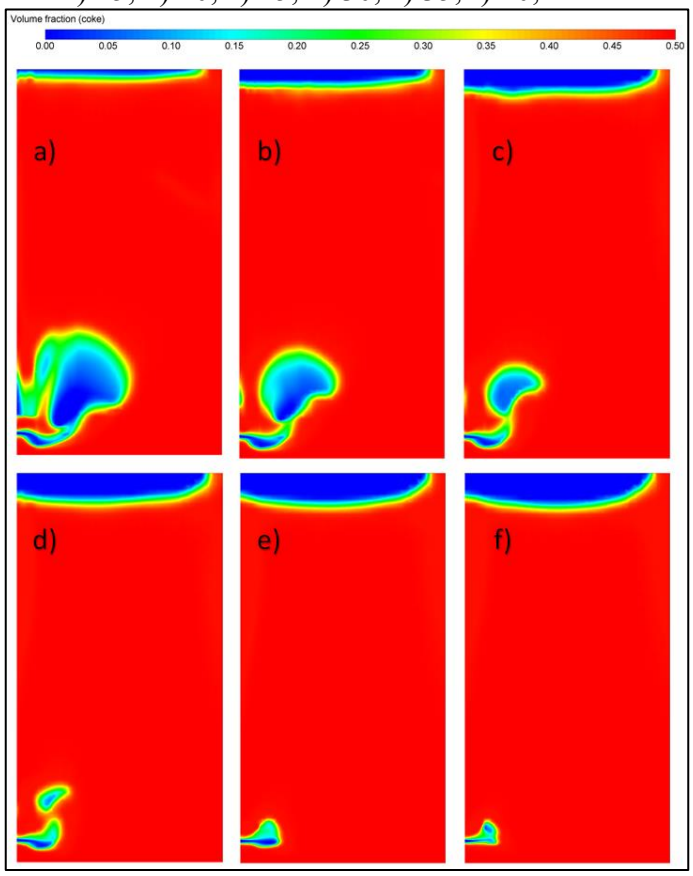

Source: author.

Figure 6.2 shows that a high bubble of air is formed for lower diameters, and as the diameter increases, the bubble size decreases.

A similar analysis was made varying the velocity of the gas. The plot of raceway depth versus gas velocity using a constant coke diameter of 30 mm can be seen in Figure 6.3.

Figure 6.3 – Raceway correlation and present study varying gas velocity

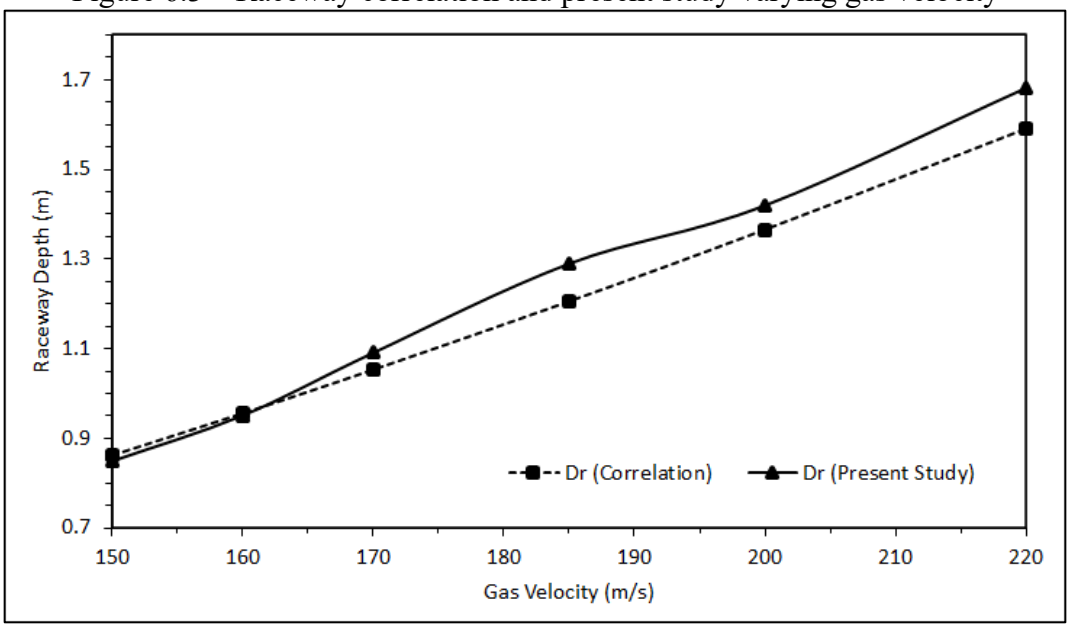

Source: author.

The maximum error observed had a value of 7% at a velocity of 185 m/s and the minimum error of 0.4% at the velocity of 160 m/s. The maximum depth obtained by the simulation was 1.68 m (220 m/s gas velocity) and a minimum of 0.85 m (150 m/s gas velocity).

In Figure 6.3, one notes that for high values of gas velocity, the correlation seems to diverge from the CFD prediction in a raceway depth value of about 200 mm. Even so, the velocity simulation obtained a less error rate than the diameter simulation. Figure 6.4 illustrates the bubble evolution with the velocity increasing.

Figure 6.4 – Volume fraction contour after 1 second. Gas velocity variation.
a) 150, b) 160, c) 170, d) 185, e) 200, f) 220, in m/s

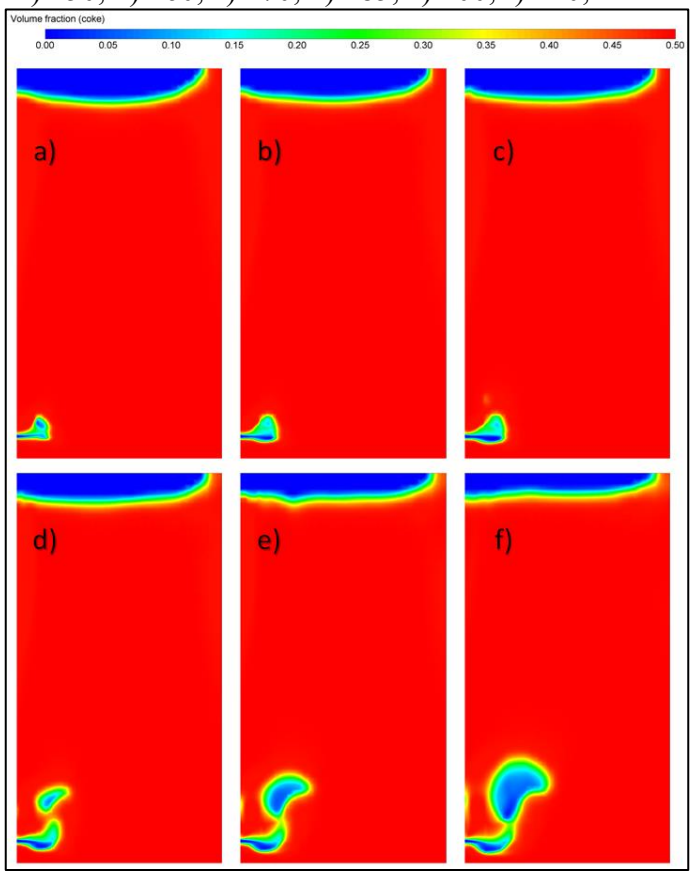

Source: author.

Comparing Figure 6.2 to Figure 6.4, one can notice that the diameter affects more the bubble size than the velocity, considering the presented values and 1-second simulation. To fully investigate this effect, a wide range of velocities and diameters should be simulated.

6.2 Raceway combustion

The following section will cover the validation of the coke combustion based on experiment results, which were the species molar fraction produced during the combustion process. Also, to support the model results, an analysis of relevant parameters will be made, such as temperature, flow field, reaction rates.

6.2.1 Validation

The coke combustion was validated by comparison between the results with both simulation and experiments results made by NOGAMI et al., 2004. Figure 6.5 and Figure 6.6 below illustrate the results in terms of the gas species molar fractions.

Figure 6.5 – Present study vs experiment – species molar fraction

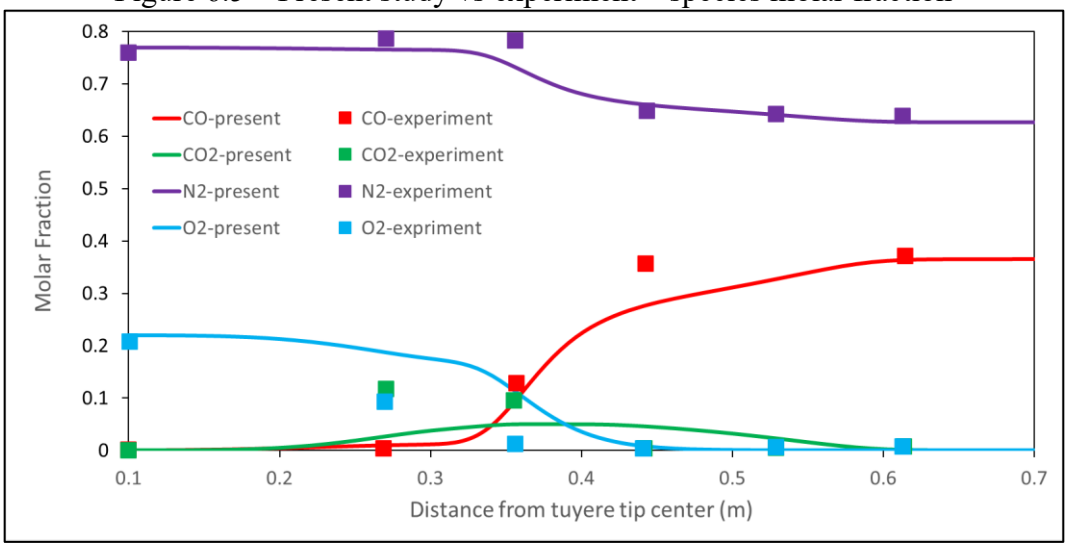

Source: author.

Figure 6.6 – Present study versus Nogami simulation – species molar fraction

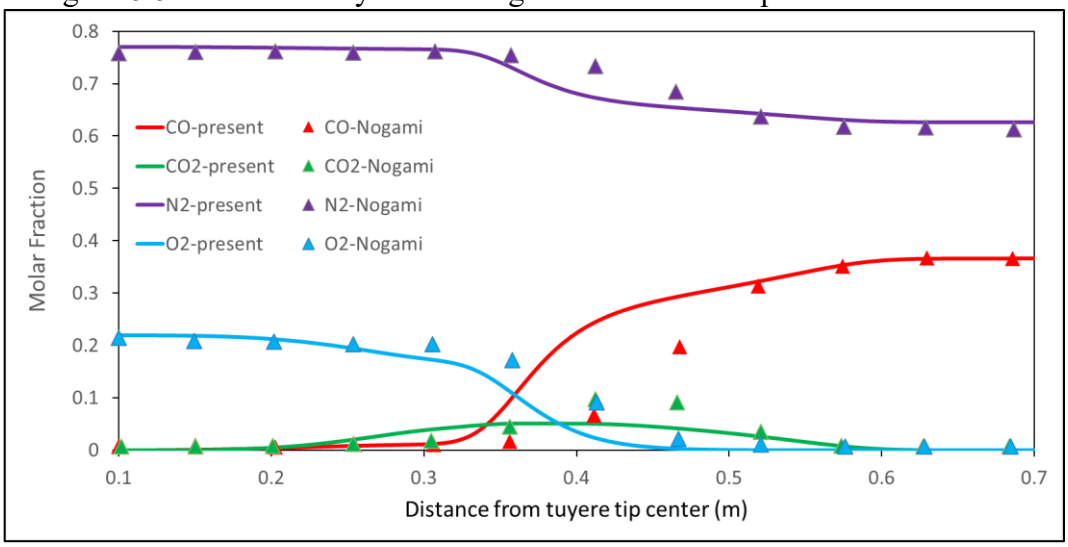

Source: author.

In both figures, the molar fraction relative to H_2 species was omitted to facilitate the view, as its results were almost zero, the same result reported by Nogami. H_2 molar fraction will be presented in the forward's contour maps. As one can see, the plots are in agreement in both trends and magnitudes with experiment and simulation.

The curve deviation from the points is related to the raceway cavity shape. As the cavity precise profile was not obtained, the reactions are going to take place in different locations, making the species molar fraction vary slightly from Nogami results in the location that are being analyzed (tuyere tip).

Next, Figure 6.7, Figure 6.8, and Figure 6.9 illustrate the contour maps relative to each gas species considered in the domain.

Figure 6.7 – CO and CO_2 mole fractions

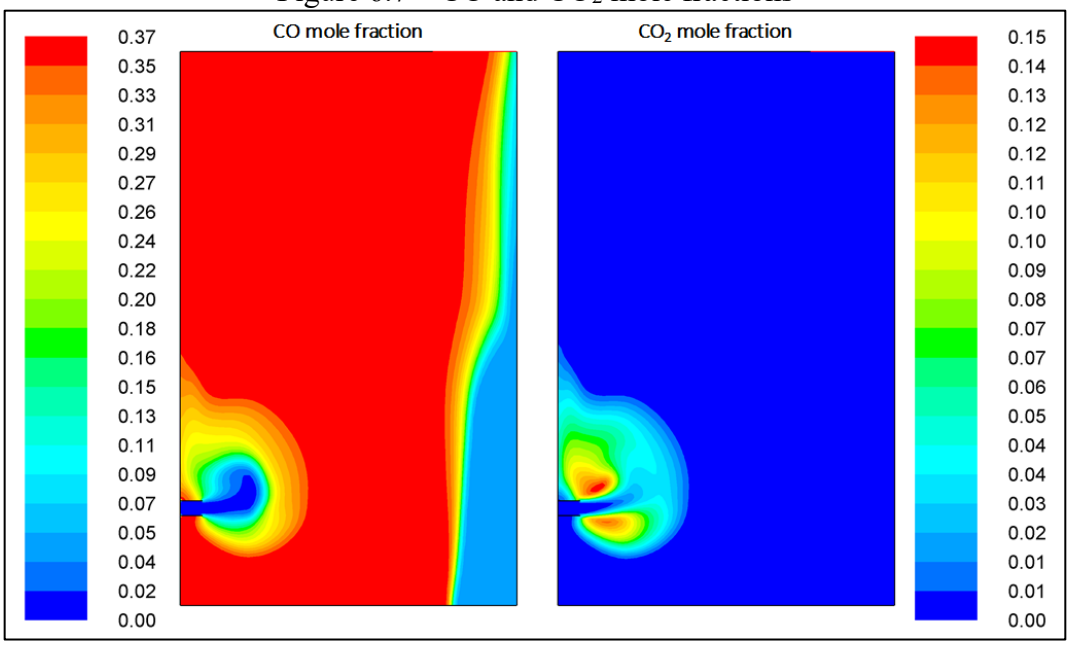

Source: author.

Figure 6.8 – O_2 and N_2 mole fractions

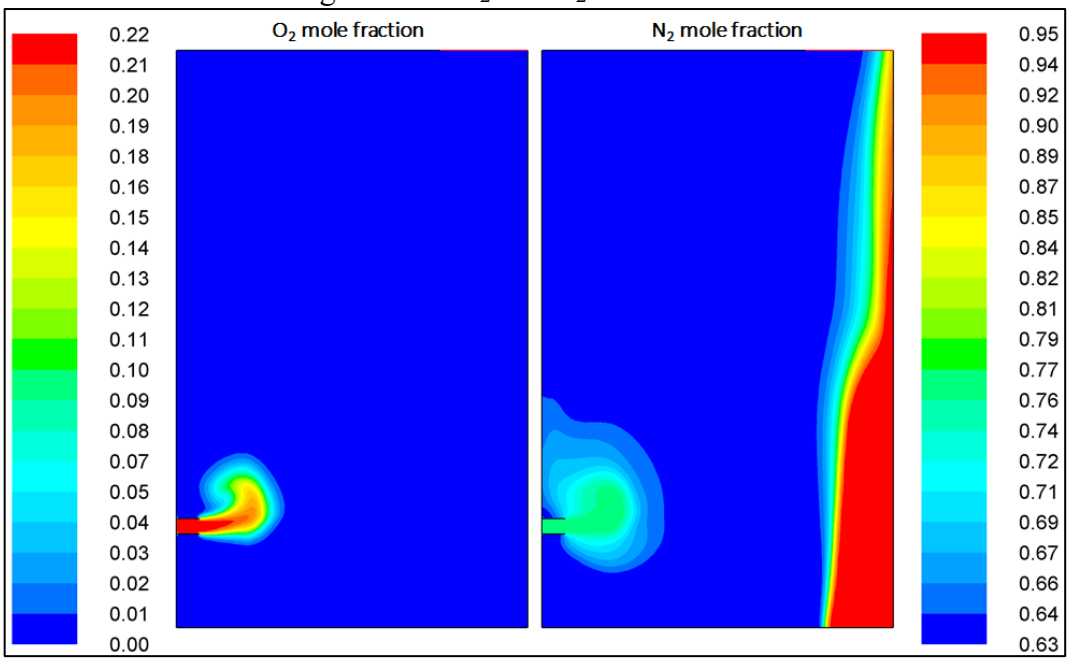

Source: author.

Figure 6.9 – H_2 and H_2O mole fractions

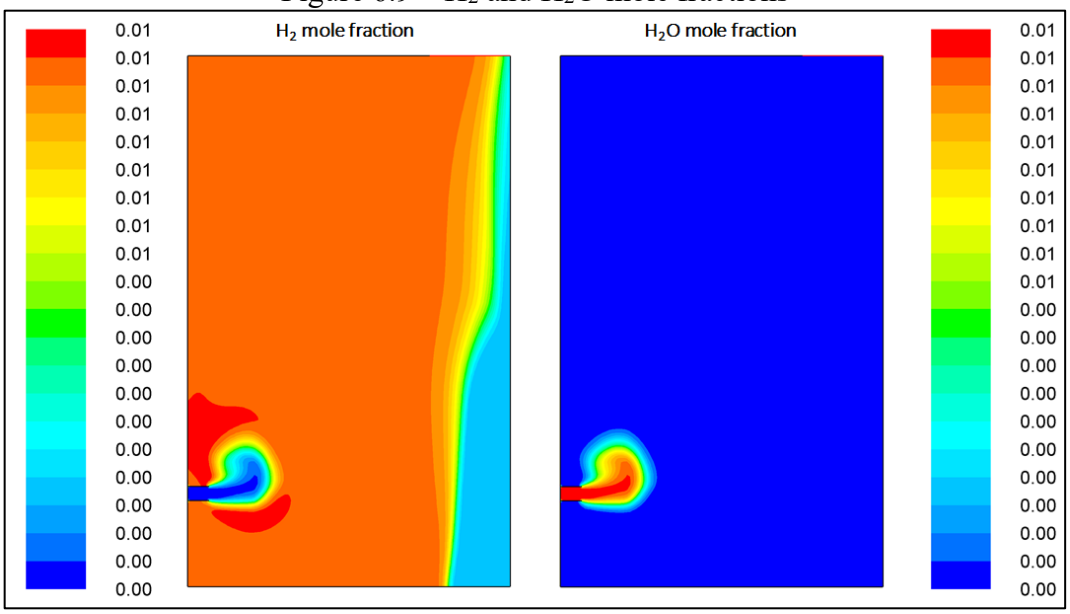

Source: author.

Observing the contours, one can see that the magnitude of the species molar fraction only varies significantly in the raceway neighborhood. For deeper locations into the domain, the steady-state is reached, and fractions remain constant. The posterior analysis will cover the mechanism that acts in the raceway surrounding area and its impact on each species.

6.2.2 Mesh independence study

To verify the sensibility of the solution according to the mesh, a grid independence study was made. The test was carried out using 6 grids which varied between 3588 to 57408 control volumes. All the grids used were two-dimensional composed of irregular quadrilaterals. The grids and the geometries were generated using ICEM-CFD software.

The strategy chosen on ICEM-CFD was to generate the grids by blocking. This approach can be briefly described as follows: the geometry is divided into blocks which will generate the mesh according to the parameters chosen for each block. The present study used the edges of the geometry to set how many elements the block would have in that specific edge. Then, the number of elements in the first edge was copied to all parallel block edges in the geometry. Figure 6.10 and Figure 6.11 below illustrate one of the grids generated.

Figure 6.10 – Grid with 18832 control volume used

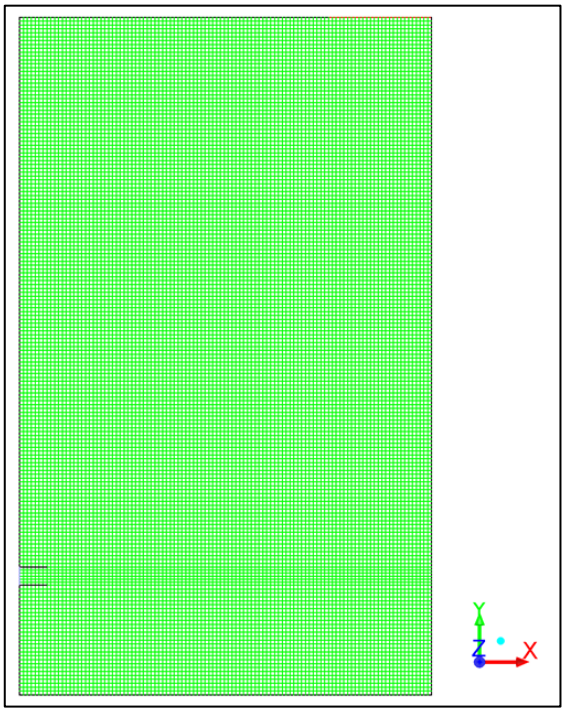

Source: author.

Figure 6.11 – Gas inlet detail for the 18832 control volume grid

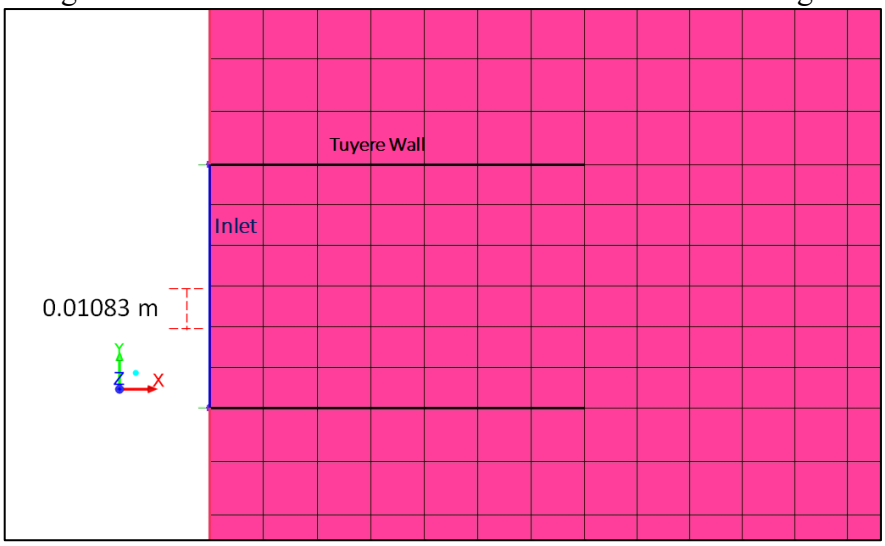

Source: author.

The strategy for the study was to start from a coarse mesh, with 3588 elements, and then progress the refinement until the results showed a low variance and agreement with the data used for the validations. The main parameters for each grid are summarized in Table 16.

Table 16 – Raceway combustion mesh independence study parameters

Mesh name	Total Quadrilateral. Elements	Elements: gas inlet	Elements: outlet	Elements: wall	Elements: wall tuyere
58k	57408	8	48	936	24
33k	32292	6	36	702	18
24k	23760	6	30	600	16
19k	18832	6	27	533	14
14.8k	14352	4	24	468	12
3.8k	3588	2	12	234	6

Source: author.

As one can see, each edge from the geometry varied according to the refinement. The results from the 3.8k mesh were very poor if compared to the others, which is expected once it is the coarser grid. The mesh 14.8k was made in a global refinement of the previous grid, to increase the total number of nodes of each edge by a factor of 2. Following this procedure, the mesh 33k is made by a global refinement of the mesh 3.8k by a factor of 3, and the 58k mesh by a factor of 4. The mesh 33k presented good results with a relatively low simulation time, therefore, was chosen to produce grids with the same gas inlet number of elements that could achieve the same results with fewer elements, originating the grids 24k and 19k.

Figure 6.12 and Figure 6.13 below show the gas temperature and CO mole fraction from the tuyere tip center for each grid described in Table 16.

Figure 6.12 – Raceway combustion grid study: gas temperature variation

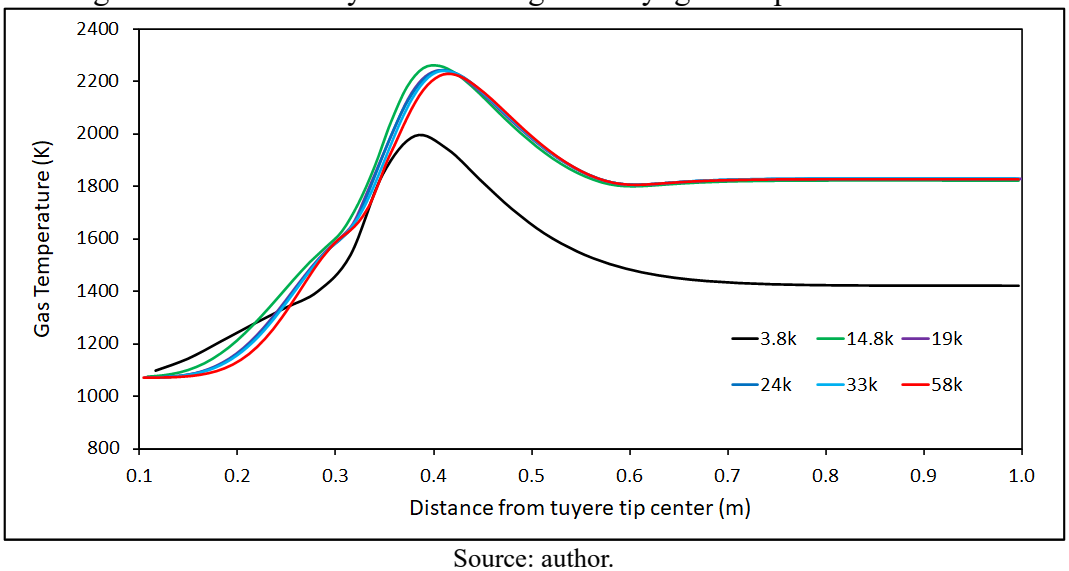

Source: author.

Figure 6.13 – Raceway combustion grid study: CO molar fraction variation

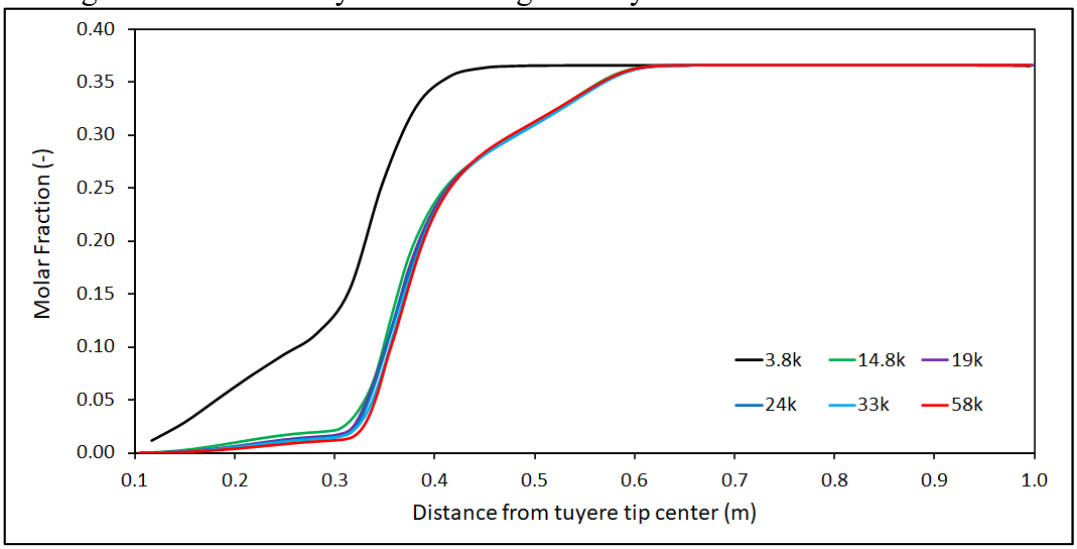

Source: author.

From the figures, one can notice that the curves relative to the grid 3.8k are very far from the other curves, which is expected by the level of refinement of the mesh. The other grids showed reasonability in their results with small deviations at the raceway region, between 0.2 and 0.4 meters, where the majority of the gradients are present, and almost no deviation after.

Based on the curves, we can infer that grids with control volumes greater than or equal to 14352 are appropriate. To be conservative, and at the same time being reasonable once this simulation demanded a high number of timesteps to be finished (1000 seconds of simulation time on average with a time step size of 0.01 to 1 second), the grid with 18832 cells (19k) was chosen to report the results.

The residuals were capable to reach values in an order of 10^{-5}. Figure 6.14 illustrates the residuals after a time-step modification for the 19k grid.

Figure 6.14 – Residuals plot – 19k grid

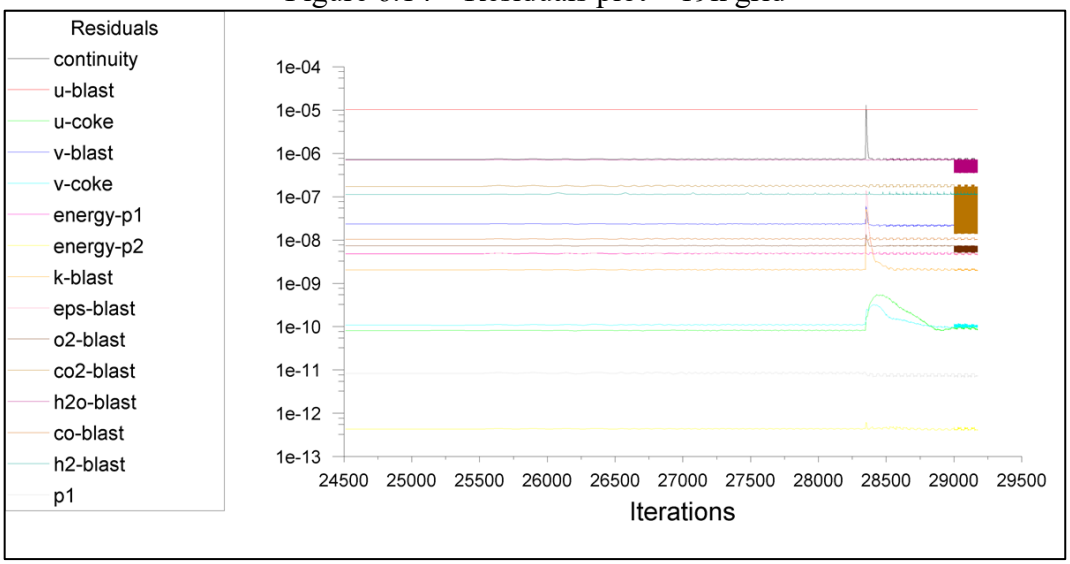

Source: author.

6.2.3 Reaction rates analysis

The reaction rates analysis will cover both heterogeneous and homogeneous reactions, The discussion will be based on temperature, velocity, and turbulence of the gas in the domain.

6.2.3.1 Full and partial combustions

The first set of reactions to be analyzed is the full and partial combustion. Figure 6.15 below illustrates the calculated rates from the tip of the tuyere to one meter inside the domain (white dashed line Figure 5.7).

Figure 6.15 – Reaction rates for Full and Partial combustion

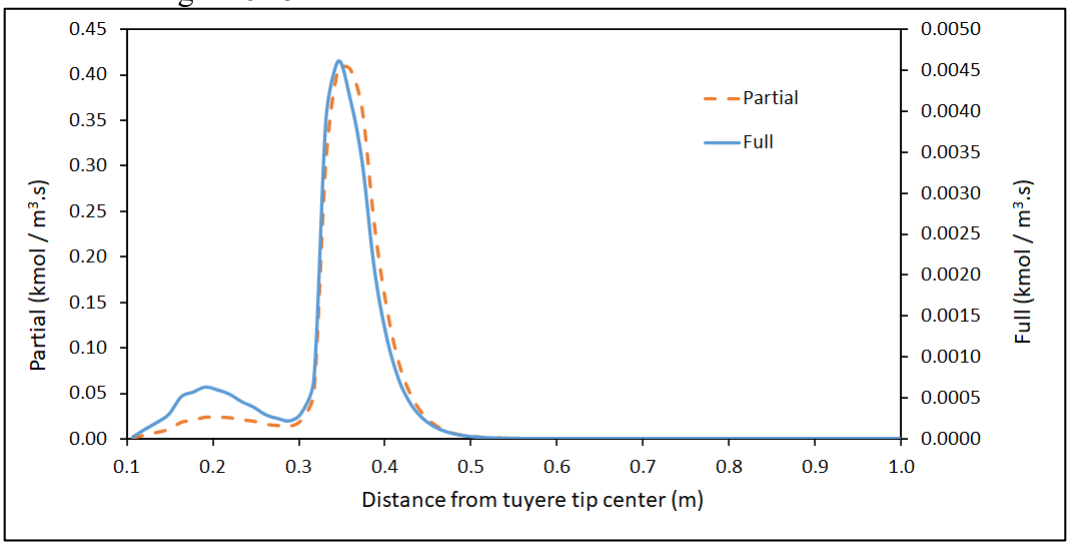

Source: author.

The results were plot in the primary and secondary *y*-axis, to illustrate that both reactions occur at the same location, where the partial combustion is plotted in the former (left side) and full combustion at the latter. Observing the values, we can notice that the blue curve, partial combustion, has a much higher rate than the orange dashed curve, full combustion. This behavior is attributed to the average temperature of the gas and coke, which have a value of approximately 1600 K at 0.3 m position (Figure 6.12). Observing the Arthur constant plot (Figure 4.2), the limit where the partial combustion assumes protagonism in the ratio is around 800 K, a value far less than the one presented in the graph. In consequence of that, the partial combustion reaches a high value where there is sufficient oxygen, being the main source of its consumption at the board of the raceway, where there is carbon, generating energy and CO to the system. Figure 6.16 and Figure 6.17 illustrate the location of the reactions, at the raceway cavity border through the contours maps (Figure 5.6).

Figure 6.16 – Reaction rate – Full combustion (unit: kmol/m^3.s)

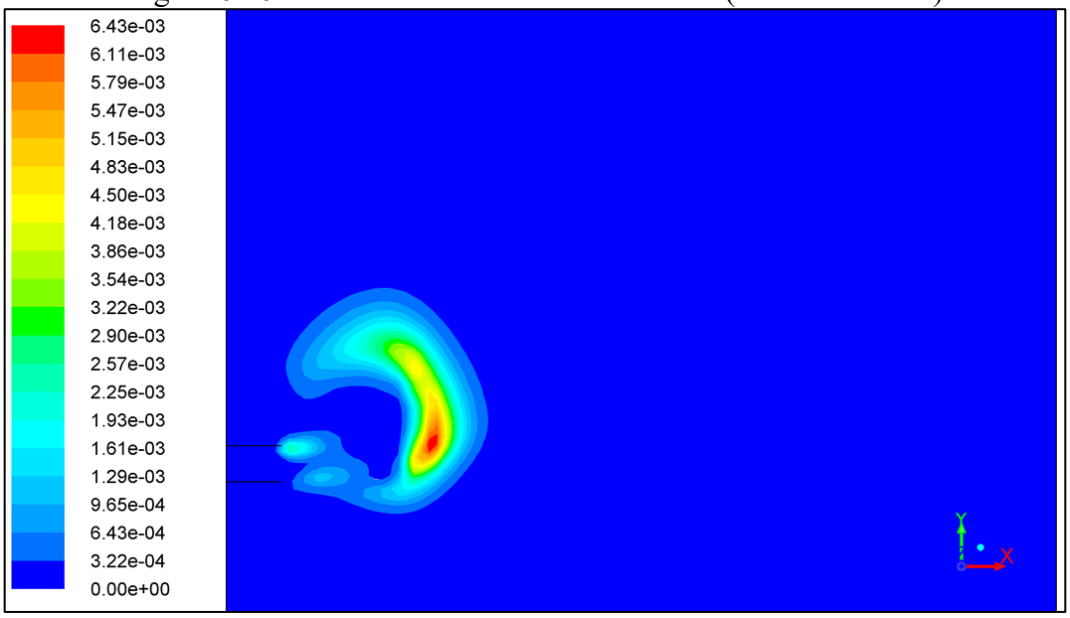

Source: author.

Figure 6.17 – Reaction rate – Partial combustion (unit: kmol/m^3.s)

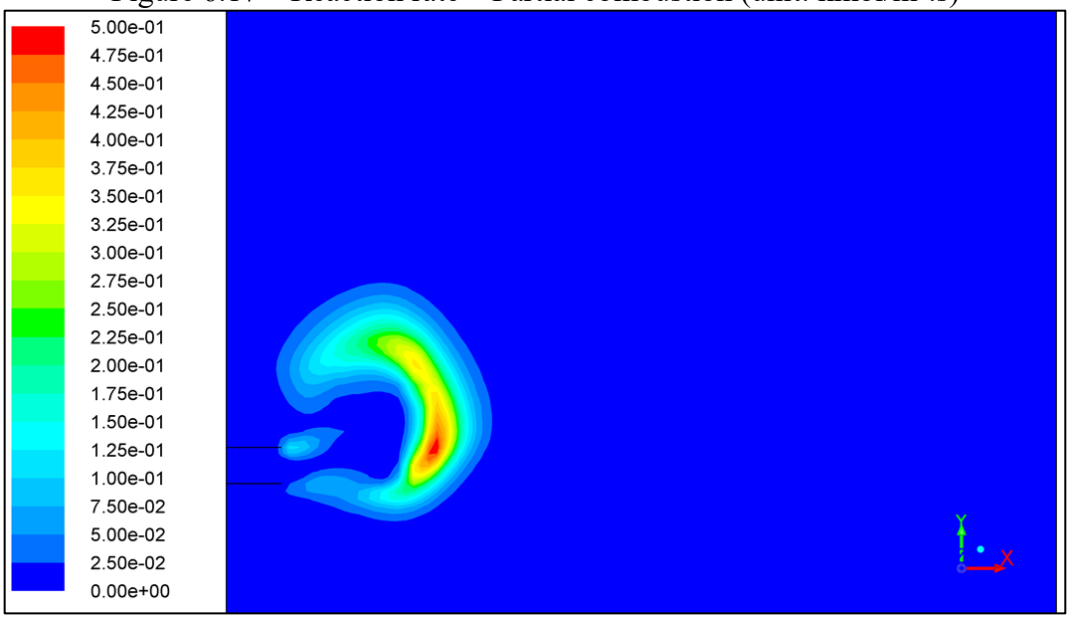

Source: author.

6.2.3.2 Solution loss and water gas

Next, Figure 6.18 below shows the curves relative to the solution loss and water-gas reactions.

Figure 6.18 – Reaction rates for Solution loss and Water gas

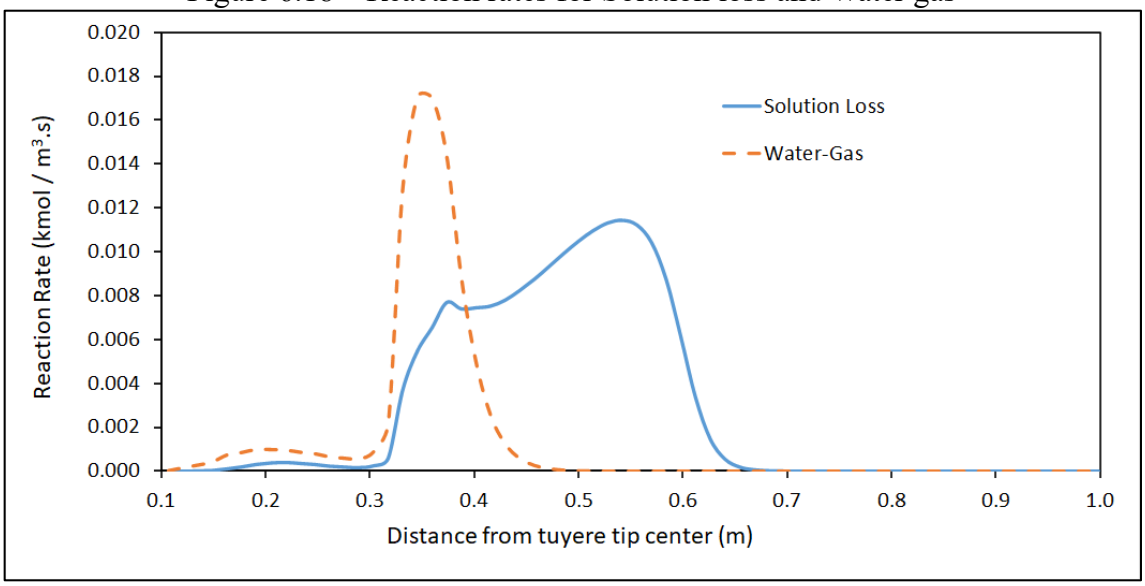

Source: author.

The location where the water-gas reaction reaches its peak (orange dash curve) is similar to full and partial combustions, indicating that this reaction acts mainly at the borders of the raceway. However, differently from the previous ones, this reaction uses H_2O as an oxidant agent, which was considered to be introduced by the blast at a concentration of 0.01

molar fraction. One can infer from the curve position peak that all the H_2O is consumed when it touches the raceway border (supported too by Figure 6.9), where the rate becomes the highest. Figure 6.19 below illustrates the location where the reaction occurs.

Figure 6.19 – Reaction rate – Water Gas (unit: kmol/m^3.s)

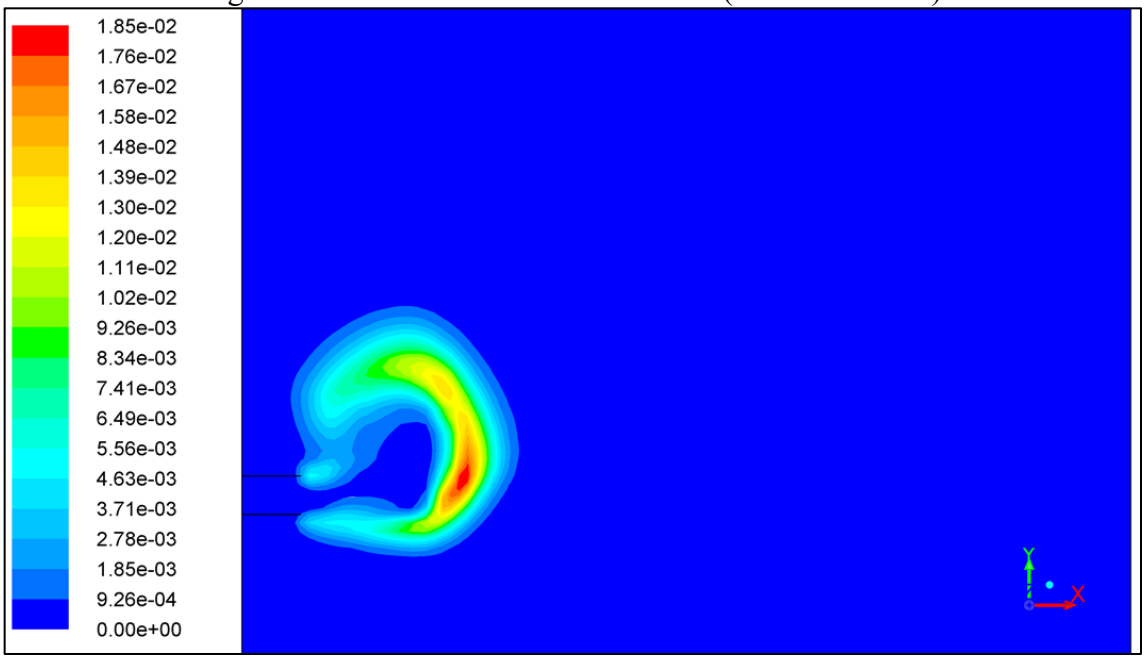

Source: author.

Unlike the previous reactions, the blue curve which represents the solution loss reaction is indicating that this reaction acts in different locations, more precisely in two locations, at the borders and after the raceway cavity. Figure 6.20 below illustrates the region on the domain where the reaction occurs.

Figure 6.20 – Reaction rate – Solution Loss (unit: kmol/m^3.s)

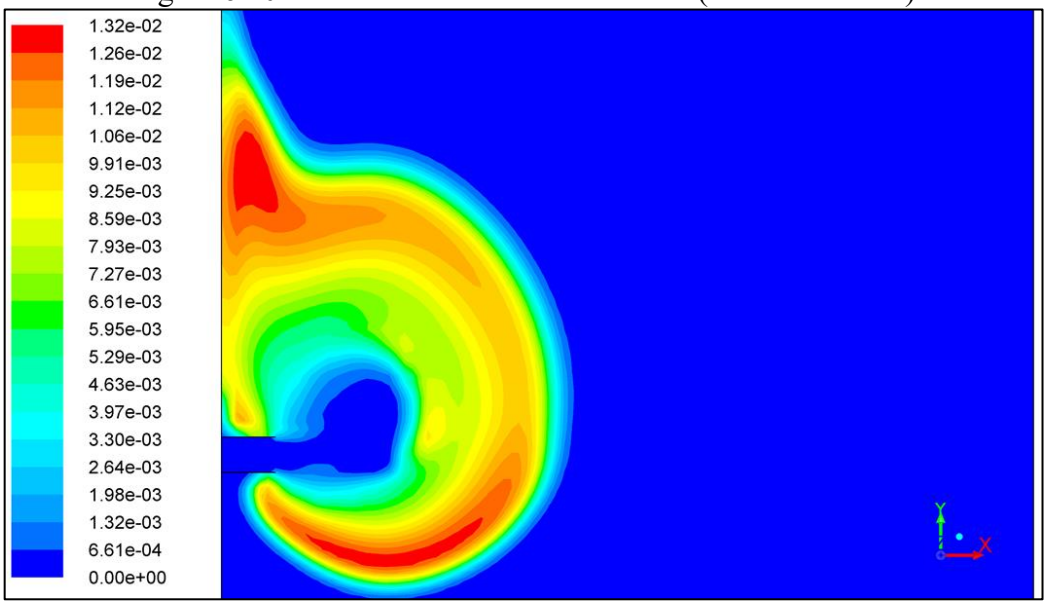

Source: author.

As one can see, the reaction is also occurring slightly further from the raceway borderline, when compared to the previous ones.

The solution loss oxidant agent is the CO_2, which is mostly provided from the CO combustion, a homogeneous reaction, and in a lower quantity by the full combustion, once this reaction does not have a higher rate due to the high temperature. Therefore, the solution loss uses the CO_2 from other reactions, converting it into CO, and in a larger proportion due to the stoichiometry of the reaction (ratio of 1:2 molecules). From Figure 6.7, one can see that the CO_2 mole fraction is limited almost precisely by the region in which the solution loss rate reaction is acting, and after this region, the CO mole fraction increases its value, which infers that CO_2 is being consumed by the solution loss.

6.2.3.3 Homogeneous reactions

For the homogeneous reactions, Figure 6.21 below plots the reaction rates through the centerline from the tuyere tip.

Figure 6.21 – Reaction rates for CO and H_2 combustion

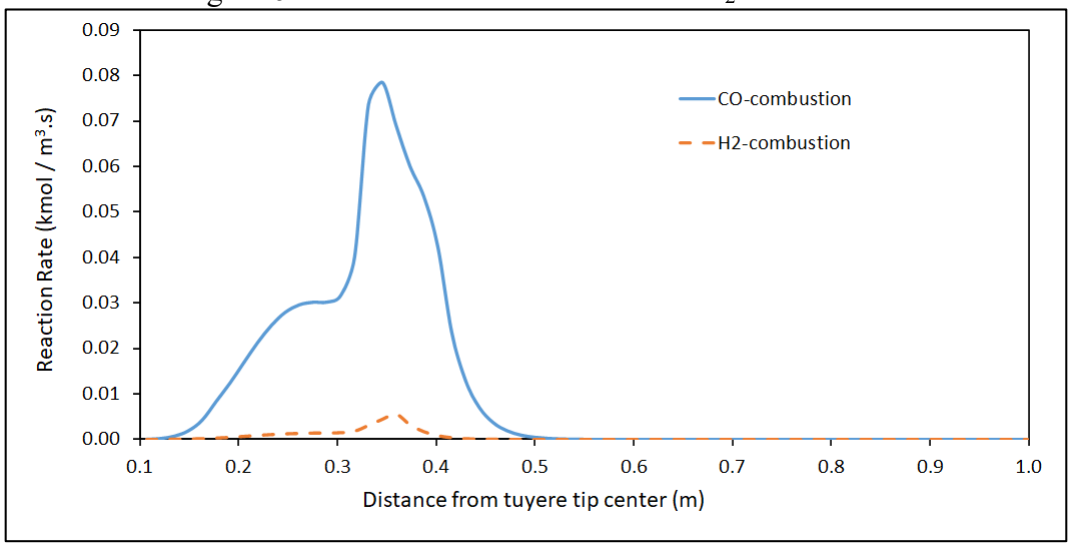

Source: author.

The homogeneous reactions followed the Eddy-dissipation model, which assumes that the rate of combustion is determined by the rate of intermixing on a molecular scale of fuel and oxygen eddies, or small vortex. In other words, by the rate of dissipation of the eddies.

Then, the mixing time scale k/ε, as mentioned in section § 4.8.1, can be analyzed to identify if the reactions are occurring inside the raceway cavity. Figure 6.22 below plots the turbulence time scale ratio at the tuyere central axis.

Figure 6.22 – Turbulence time scale, k/ε

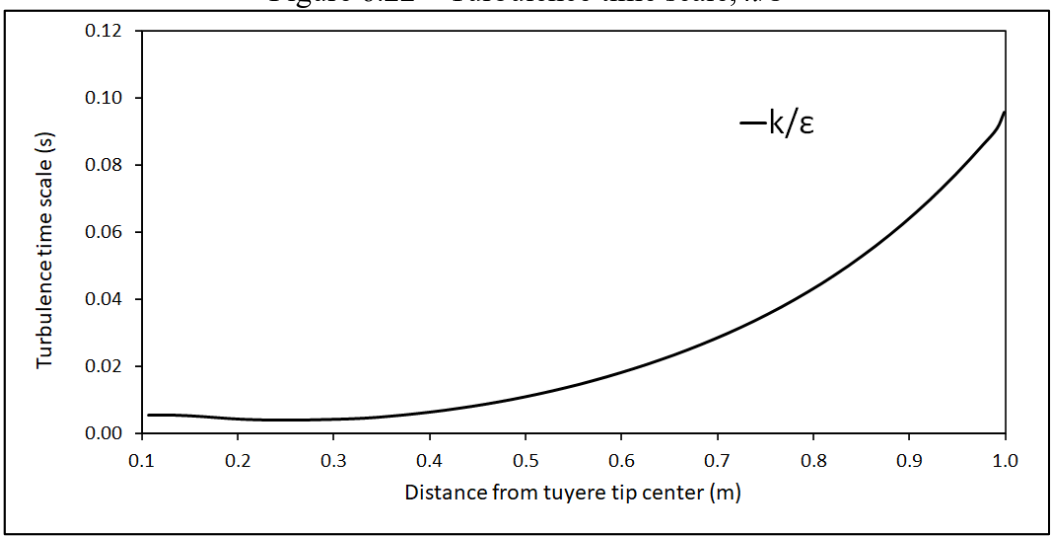

Source: author.

As one can see, the position of the curve which characterizes the raceway cavity (below 0.4 m) presents very low time scale values, inferring that the reactions are occurring very fast due to the mixing proportioned by the velocity of the gas. The inverse of this ratio will originate a high value for the rate of the reaction (Equation (66) and (67)) when the concentration of the species involved are also in high value, which is the case for CO gas species produced by the partial combustion. For the H_2 combustion, as the concentration of this species is too low, the rate does not achieve high values.

To illustrate this phenomenon, the turbulent quantities kinetic energy (k) and dissipation rate (ε), are displayed in Figure 6.23 and Figure 6.24 in their respective contour maps, as well as and the region where the homogeneous reactions are occurring in Figure 6.25 and Figure 6.26.

Figure 6.23 – Gas turbulent dissipation rate ε (unit: m^2/s^3)

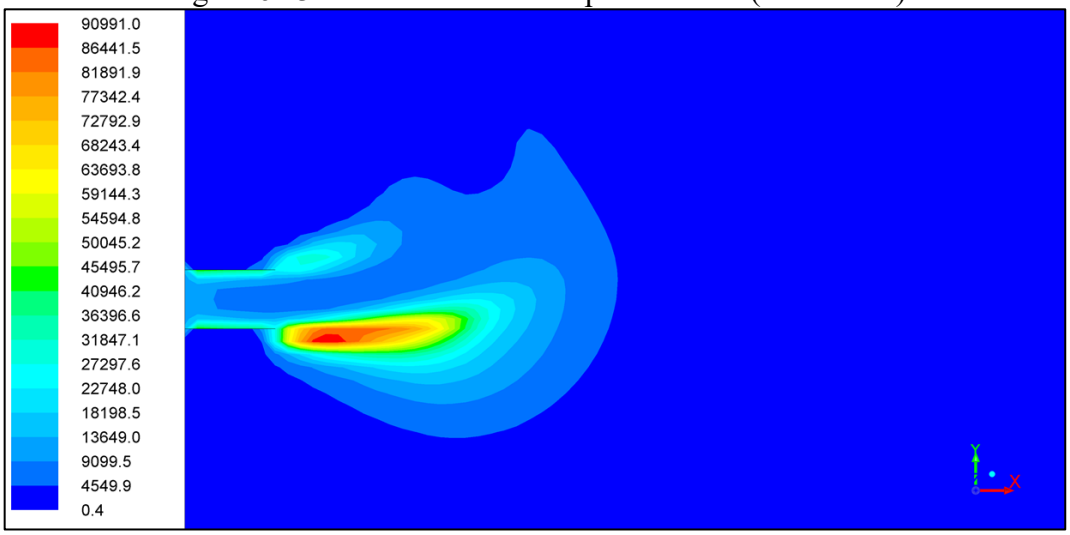

Source: author.

Figure 6.24 – Gas turbulent kinetic energy k (unit: m^2/s^2)

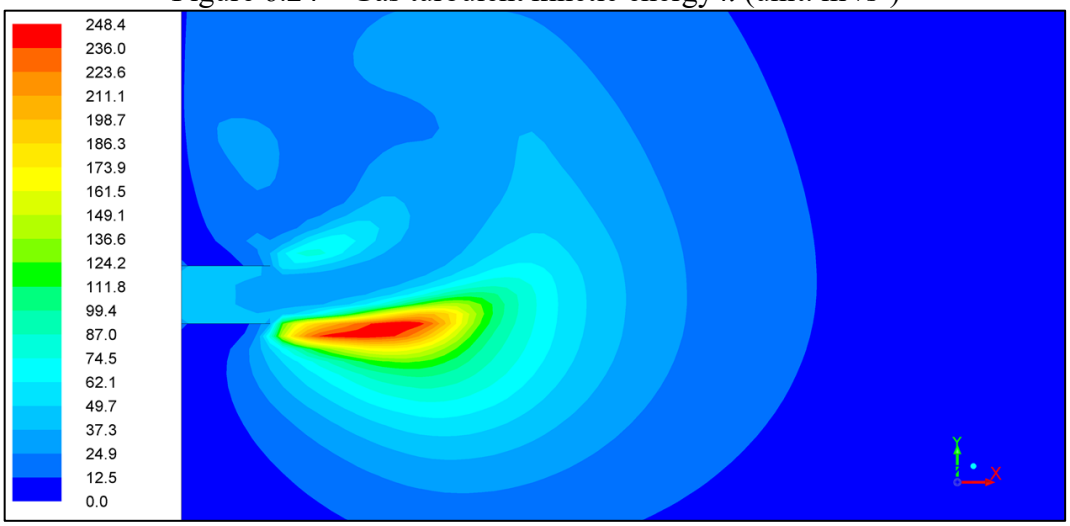

Source: author.

Figure 6.25 – Reaction rate – CO combustion (unit: $kmol/m^3.s$)

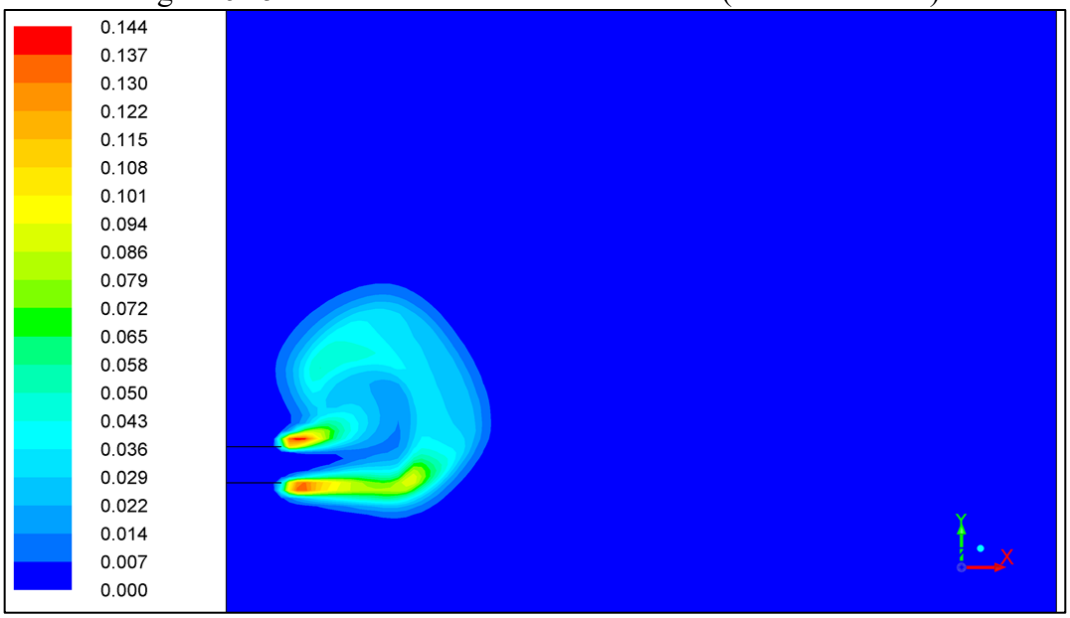

Source: author.

Figure 6.26 – Reaction rate – H_2 combustion (unit: kmol/m^3.s)

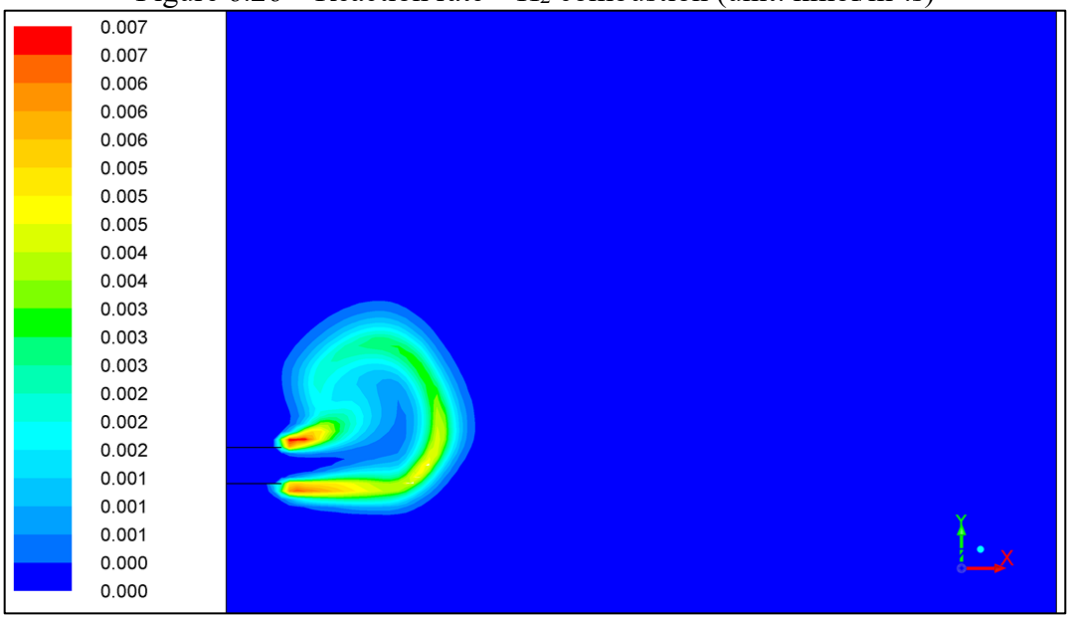

Source: author.

Observing the contours, the region nearby the tuyere walls concentrates the highest value of turbulence, which reflects in high reaction rates.

Now, to observe the cause of the turbulence, the gas velocity vector profile is illustrated in Figure 6.27 below.

Figure 6.27 – Gas velocity vectors (unit: m/s)

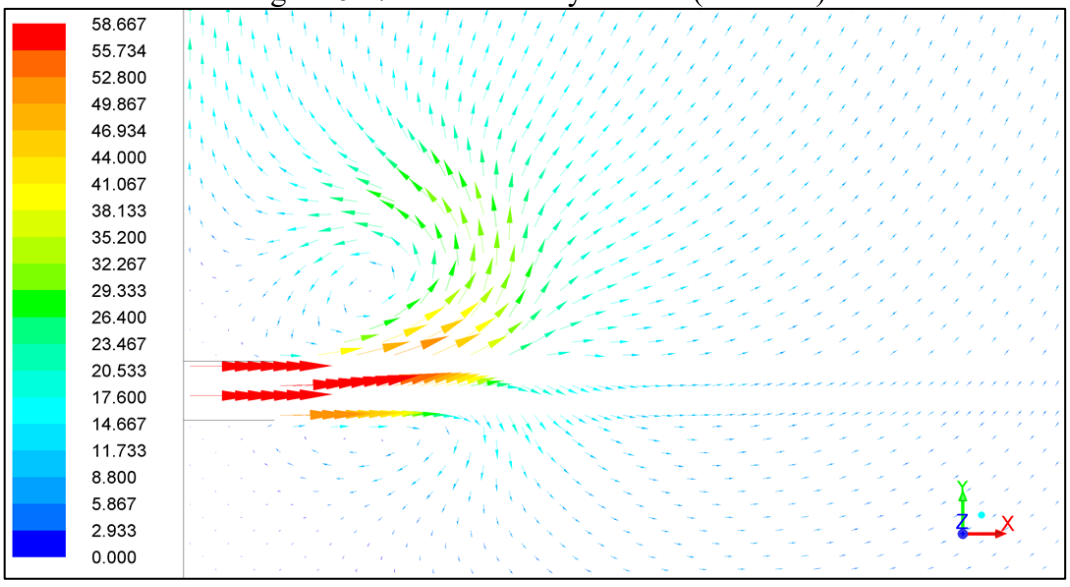

Source: author.

As one can see, there are high-value velocity vectors on the inferior and superior walls of the tuyere, which is causing turbulence generation in these regions. To observe the consequence of reaction regions on the final gas temperature, Figure 6.28 below illustrates the gas temperature profile contour map.

Figure 6.28 – Gas Temperature (unit: K)

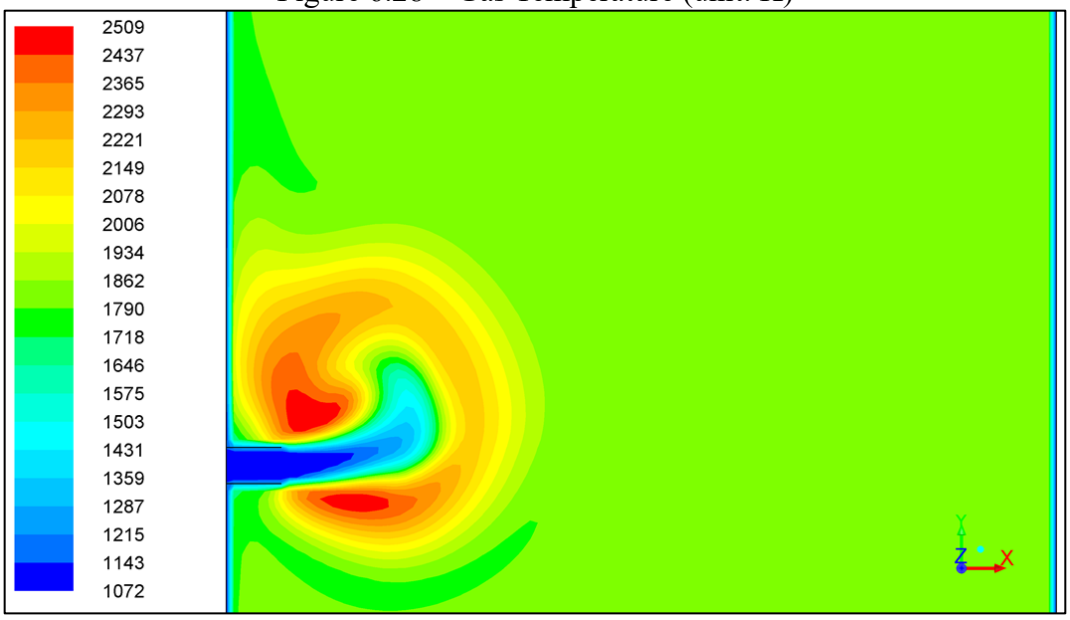

Source: author.

From the figure, one can observe that in the regions where there is a high temperature, are the regions where there is high turbulence, below and above the tuyere walls.

6.2.3.4 Reaction rates analysis summary

After the results confrontation of each reaction rate in pairs, one can observe all the values on one plot in Figure 6.29 below.

Figure 6.29 – Overlay of all reaction rates

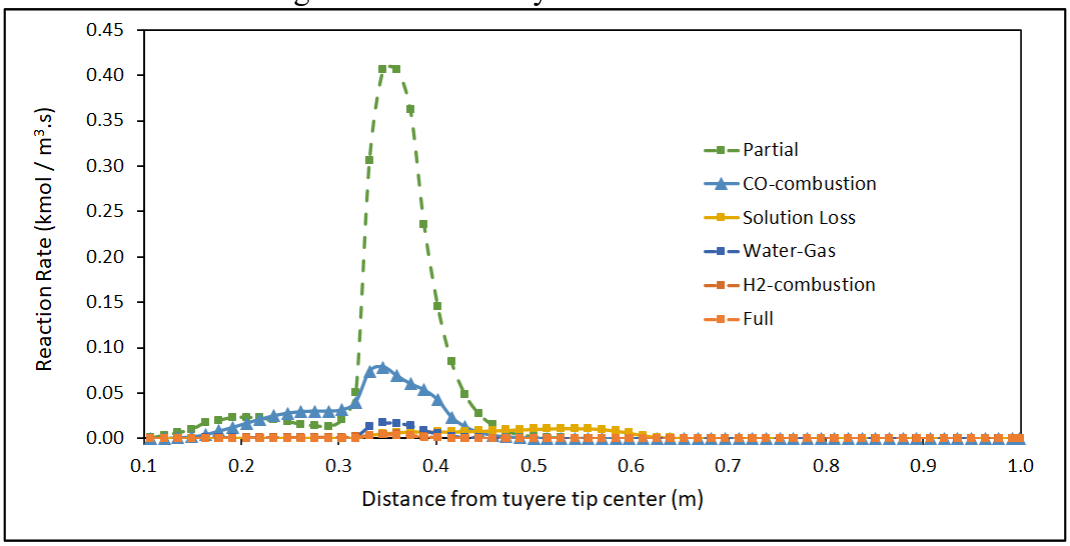

Source: author.

The plot indicates that the partial combustion reaction has the highest reaction rate among all the others reactions, followed by the CO-combustion homogeneous reaction.

The high rate reaction for the partial combustion is due mainly to the average temperature of the coke and gas phases and the Arthur constant acting as a “switch”, controlling the rates. For the CO-combustion, the behavior can be attributed to the turbulence field nearby the tuyere wall and by the carbon monoxide concentration.

The solution loss is also an important reaction to the system, but its rate is too low due to its dependence on the CO_2 concentration, which is generated by the previous reactions.

The water-gas and H_2 reactions also depend on species concentration that does not achieve high values in the experiment simulated, thus presenting low reaction rates.

Overall, the present model was capable of reproducing similar results as from the work of NOGAMI et al., 2004.

6.3 Coal combustion

The validation is going to be present first in terms of O_2 and CO_2 detected in an experiment done by Zhang, as described in section § 5.3. Next, an analysis of the results will be presented containing temperature field, flow field, chemical species, variables from tracked particles as residence time, properties, volatiles, and char mass fractions.

6.3.1 Validation

The experimental work from (ZHANG et al., 2005) was used to validate the coal combustion model using the implemented reaction rate formulation. Illustrated from Figure 6.30 to Figure 6.35, the validation is presented in plots and contour maps of species molar fractions for O_2 and CO_2 and their confrontation with Zhang's experimental measurements.

Figure 6.30 – O_2 and CO_2 molar fractions for coal 1

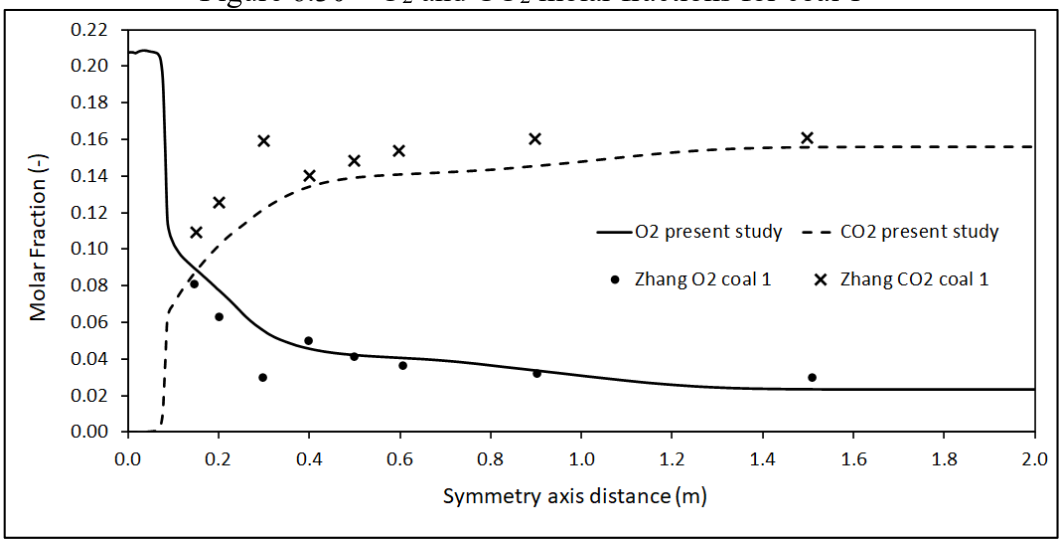

Source: author.

Figure 6.31 – Coal 1 O_2 molar fraction contour, a) all domain, b) 0.5 m zoom

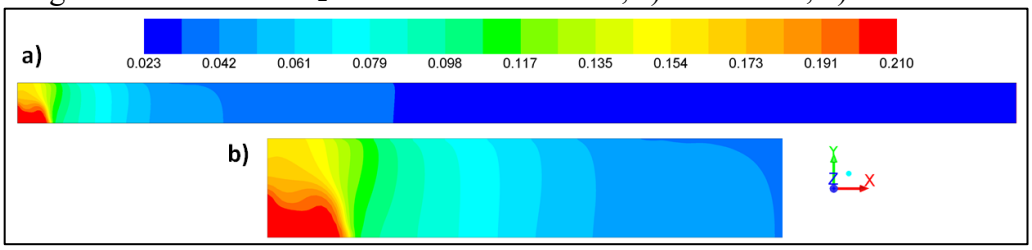

Source: author.

Figure 6.32 – Coal 1 CO_2 molar fraction contour, a) all domain, b) 0.5 m zoom

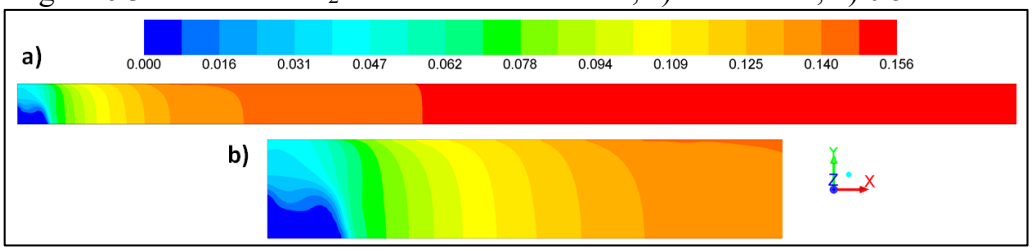

Source: author.

Figure 6.33 – O_2 and CO_2 molar fractions for coal 2

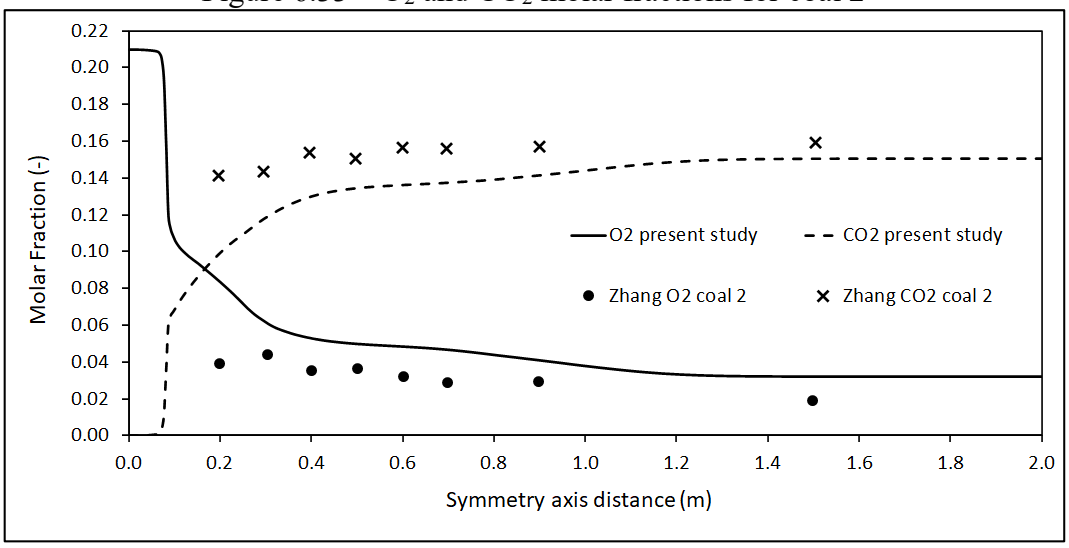

Source: author.

Figure 6.34 – Coal 2 O_2 molar fraction contour, a) all domain, b) 0.5 m zoom

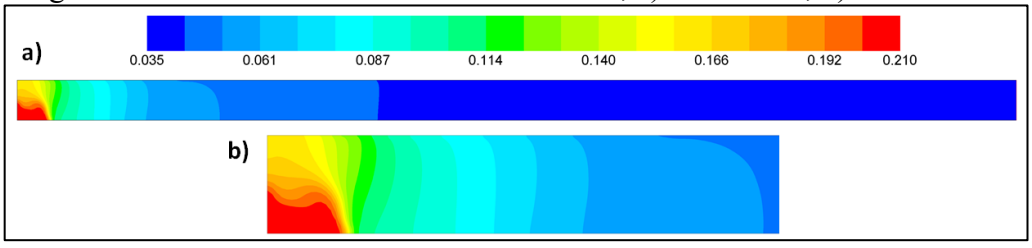

Source: author.

Figure 6.35 – Coal 2 CO_2 molar fraction contour, a) all domain, b) 0.5 m zoom

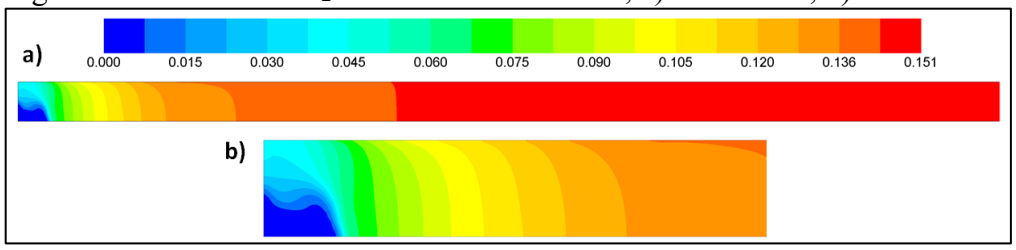

Source: author.

As one can see, the mole fractions of O_2 and CO_2 fitted better in coal 1 than in coal 2. This is linked to the coal analysis, more specifically, to the fixed carbon value. Coal 1 has a higher value of fixed carbon than coal 2 (Table 12), which will be used in the char combustion after the devolatilization. Therefore, the model tendency was to give better values to coal 1, which is reflected in the combustion species production and consumption.

One way to overcome this issue would be to have more information about the coal properties, for example, the swelling coefficient, which represents the capacity of the coal to increase its diameter after the devolatilization (YU et al., 2005), in which on the present study was considered as one to give a base result for the method being validated. Another way would be to test different devolatilization models, as the two-competitive model from Kobayashi (KOBAYASHI et al., 1977), to investigate if the yield of the CO_2 would increase.

Lastly, the particle diameter distribution could be interfering with the overall reactions. ALGANASH, 2015 proposed to investigate the coal combustion using the same experimental work being used in the present study but made use of a Rosin-Rammler particle diameter distribution to model the mass fraction attributed to each size. Such consideration could be interfering with the overall O_2 and CO_2 molar fractions calculated by the model, as to distribute more mass fraction to a particle with more surface area (lower diameters).

Thereby, it is clear that coal 1 achieved better results in terms of the chemical species than coal 2, therefore, the former will be used to report the reaction rates analysis in the next sections.

6.3.2 Mesh independence study

The mesh independence study was made to investigate if the results would change with different grid refinements. The control volume elements, grid generation, and strategy followed the one already described for the raceway combustion (section § 6.2.2).

However, one difference was the use of two different grid densities, one at the position x = 0.5 m in the symmetry plane, and another at the wall after the secondary gas inlet

at the position $y = 0.02$ m. These two grid densities were applied to increase the refinement at the region where most of the coal combustion takes place, and coarse the mesh where there are fewer gradients. Next, Figure 6.36 to Figure 6.38 illustrate the main parameters for the 48000 control volumes grid.

Figure 6.36 – Inlet coal detail for the 48000 control volume grid

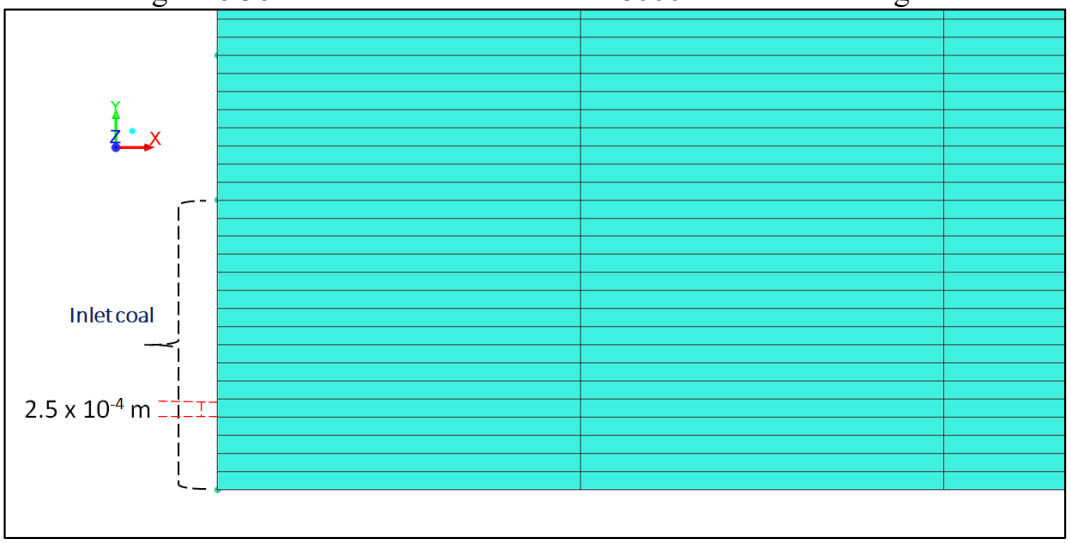

Source: author.

Figure 6.37 – Grid density at the wall, $y = 0.2$ m, for the 48000 control volume grid

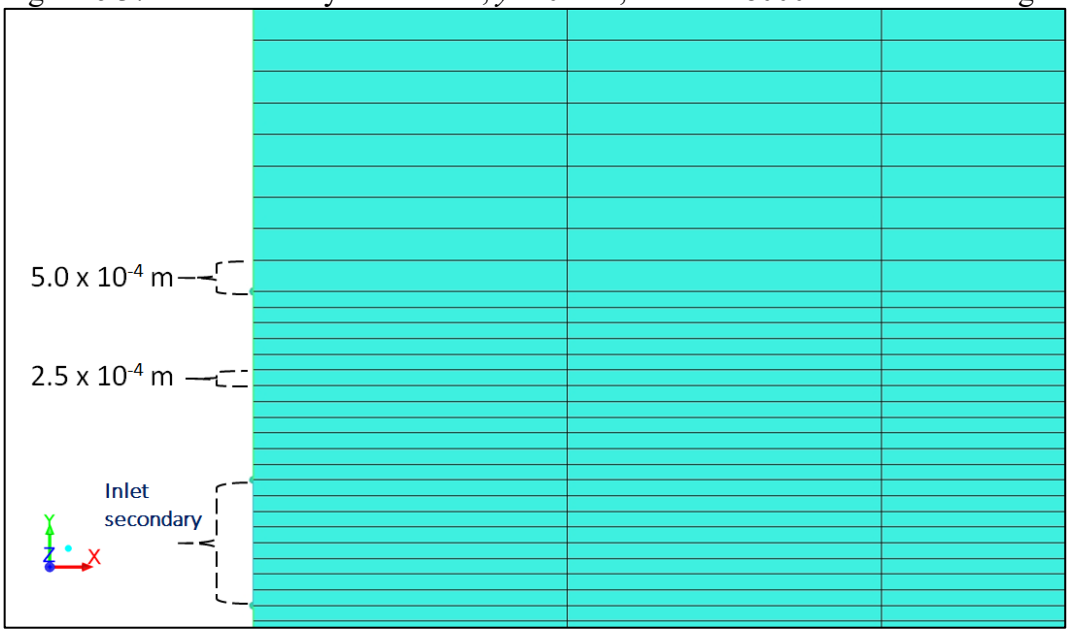

Source: author.

Figure 6.38 – Grid density at the symmetry plane, x = 0.5 m, for the 48000 control volume grid

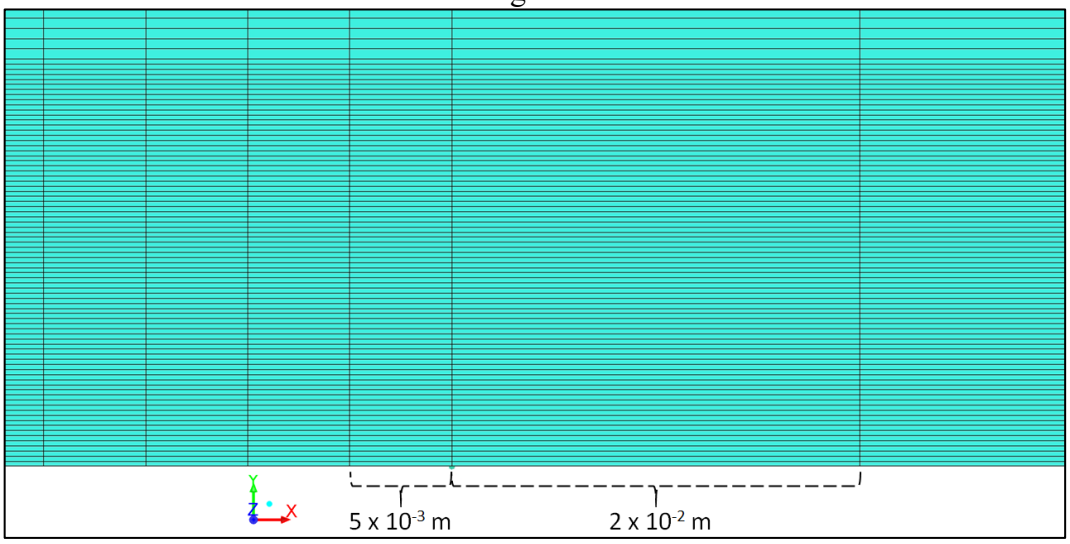

Source: author.

The refinement strategy followed the one from the raceway combustion, a progressing refinement until the results showed a low variance and were in agreement with the data used for the validations. Table 17 below describes the parameters varied in each mesh simulated.

Table 17 – Coal combustion mesh independence study parameters

Mesh name	Total Quadrilateral. Elements	Elements: inlet coal	Elements: inlet primary	Elements: inlet secondary	Elements: axis
113k	112500	20	15	10	375
73k	72000	16	12	8	300
48k	48000	16	12	8	200
46k	45200	14	10	6	200
40k	40500	12	9	6	225

Source: author.

As one can see from the table, the number of elements in each inlet varied according to the refinement, as well as the elements at the central axis. The grids 40k and 46k performed worse, once they were the coarse ones. As the refinement proceeded, the grids 48k and 73k achieved better results with no change in the results from one mesh to the other. Lastly, a global refinement resulting in a mesh with 112500 elements (113k mesh) to confirm the results no variance with the mesh. Figure 6.39, Figure 6.40, and Figure 6.41 below plot the results relative

to the coal 1 evaluated for each mesh size simulated: gas temperature, CO_2, and O_2 chemical species.

Figure 6.39 – Coal combustion grid study: gas temperature variation

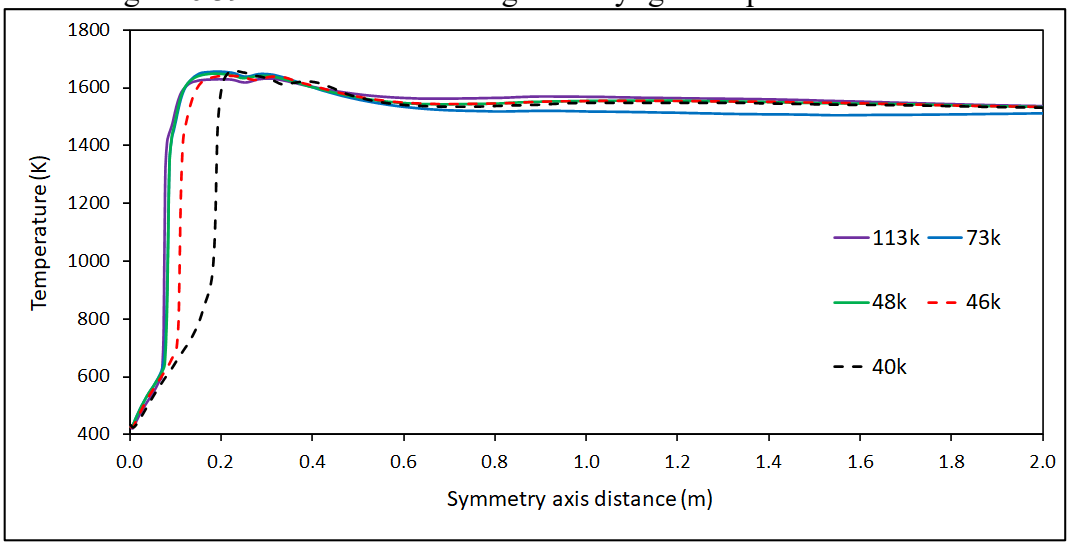

Source: author.

Figure 6.40 – Coal combustion grid study: O_2 variation

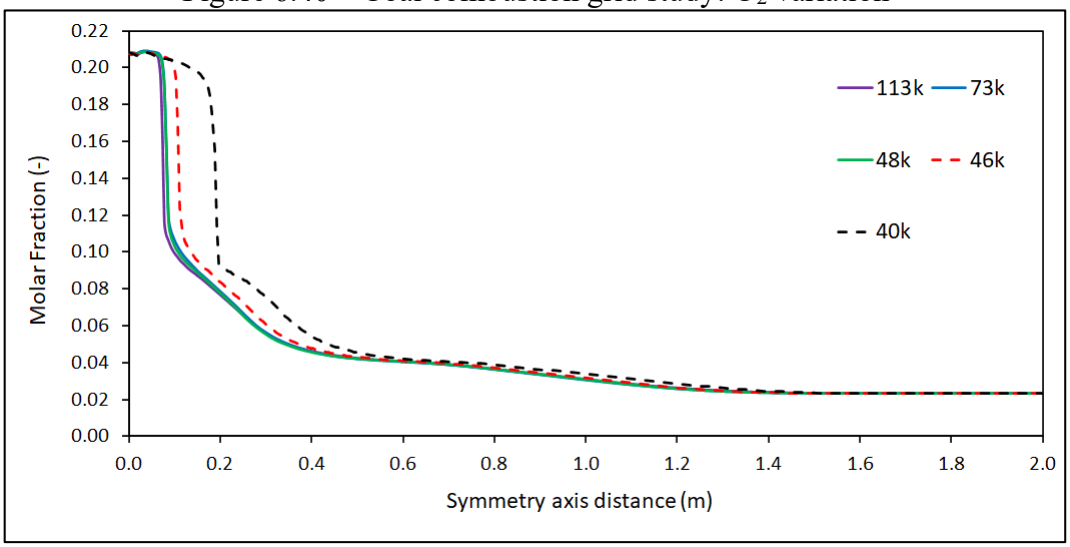

Source: author.

Figure 6.41 – Coal combustion grid study: CO_2 variation

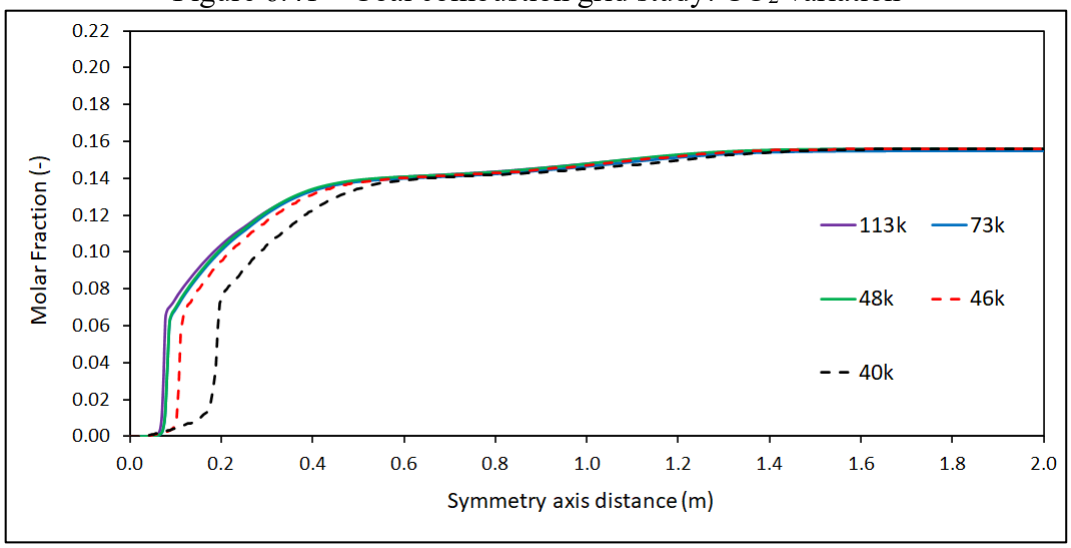

Source: author.

From the figures, one can see that the grids 113k, 73k, and 48k achieved the same results. The grid chosen to report the results were the 48k, as no significant difference was found in the results confrontation with the other fine grids, and the simulation time would be reduced.

The residuals were capable to reach values in an order of 10^{-4}. Figure 6.42 illustrates the residuals after1000 iterations for the 48k grid.

Figure 6.42 – Residuals plot – 48k grid

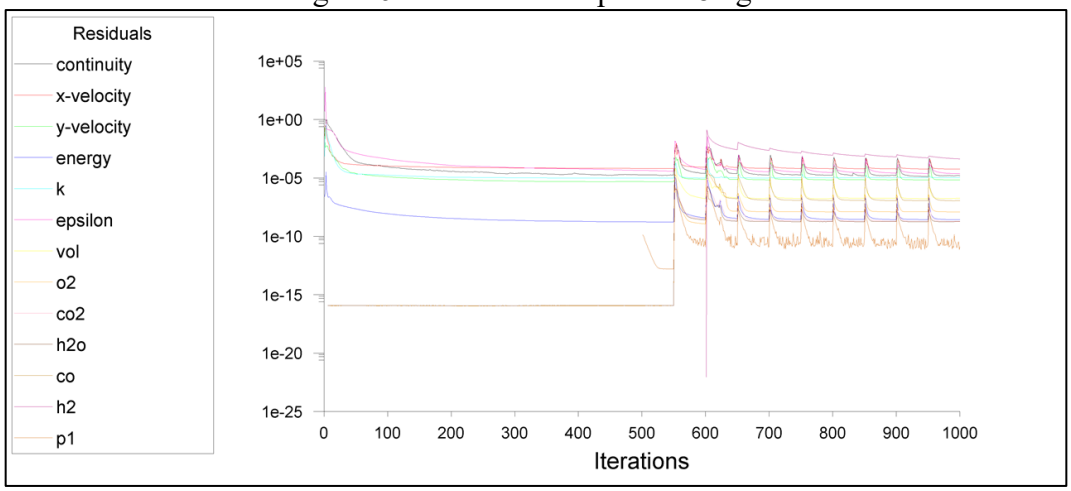

Source: author.

6.3.3 Reaction rates analysis

The following section will cover the analysis of the reaction rates relative to coal 1 using a mesh with 48000 quadrilateral elements. Also, an analysis concerning the devolatilization and burnout rates values will be discussed. The analysis will be presented using reaction rate plots at the symmetry axis of the reactor, and contours maps.

6.3.3.1 Full and partial combustions

The first set of reactions that will be analyzed will be the full and partial combustions. To start the discussion, Figure 6.43 and Figure 6.44 show the particle temperature variation through the central axis of the reactor, and the heating rate for the 350 µm diameter particle, respectively.

Figure 6.43 – Coal particles temperature variation by size

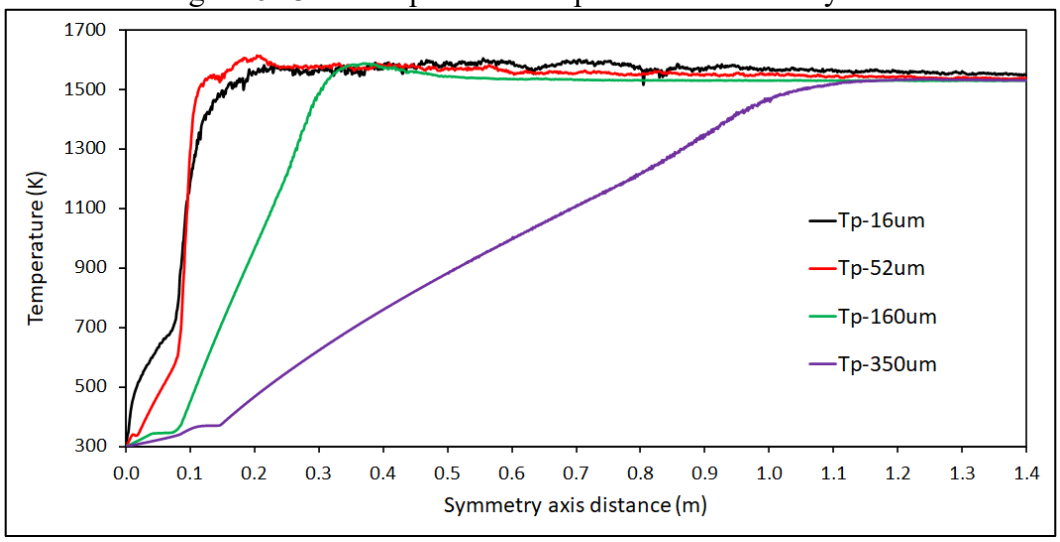

Source: author.

Figure 6.44 – Coal particle, diameter 350 µm, heating rate

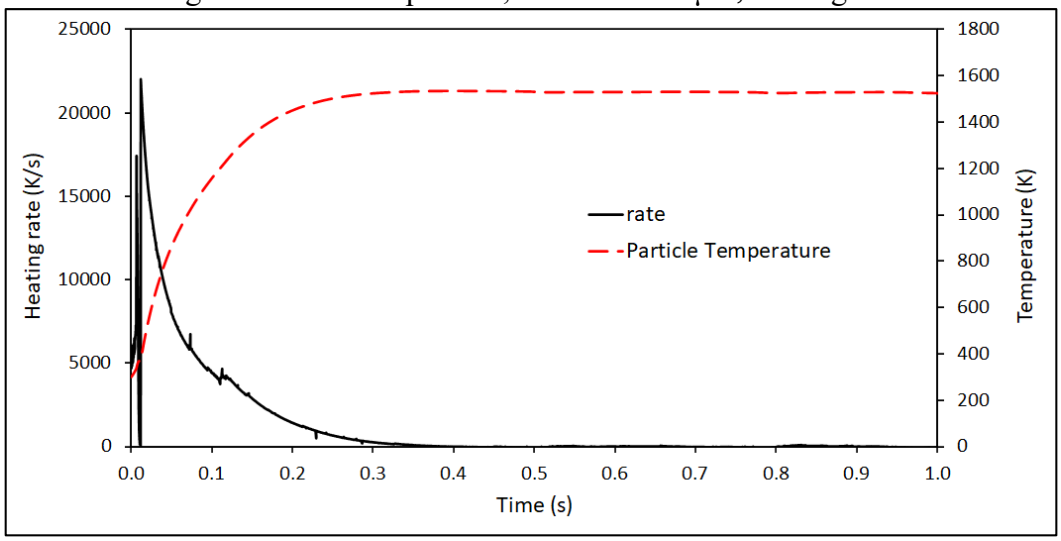

Source: author.

This first discussion about the particle temperature is necessary because of the vaporization temperature used in the model, which was set to 1200 K (Table 10). According to WU, 2005, for heating rates in an order of 10000 ºC/s, the devolatilization may start around 1500 K, and observing the heating rate in Figure 6.44, one can see that this assumption is in

agreement with the one proposed by the literature. As such, analyzing the coal particles temperature evolution in Figure 6.43, one can infer that the first set of particles that will progress to the devolatilization after the water pyrolysis at 343 K, will be the ones with 16 μm and 52 μm, at approximately 0.1 m position, followed by the particles with 160 μm, between 0.2 and 0.3 m, and finally by the 350 μm after 0.8 m. Therefore, we can expect a distinction in the location of each reaction in the domain according to the particle diameter.

With this introduction, one can proceed to the reaction rates analysis. Figure 6.45 and Figure 6.46 below plot the full and partial combustion at the symmetry axis, respectively.

Figure 6.45 – Coal full combustion reaction rate plot

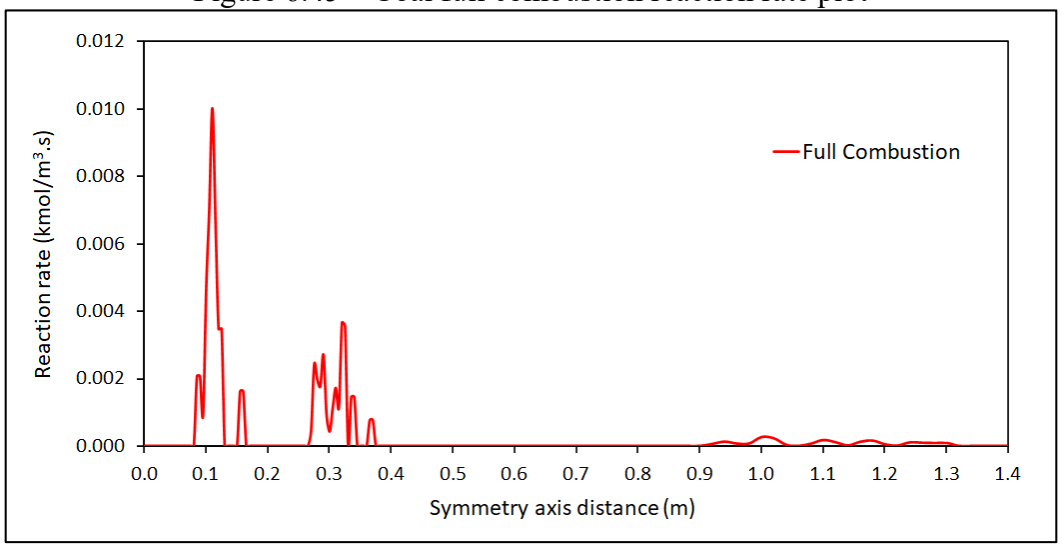

Source: author.

Figure 6.46 – Coal partial combustion reaction rate plot

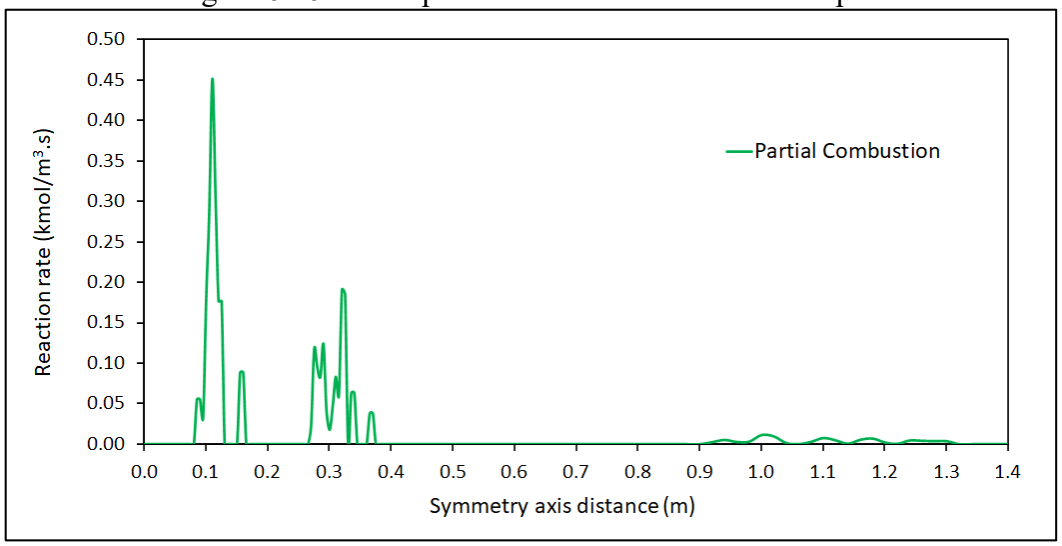

Source: author.

It can be seen in the plots that there are three distinct locations where the reactions are happening. The first peaks, between the positions 0 and 0.2 meters, are relatives to the

particles with the smaller diameters, 16 and 52 μm. Between the positions 0.2 and 0.4 meters, the 160 μm particles are reacting and, almost a trace, between the positions 1.0 and 1.4 meters, the particles with 350 μm are reacting. This is in agreement with the proposed analysis by the temperature.

The difference between the reaction rate intensity can be attributed to three main reasons: (1) to the overlap of the small particles combustion (16 and 52 μm), (2) to the O_2 species concentration, which is already almost entirely consumed at 0.4 m position, (3) and the mass fraction distribution between the diameters, which affect the larger particles with 350 μm that represent 10 percent of the mass fraction injected, and favors the small ones that together represent 65 percent. The 160 μm represents an intermediate value of 25 percent. Also, there is the superficial area of the particles that contributes to the overall reaction rate. The last justification cannot be properly addressed as it may require that each particle's mass fractions be at the same level of injection to fully answer the contribution of each superficial area by size distribution.

Another perspective of the phenomenon can be seen in Figure 6.47, and Figure 6.48 that illustrate the contours inside the domain. The values are presented in a logarithm scale to facilitate the visualization.

Figure 6.47 – Coal full combustion reaction rate, kmol/m^{3}s, log scale

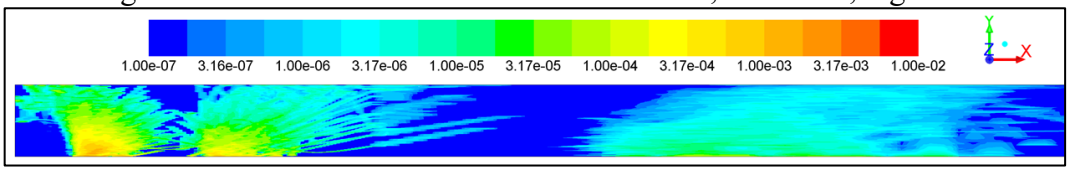

Source: author.

Figure 6.48 – Coal partial combustion reaction rate, kmol/m^{3}s, log scale

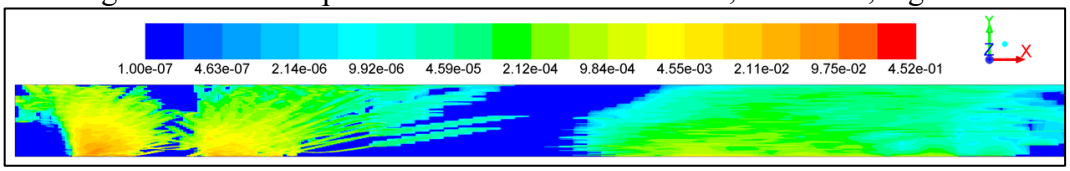

Source: author.

From the contours, one can see the three regions previously described. It is worth mention that both values at the plots and contours report the same maximum value for the reaction rates (0.01 for full and 0.452 for partial), indicating that they start at the central axis, scattering through the domain after the first ignition.

Lastly, the value of the reaction rate is higher for the partial combustion than for the full combustion, an effect that can be attributed to the Arthur constant, which favors the high temperature to give increased values of reaction rate.

6.3.3.2 Solution loss and water-gas reactions

For the next analysis, Figure 6.49 and Figure 6.50 plot the solution loss and water-gas reactions for the coal particles at the symmetry line of the reactor.

Figure 6.49 – Coal solution loss reaction rate plot

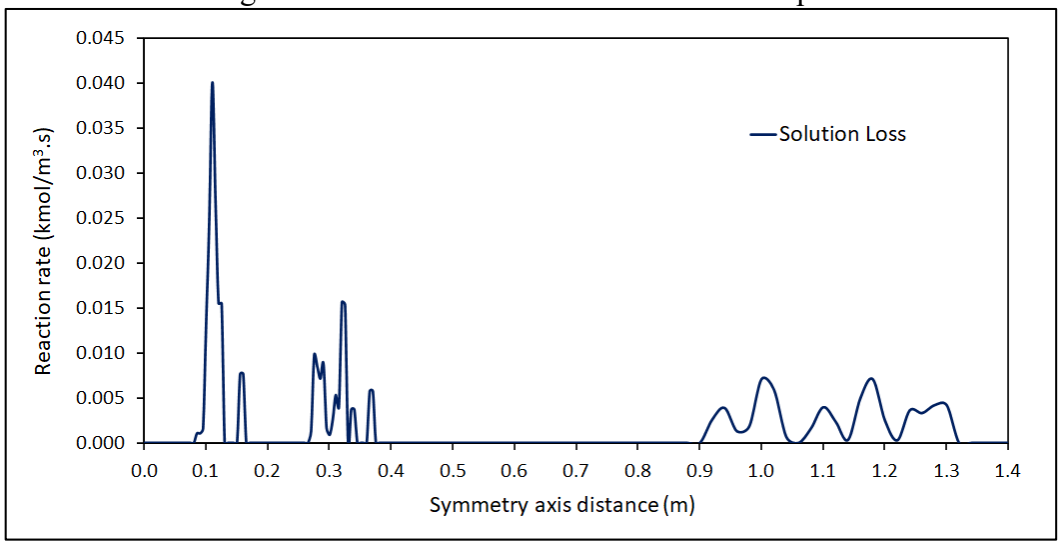

Source: author.

Figure 6.50 – Coal water gas reaction rate plot

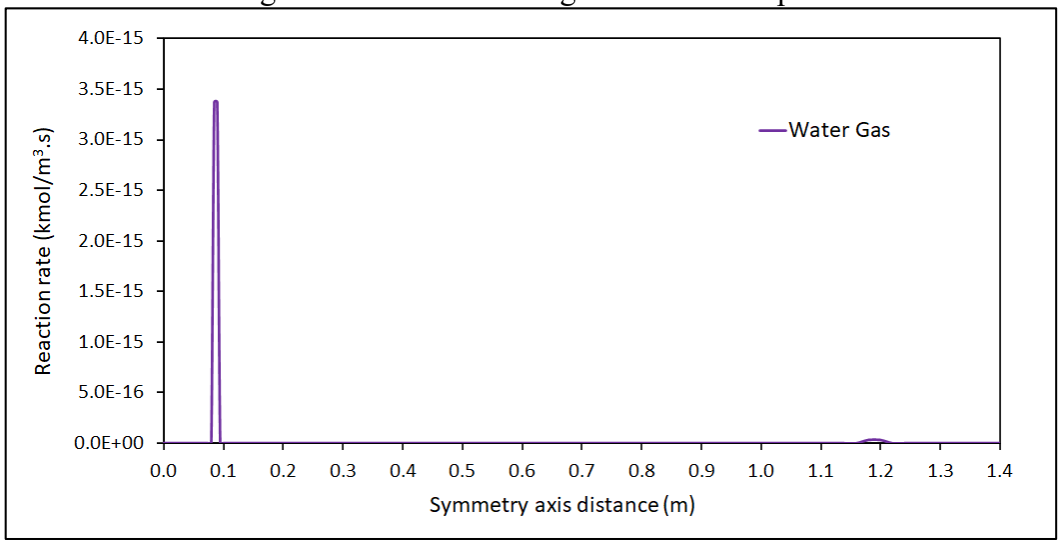

Source: author.

The solution loss plot illustrates more clearly the three spots of reactions inside the domain than the previously examined reactions. The water-gas reaction did not achieve a proper

rate, which could be attributed to the low H_2O concentration during the simulation. As for the solution loss, the high CO_2 concentration at the domain contributed to elevating the rate of the reaction for the larger diameters particle than for the ones that require the O_2 chemical species. As for the previous reactions, Figure 6.51 illustrates a contour map for the solution loss reaction at a logarithm scale. The water-gas reaction was omitted once its rate achieved a very low rate.

Figure 6.51 – Coal solution loss reaction rate, kmol/m^{3}s, log scale

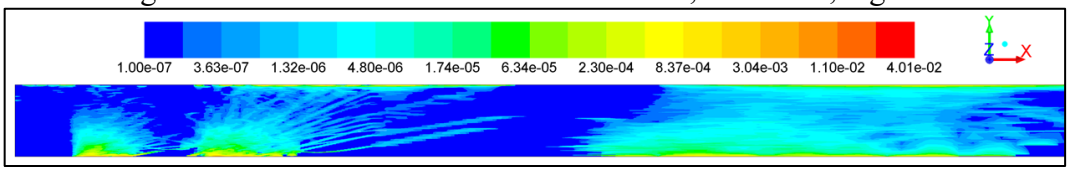

Source: author.

6.3.3.3 Homogeneous reactions

To evaluate the gas-phase homogenous reactions' influence, the CO, H_2, and volatiles combustions will be investigated. The plots of each reaction can be seen in Figure 6.52 to Figure 6.54 below.

Figure 6.52 – Gas-phase CO combustion plot

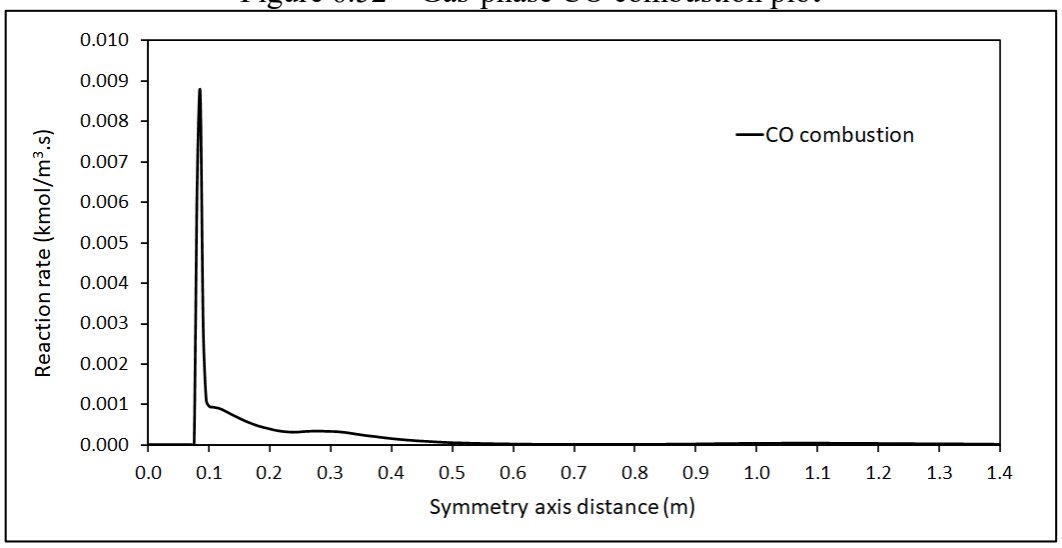

Source: author.

Figure 6.53 – Gas-phase H_2 combustion plot

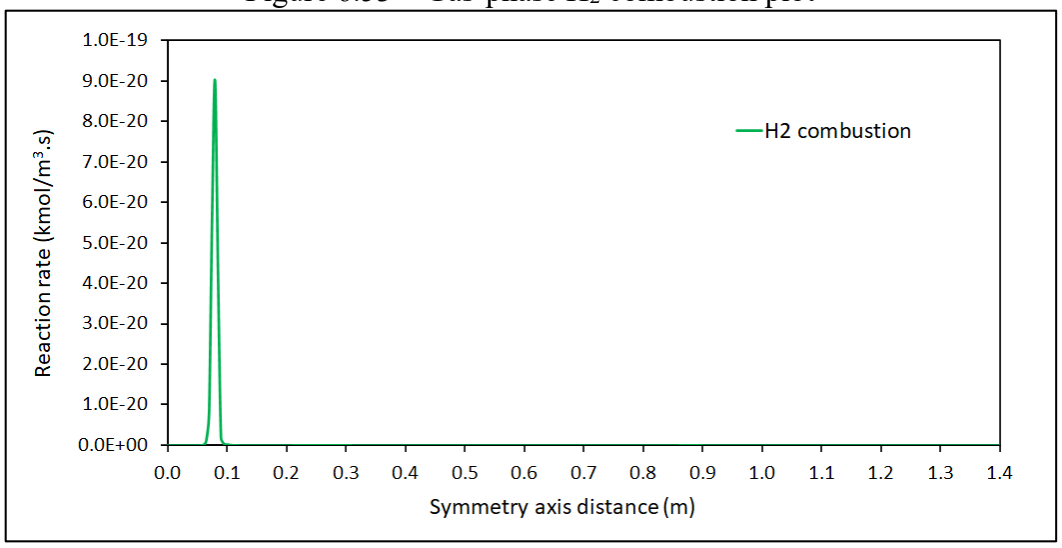

Source: author.

Figure 6.54 – Gas-phase volatiles combustion plot

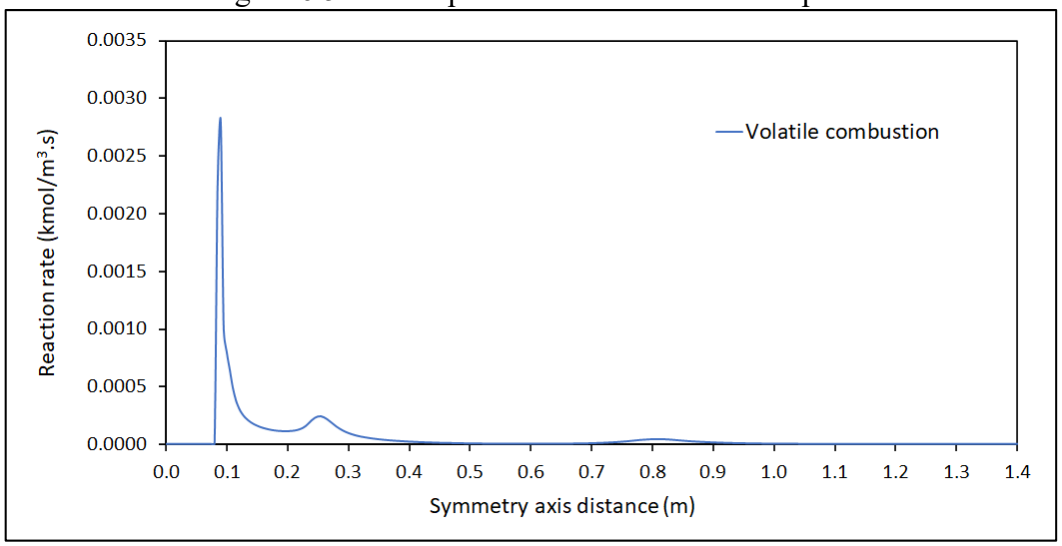

Source: author.

From the figures, we can see that only the CO and the volatiles species combustion achieved high reaction rates. Both reactions presented similar behavior, with a high peak at the lower diameters particles combustion position, an intermediate peak at the 160 μm particles, and a very low rate at the almost imperceptible at the higher diameters particles (only seen in Figure 6.54 at 0.8 m position). To better verify the phenomenon, Figure 6.55 and Figure 6.56 illustrate the domain region where the CO and the volatile species are each reacting.

Figure 6.55 – Coal CO combustion reaction rate, kmol/m^{3}s

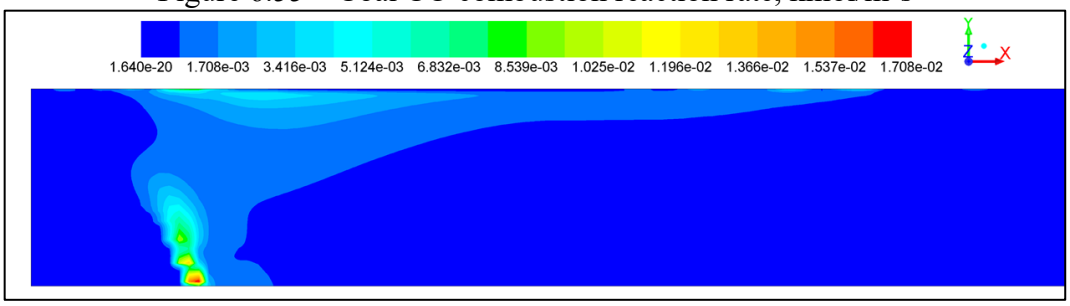

Source: author.

Figure 6.56 – Coal volatile combustion reaction rate, kmol/m^{3}s

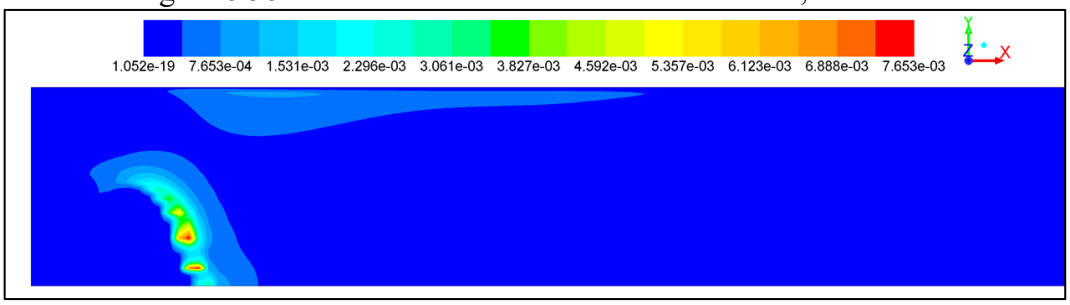

Source: author.

As we can see in the figures, the tendency of the reaction was to be concentrated at the region where there are coal particles with a smaller diameter. This can be due to the O_2 concentration is higher at that position, supporting the mixing phenomenon used by the eddy dissipation combustion model.

Another factor that affects the homogeneous reactions is the turbulence. As the experiment progress in an almost laminar environment, the mixing of the species is concentrated at the reactor entrance. To support such affirmation, Figure 6.57 plot the turbulence time scale k/ε and the homogeneous reaction rates at the symmetry axis, and Figure 6.59 and Figure 6.62 illustrates the turbulence quantities ε and k separately at the react entrance.

Figure 6.57 – Gas turbulence time scale and reaction rates at symmetry axis

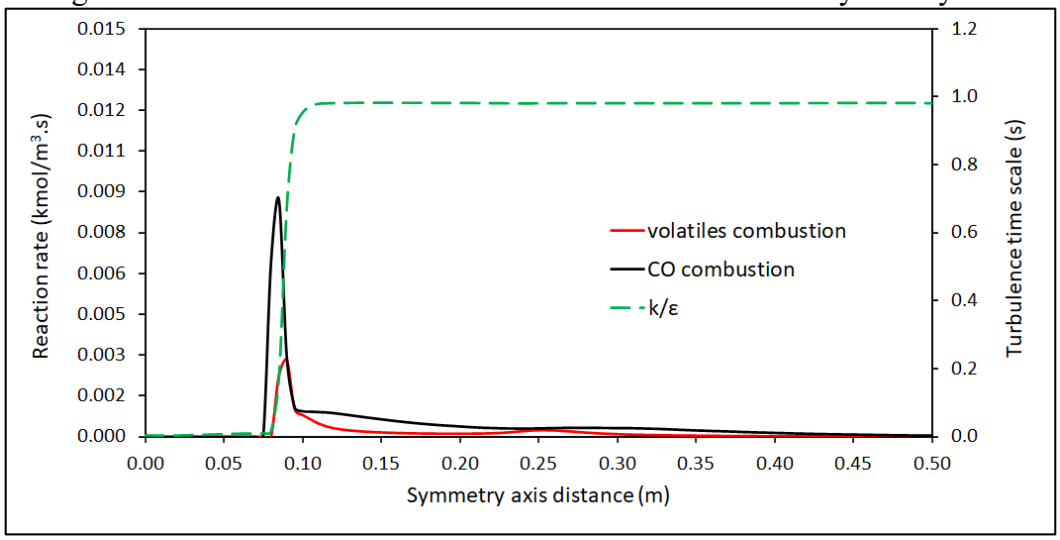

Source: author.

Figure 6.58 – Gas turbulent dissipation rate ε (unit: m^2/s^3)

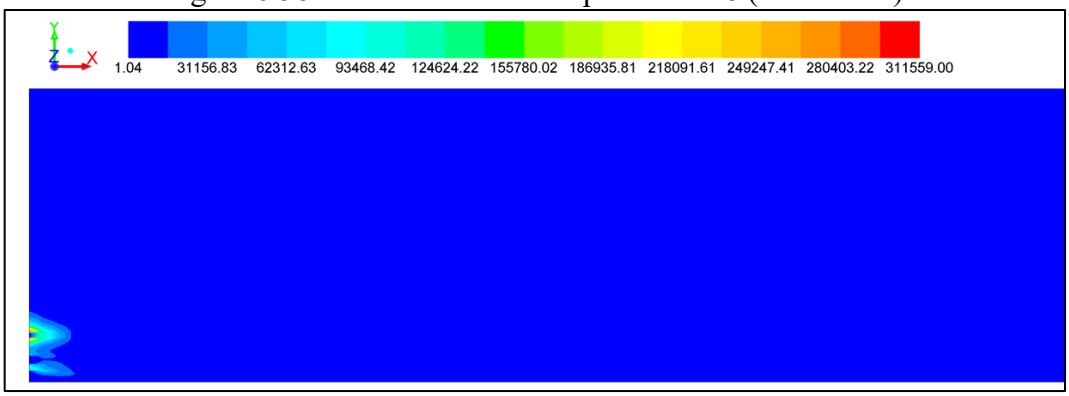

Source: author.

Figure 6.59 – Gas turbulent kinetic energy k (unit: m^2/s^2)

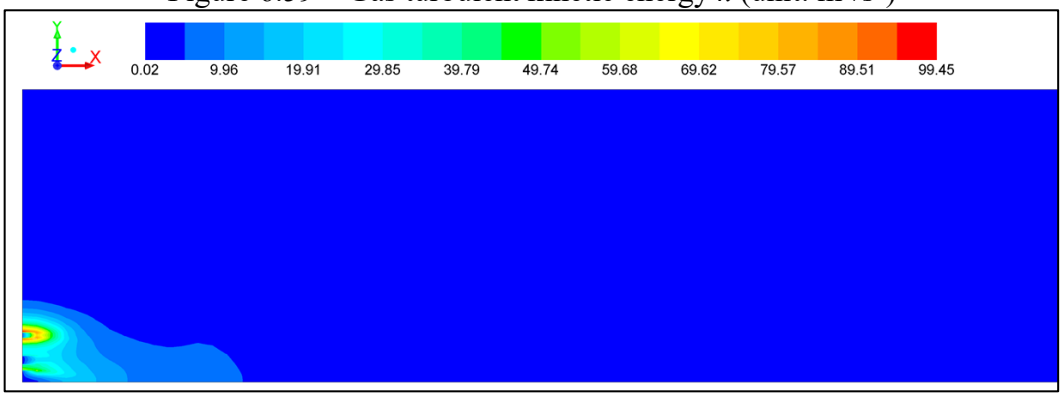

Source: author.

As we can see, there is turbulence only at the reactor near gases inlet. The plot is showing that the reactions are happening at the range where the turbulence time scale is the smallest. It is worth mention the behavior of the volatiles combustion, which is acting on a

small scale since the coal particles realize the volatiles in a position not favorable by the turbulent mixing of the chemical species. At the region where the turbulence time scale is maximum is where the finite rate is at high reacting rates, but the eddy dissipation value is chosen since the model tendency to minimize the overall rate of the reaction. Figure 6.60 and Figure 6.61 illustrate the concept of the minimization of the reaction rate by the model for the volatile homogeneous reaction.

Figure 6.60 – Volatiles eddy dissipation turbulent reaction rate (unit: kmol/m^{3}s)

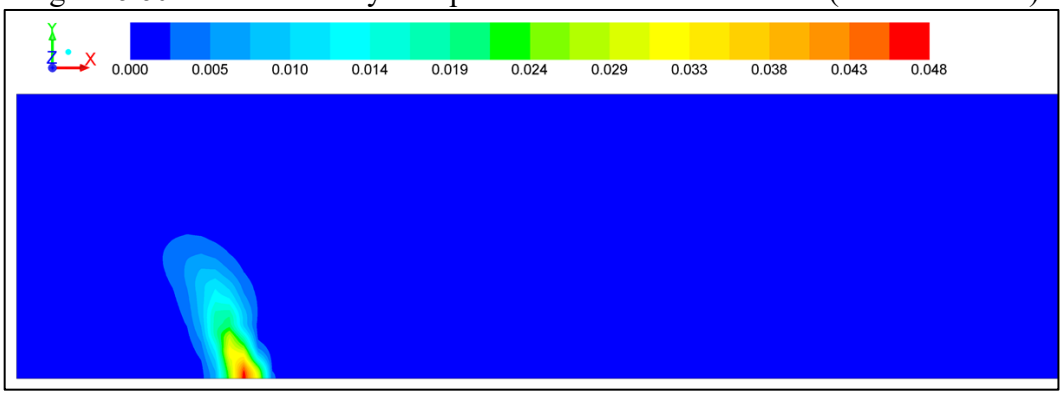

Source: author.

Figure 6.61 – Volatiles finite rate reaction rate (unit: kmol/m^{3}s)

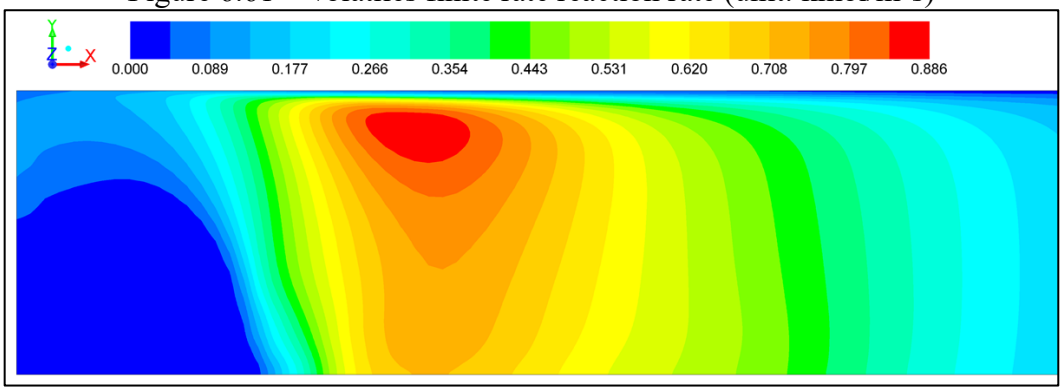

Source: author.

As one can see, the finite rate value of the reaction is high at the regions with low turbulence, and the eddy dissipation is the opposite. The two rates then result in the one reported by Figure 6.56, which is the minimum of the eddy and finite rate values. The other reaction figures were omitted to not extend the discussion.

6.3.3.4 Devolatilization and burnout

The set of analyses will describe the behavior of the coal combustion simulation using parameters well known in the literature: devolatilization and burnout.

However, some assumptions were taken to properly describe the results. The first is the fact that the original experiment did not report any values of the variables in question, which makes the comparison not applicable. Second, is the fact that both variables achieved 100% of efficiency with the reported operating conditions. This result is somewhat not realistic, once several others literature works describe some degree of unburned char and incomplete devolatilization during experiments results. ALGANASH, 2015 reported solid results about the behavior of the mass depredation and burnout of the same experiment done by the present study, but, as already pointed out, it used a particle size distribution different from the original experiment. Therefore, the present study will present the following discussion as a way to support the reaction rate results, the focus of the work.

With the above introduction, Figure 6.62 plots the devolatilization at the symmetry axis of the reactor.

Figure 6.62 – Coal devolatilization at the symmetry axis

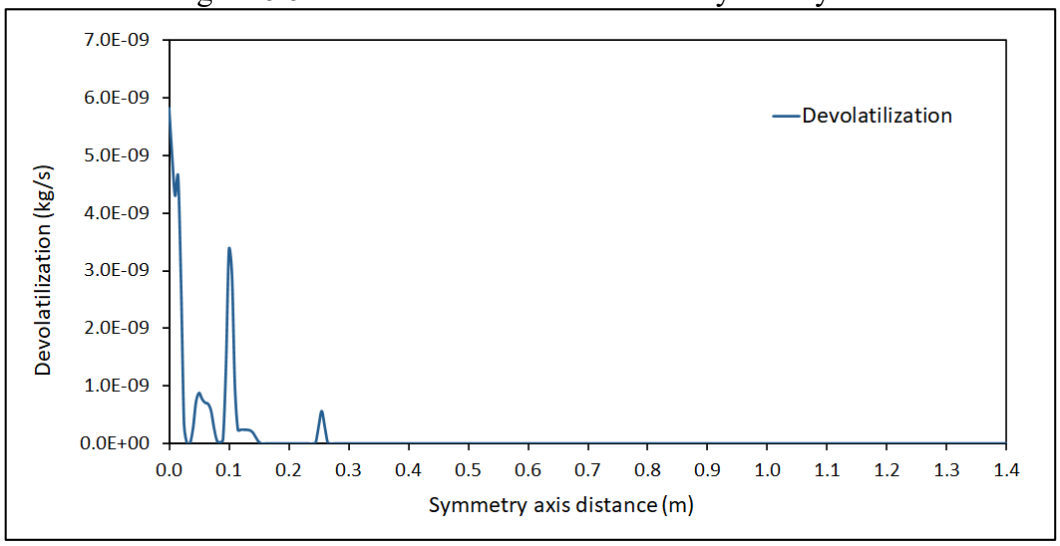

Source: author.

From the devolatilization plot, one can infer that the reaction happens as soon as the coal particles enter the domain, affirmation supported by the particle temperature plot in Figure 6.43, where the particle with 16 and 52 μm are already at the vaporization temperature in a range of 0.1 m inside the domain. After that, the particles with intermediate diameter release their volatiles between the positions 0.2 and 0.3 m. To observe the full phenomenon, Figure 6.64 below is showing the contour map for the devolatilization.

Figure 6.63 – Coal devolatilization rate, kg/s

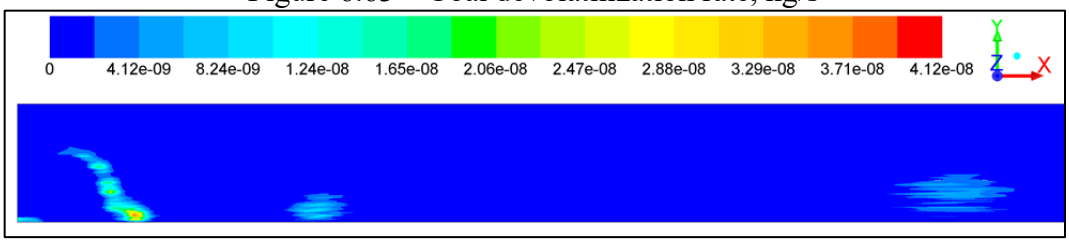

Source: author.

One can observe from the figure that there are three well districting regions where the devolatilization takes place. The volatiles evolution for the coal particles with 350 µm occurs a little above from the symmetry line of the reactor, which is why it did not show on Figure 6.62 plot. To complete the analysis, Figure 6.64 below plots each particle size volatile fraction consumption through the domain.

Figure 6.64 – Coal particles volatile fraction by traveled distance

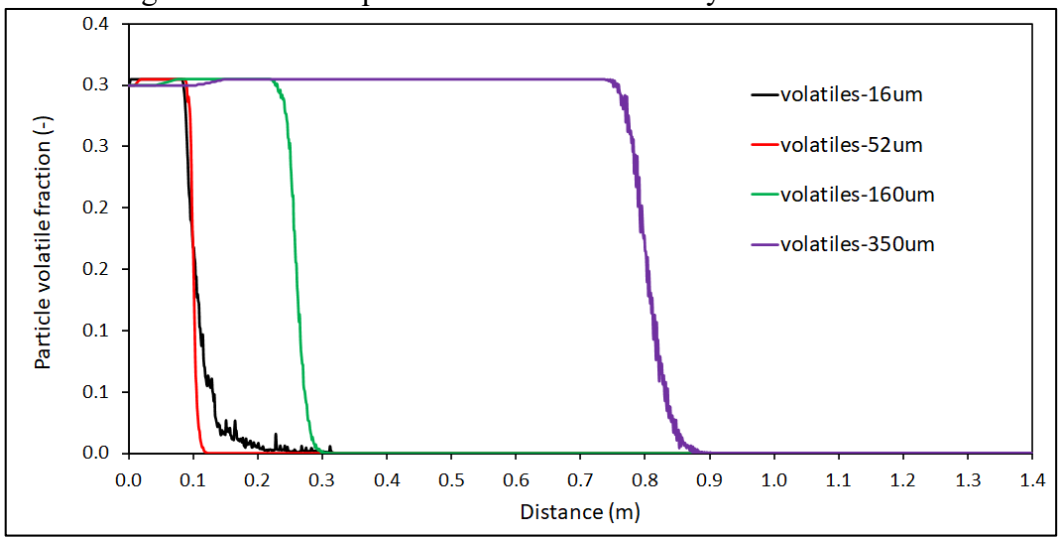

Source: author.

This plot was computed by averaging the variable for all the particles present at that position inside the domain, which is why instead of symmetry axis distance, the *x*-axis was changed to distance. One can see from the plot that the size of the first particles to realize their volatiles are the small ones, followed by the intermediate 160 µm, ending with the larger ones with 350 µm, which is in agreement with the previous results. One can connect the plot with the particle's temperature plot in Figure 6.43, which supports that the volatiles fraction only begins to decrease when the temperature of 1200 K is achieved.

Next, after the devolatilization, the particles proceed to the surface reaction of the char in form of carbon. Figure 6.65 below plots the burnout of the particles in the symmetry axis, on Figure 6.66 the same variable in a contour map plot, and finally the char consumption to each particle size by the traveled distance in Figure 6.67.

Figure 6.65 – Coal burnout at the symmetry axis

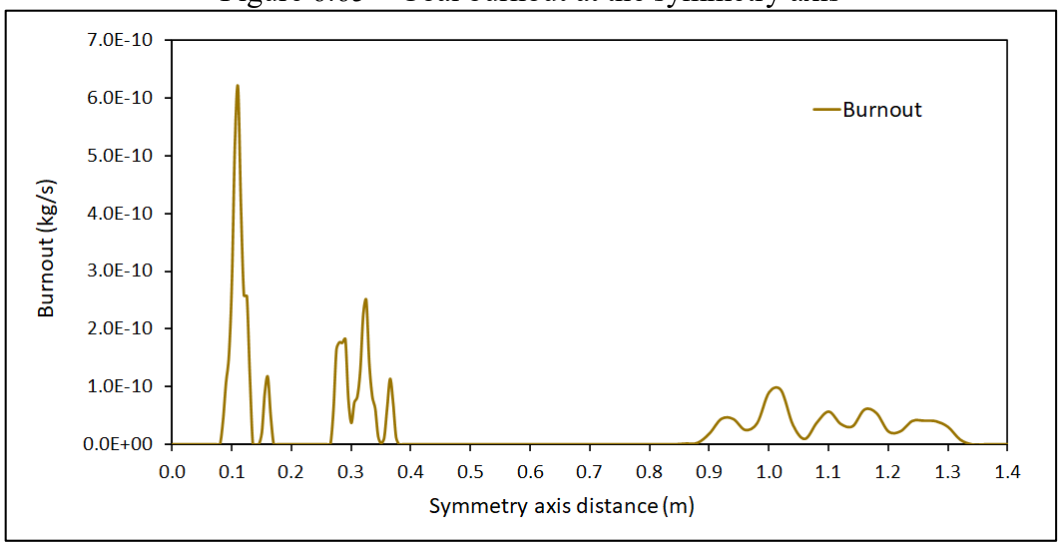

Source: author.

Figure 6.66 – Coal burnout rate, kg/s

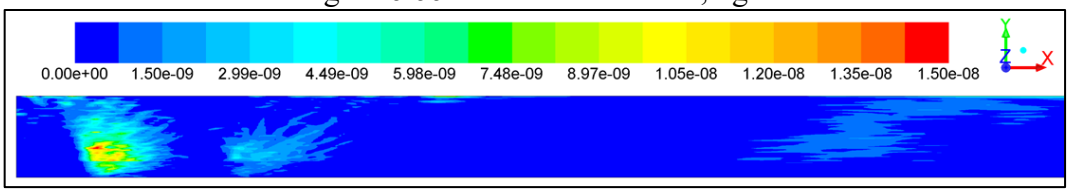

Source: author.

Figure 6.67 – Coal particles char fraction by traveled distance

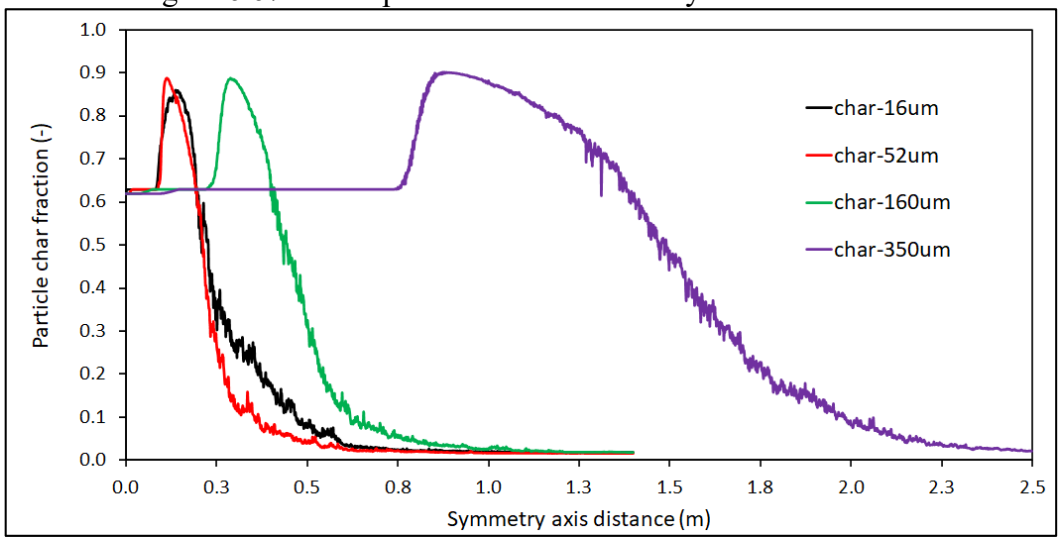

Source: author.

The plot from Figure 6.65 is showing the three spots where the coal particles react, but differently from the devolatilization, the large particle was detected at the symmetry axis line. In Figure 6.66, one can observe that after the devolatilization, on Figure 6.63, at the same position, the particles are burning in a specific shape that scatters the particles into the domain,

projecting them toward the outlet. Finally, in Figure 6.67, we can see that the char fraction first remains constant, increases to then decreasing.

The constant part of the curve is relative to the heating process of the particles. The increase in the char content is relative to the end of the devolatilization process, which is releasing the volatiles and converting the coal surface to composed by char, which in turn is composed of carbon, an assumption of the present study, once all the surface reactions being considered are the ones in which carbon is present. As pointed at the beginning of this section, burnout achieved 100% efficiency, which is reflected in the plot by the char fraction complete depletion by all coal particles size.

6.3.3.5 Reaction rates analysis summary

With the exposed in the following section, one can see all the reaction rates discussed at the symmetric axis, in Figure 6.68 below.

Figure 6.68 – Reaction rates plot for all reactions considered

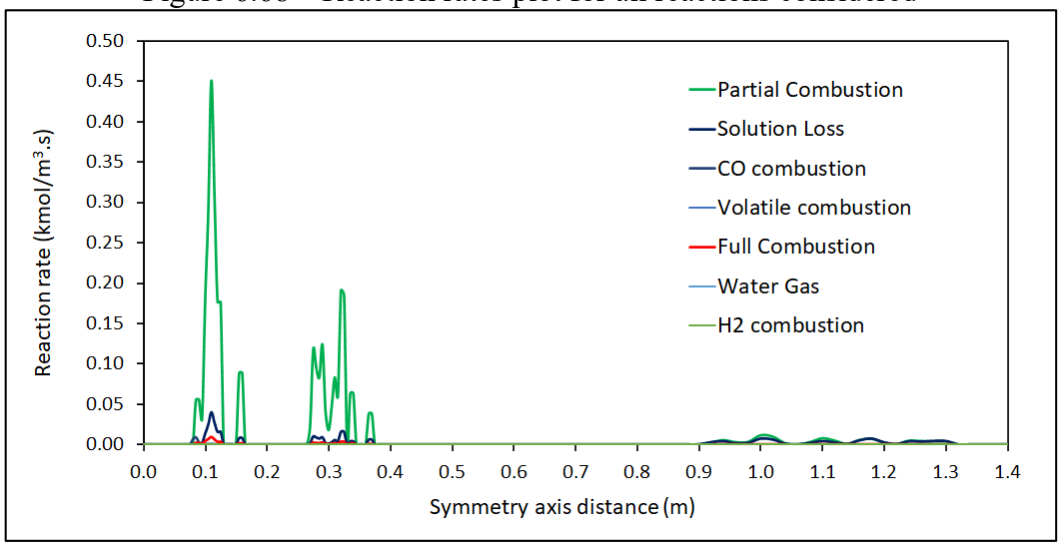

Source: author.

A similar result from the coke combustion analysis, Figure 6.29, with the partial combustion being the reaction with the highest rate obtained. The difference was in the fact that there is a low turbulence environment at the coal combustion experiment, which affected the CO combustion homogeneous reaction, decreasing its value in comparison with the high turbulence result from the coke combustion experiment. The result was the solution loss reaction being in second on the overall rates comparison.

6.4 Reaction rate analysis – blast furnace operation conditions

In this section, the previous models, studied in a segregated way, were united in one simulation using blast furnace operations conditions from a previous work made by WU et al., 2019.

The raceway profile methodology and boundary conditions were described in section § 5.4. The domain initial state is occupied by N_2. Then, the reactions occurred in a transient mode by the flow of the blast through the domain. The analysis will start with the coke and gas-phase reactions, followed by the PCI reactions.

6.4.1 Coke and gas-phase rate reactions

The use of the blast furnace operation conditions, which has a high blast flow rate and oxygen enrichment, is a common practice in the industry. Thus, we can expect that reactions to increase their value, and the ones that have not achieved high rates, as the water-gas heterogeneous reaction, and H_2 combustion, to increase their contribution, which justifies the use of these two reactions in the model.

To begin the analysis, Figure 6.69 below illustrates the first set of chemical species, CO_2, CO, and O_2, and the gas temperature.

Figure 6.69 – Species mole fractions a) CO, b) CO_2, c) O_2, d) gas temperature (K)

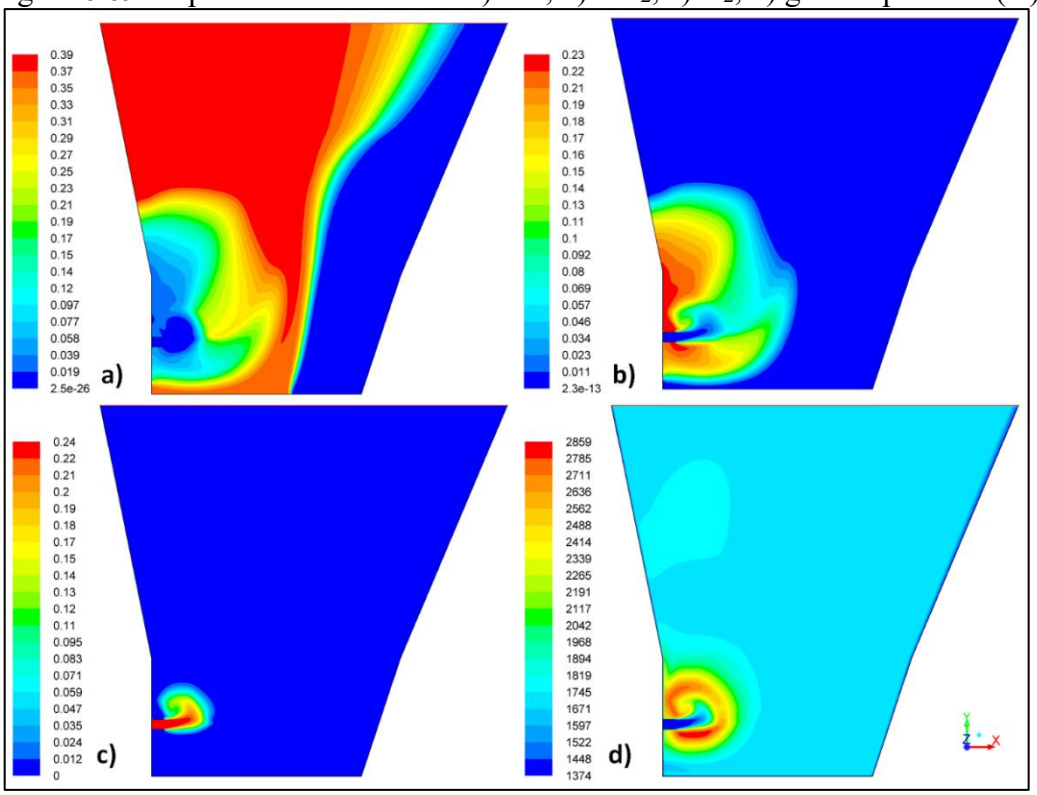

Source: author.

As one can see, the CO mole fraction achieved a similar magnitude, 0.37 to 0.39, to the raceway combustion validation (the mole fraction converted to mass fraction gave a value of 0.39 as well). This value is in agreement with the previous results reported by AUSTIN et al., 1997 and NOGAMI et al., 2004, in which the model developed by DE CASTRO et al., 2011 is based.

The CO_2 mole fraction had an increase, which origin can be tracked by the turbulence, which source was the high flow rate value, that affected the mixture reactions controlled by the eddy dissipation model. The rise in the homogeneous reaction rate increased thermal input that was responsible for the temperature increase at the raceway neighborhood (the homogeneous reaction rate is illustrated in Figure 6.72).

To observe where the reactions are acting on the raceway, Figure 6.70 illustrates the reaction rates in the domain.

Figure 6.70 – Heterogeneous reaction rates, coke, kmol/m^3.s a) Full combustion. b) Partial combustion. c) Water-gas d) Solution loss

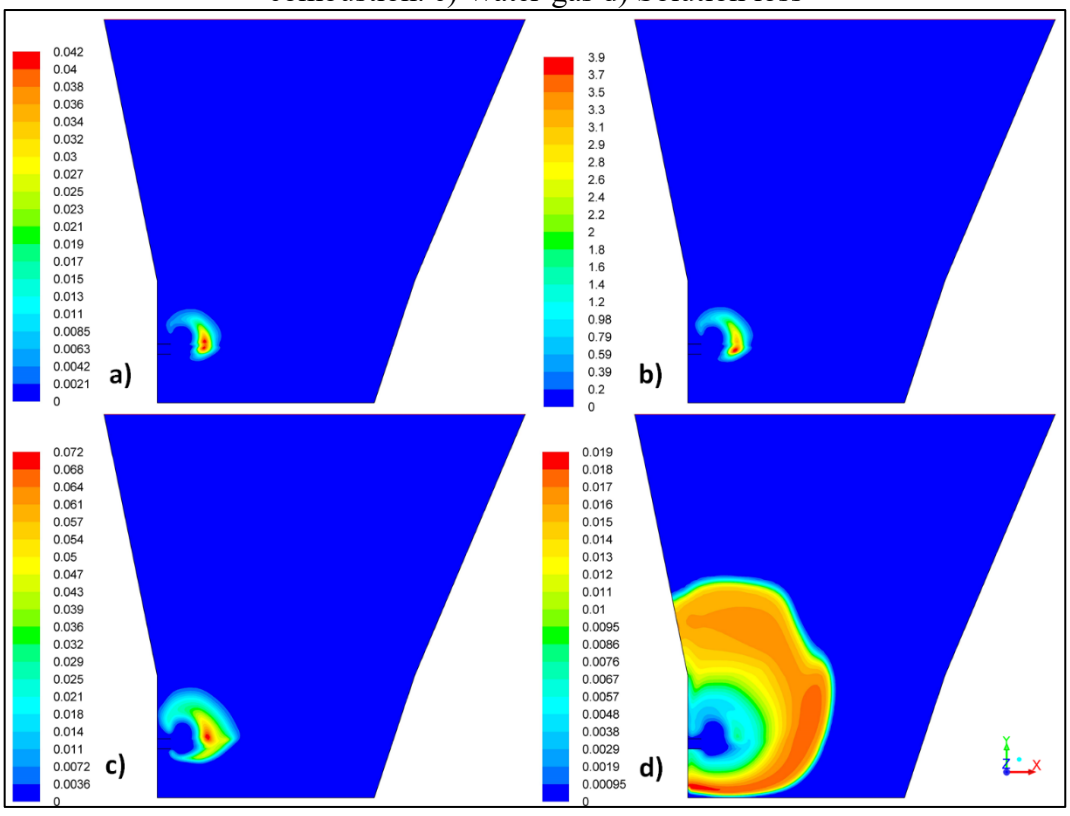

Source: author.

As one can see, the full, partial, and water-gas reaction regions are concentrated at the raceway boundary, where the oxygen from the blast is consumed by the reactions. Different from the previous ones, the solution loss region was expanded to where the CO_2 was produced. The region of action of the reactions was similar to the ones found on the validation.

With the use of blast furnace operation boundary conditions, is interesting to highlight as well the change in the other chemical species. Figure 6.71 below illustrates the mole fraction relative to H_2, H_2O, N_2, and volatiles chemical species.

Figure 6.71 – Species mole fractions a) H_2, b) H_2O, c) N_2, d) Volatiles

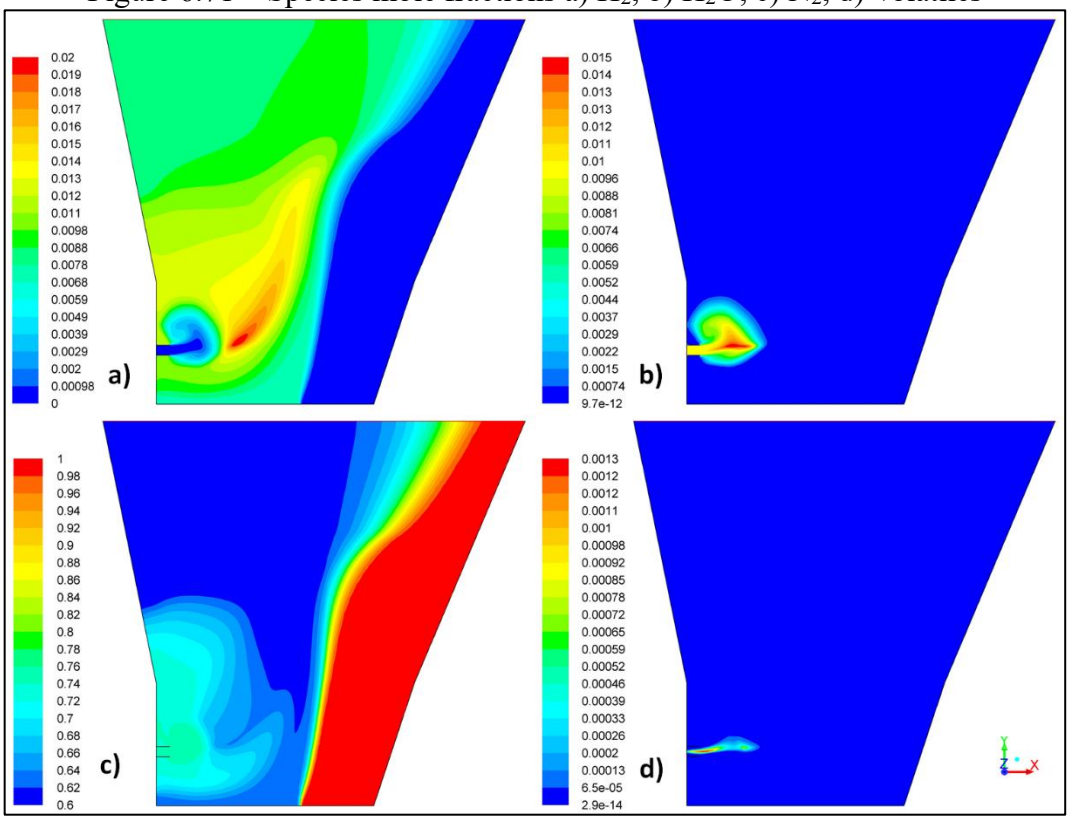

Source: author.

From the figure, one can see H_2 gas species had an increase after the raceway cavity. This is related to the water-gas reaction, from coke, and from the volatiles combustion that was originated by the PCI devolatilization. The devolatilization produces the volatiles, which reacts with the oxygen producing H_2O, which increases the H_2 production, making this reaction more relevant on blast furnace conditions. The N_2 mole fraction is due to the assumption that this gas fills the domain is initially, which shows the preferential path taken by the blast.

Different from experiment conditions, the blast furnace flow rates are very high, which originates gas velocities in the order of 200 m/s. The consequence was the turbulence increase, which is reflected in the homogenous reaction rates. Figure 6.72 illustrates the rates and the gas velocity obtained.

Figure 6.72 – Homogeneous reaction rates kmol/m^3.s a) CO comb. b) H_2 comb. c) Volatile comb. d) gas velocity m/s

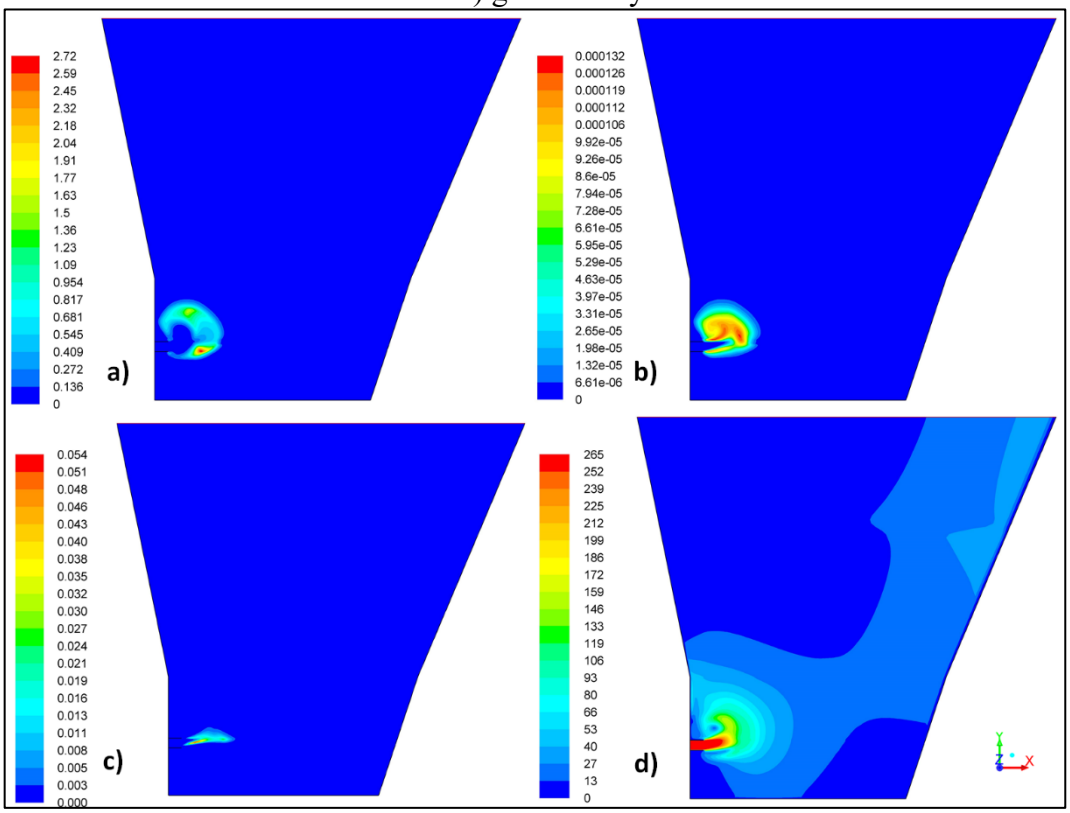

Source: author.

As one can see, the velocity at the tuyere tip reaches values of 265 m/s, and decreases once reaches the raceway boundary. This behavior increases the mixture of the gas species inside the cavity where the oxygen is supplied, increasing the rates when compared to the experiment's validation results. The CO combustion, produced by the partial combustion reaction, contributed to the CO_2 generation, increasing the thermal input.

6.4.2 Pulverized coal rates reactions

Starting the PCI reaction rates analysis, Figure 6.73 illustrates the discrete particle concentration through the domain.

Figure 6.73 – Discrete particle concentration (unit: kg/m^3)

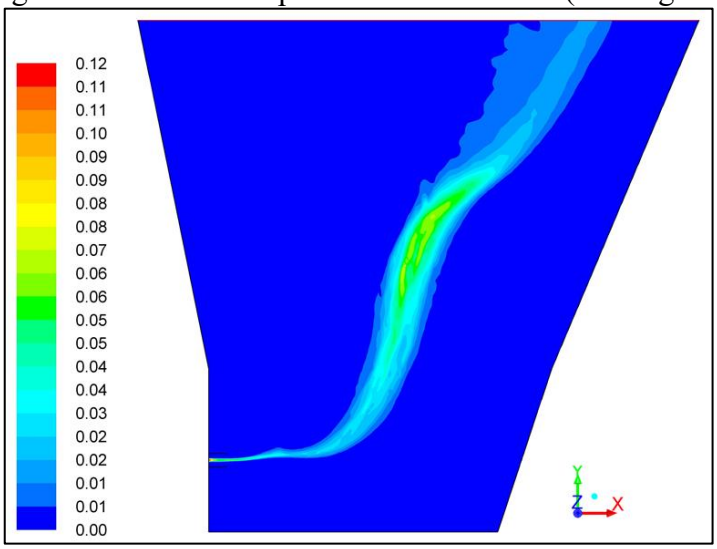

Source: author.

The figure informs the path in which the coal particles are being tracked by the model, from the slot inlet at the tuyere, to the outlet. One can notice that the particles are concentrated until the raceway border region. This effect can be attributed to the gas velocity momentum transfer to the coal particles. Figure 6.74 below plots the coal particle velocity grouped by diameter following the path illustrated by Figure 6.73.

Figure 6.74 – Coal velocity by distance for each particle size

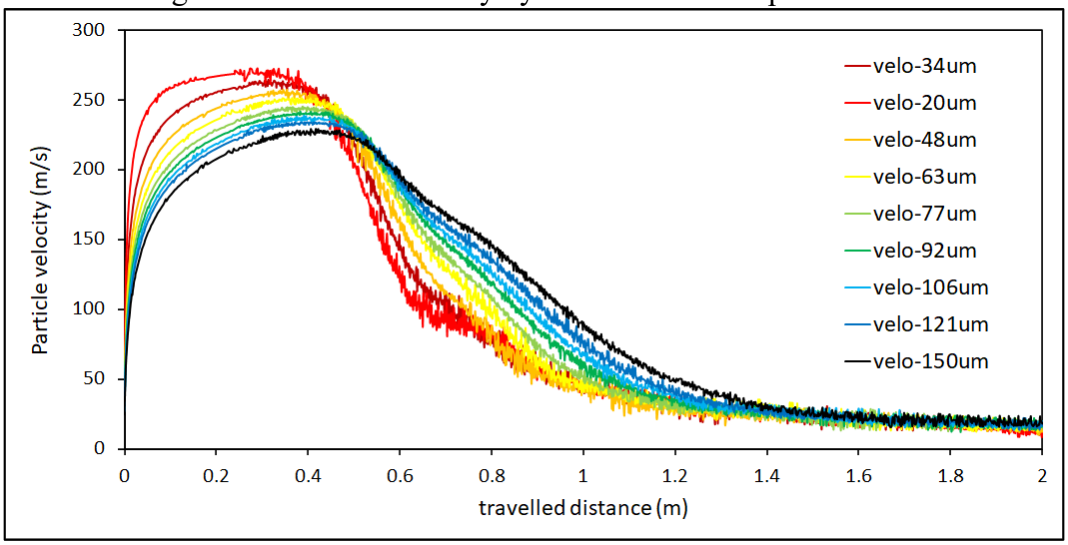

Source: author.

The plot shows that there is a high increase rate in the velocity between 0 and 0.2 meters, followed by a decrease until all the diameters conserve the same velocity. The plot is in agreement with Figure 6.73, where the particles are dragged by the blast until the raceway boundary when the velocity is decreased and they scatter to the outlet

Next, Figure 6.75 illustrates the coal heterogeneous reaction rates.

Figure 6.75 – Heterogeneous reaction rates, PCI, kmol/m^3.s a) Full comb. b) Partial comb. c) Water-gas d) Solution loss

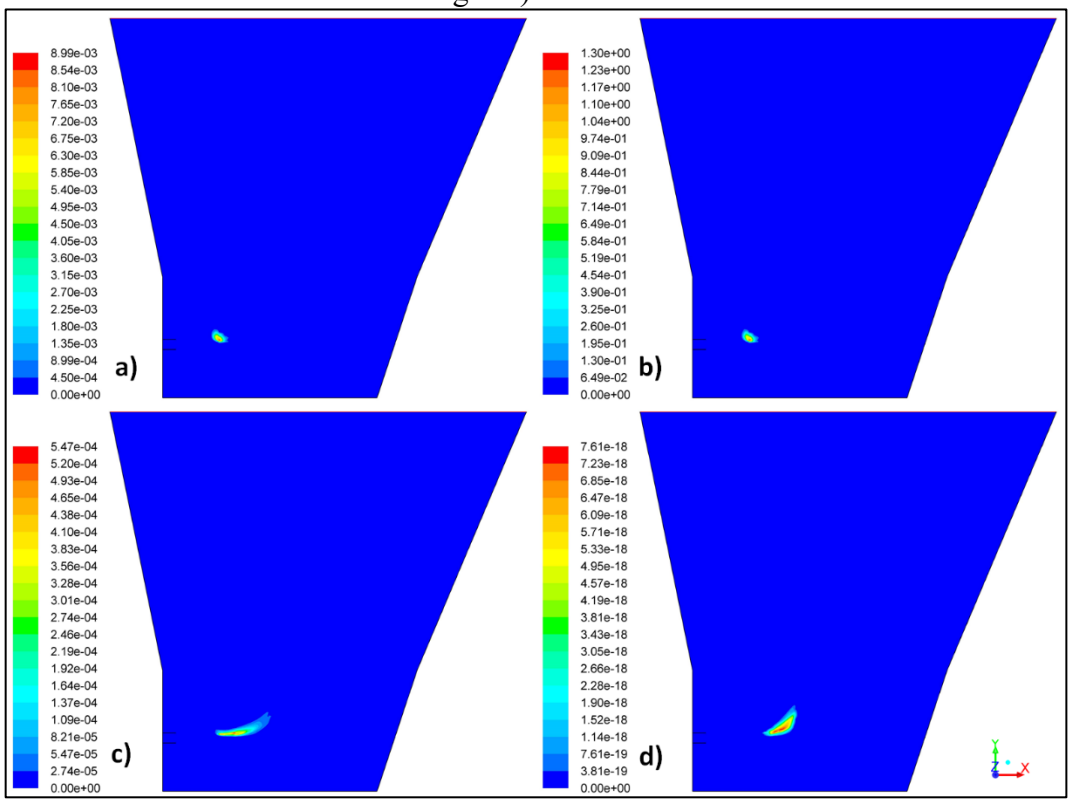

Source: author.

As one can see in the figure, the PCI reactions are located at the raceway level. The full and partial combustions are occurring first, where there is oxygen available in the raceway border, followed by the solution loss, and water-gas which are extended from a small region. As one can see from the values of the rates, partial combustion achieved the highest value among the PCI reactions.

Figure 6.71 d) shows that the volatile molar fraction starts as soon as the coal particles enter the domain, meaning that the devolatilization process is already taken place. Figure 6.76 below plots the volatiles fraction in each coal particle grouped by diameter through the tracked distance.

Figure 6.76 – Coal volatile fraction by distance for each particle size

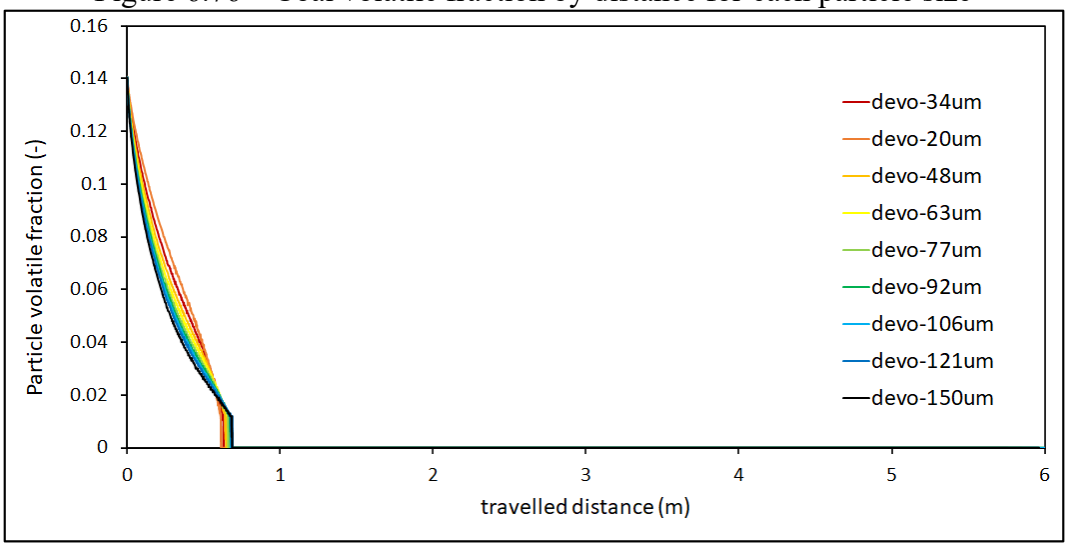

Source: author.

One can see that the devolatilization of all particle sizes presents the same behavior. As it was assumed that the coal particles entered into the domain with the same initial temperature as the blast, 1408 K, the vaporization temperature was already achieved. Figure 6.77 plots the temperature of the particles by grouped by diameter.

Figure 6.77 – Coal temperature by distance for each particle size

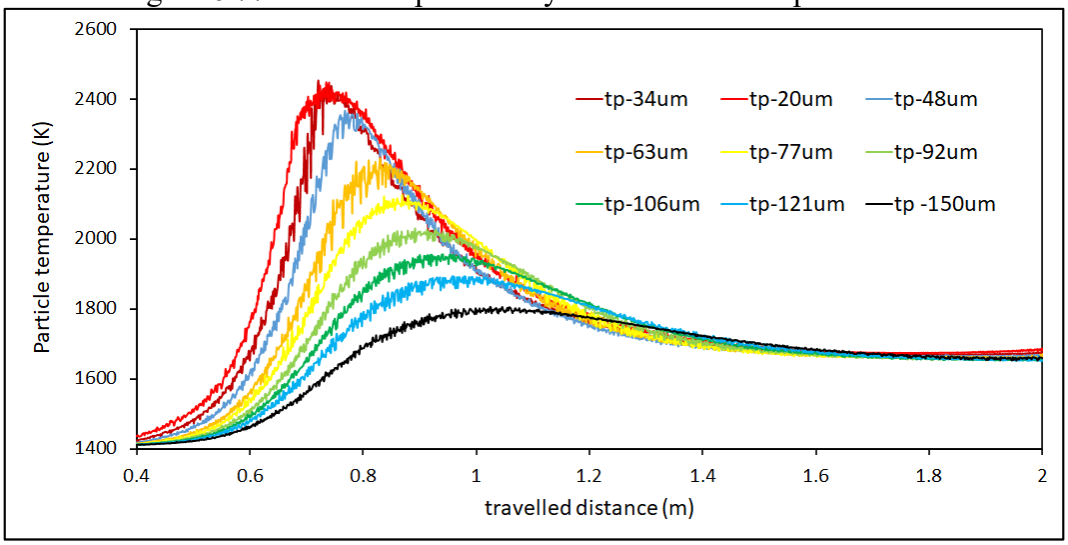

Source: author.

From the plot, one can see that there is a high heating rate in one region, which is where there is oxygen and is inside the raceway cavity. In addition, one can observe that the heating rate is severe affected by the diameter of the particles, where the smallest particles can reach temperatures in an order of 2400 K, decreasing according to the diameter increase. This phenomenon is connected to the velocity of particles, which is too high and does not provide

an appropriate residence time to able to the largest particles to be heated according to the diameter.

After the devolatilization, the particles char content starts to react with the oxygen, and then surface reactions with the carbon start. Figure 6.78 plots the char content by the tracked distance to each particle diameter.

Figure 6.78 – Coal char fraction by distance for each particle size

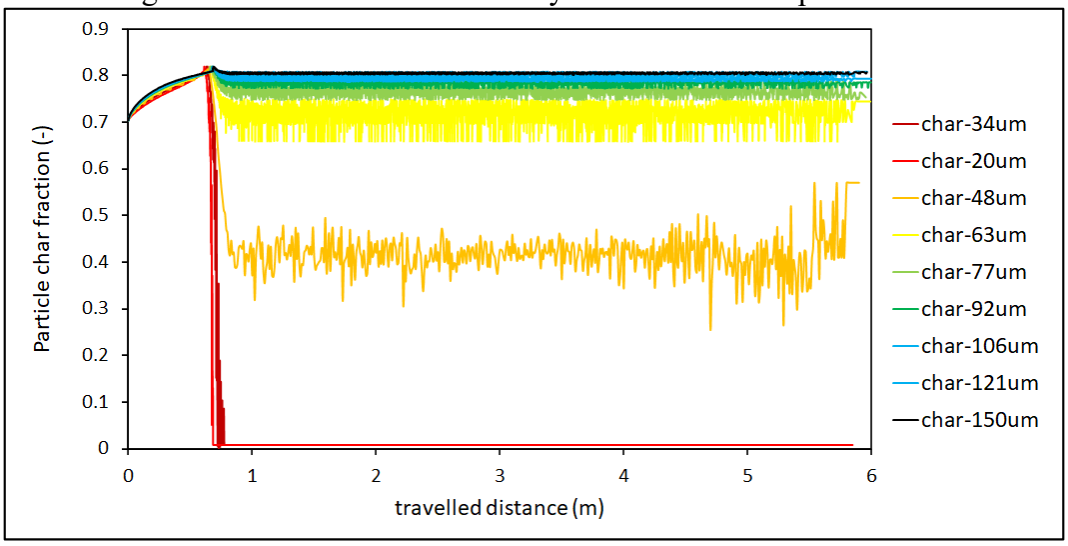

Source: author.

As one can see, there is a clear unburned char fraction at diameters greater or equal to 48 µm, with only the particles with 20 and 34 µm achieving complete burnout. This behavior is attributed to the oxygen consumption at the border of the raceway and the temperature reached by each diameter, as well as the low residence time. The char burnout results obtained are in agreement with the ones obtained by Wu's study, although they lack the details, they show that for particles with a diameter superior to 60 µm, the char burnout rate is severely affected. The summary of the burnout provided by ANSYS-FLUENT for all the particles was that the char content conversion was 57.12 %, with an average residence time of 330 ms.

During the transient simulation, all equations the residuals achieved values in an order of 10^{-5}. Figure 6.79 plots the final iterations residuals for the coke and PCI simulation.

Figure 6.79 – Residuals coke and PCI simulation

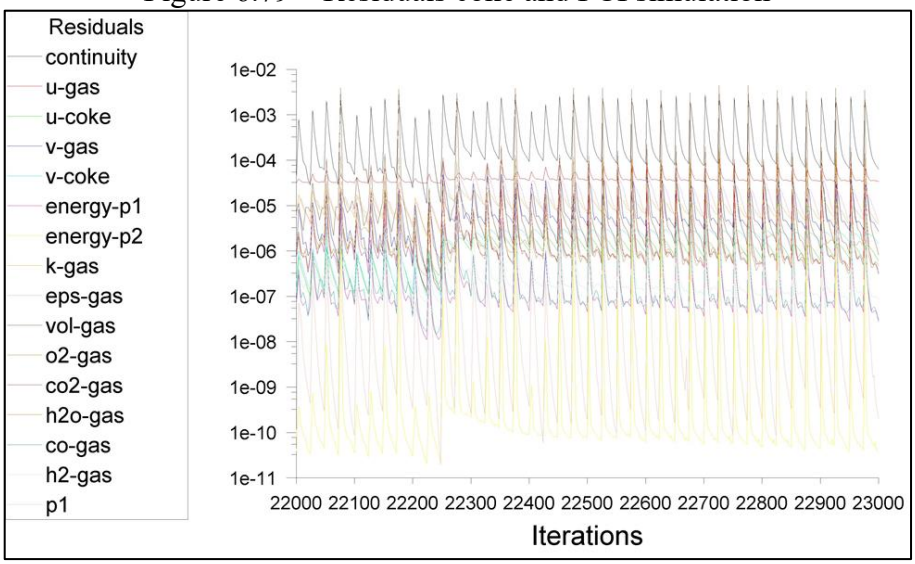

Source: author.

7 CONCLUSIONS

The present study evaluated numerically four research items, (1) the formation of the raceway varying two parameters, coke diameter and gas velocity, (2) applied the methodology of raceway formation to the coke combustion to implement and validate rate equations formulation which considers particles internal structure, (3) adapted the implemented the same reaction rates for coal combustion as well considering different particles diameters, (4) and used the three models in one simulation to evaluate their performance when submitted to blast furnace operation conditions. The conclusions are as follows:

1) The raceway formation was more affected by the diameter variation than by the velocity according to the simulation results. The simulation validation for the 2D case achieved a good fit for both cases.

2) The coke combustion achieved good validation results. The species mole fractions curves were in agreement with the raceway shape formed in terms of the volume fraction which delimited its boundary and dictated the location where the reactions happened. The reaction formulation showed that partial combustion achieved the highest rate followed by CO combustion due to the turbulence.

3) The coal combustion validation results for CO_2 and O_2 mole fractions were in agreement with the experiment results, with the difference that instead of the CO combustion being the second-highest rate as in the coke combustion, the solution loss was due to the low turbulence of the flow. The results were also confirmed in terms of devolatilization and burnout. There were differences in the magnitude of the mole fraction results for coal 2, which were attributed to the char content and particle distribution mass fraction, proving that the model is sensitive to those two variables.

4) When submitted to blast furnace operation conditions, the models performed as expected, following the tendency observed in the previous validation simulations. Partial combustion rate prevailed among the other rates and the velocity effect was observed to increase the CO combustion rate due to the species mixing phenomena at the raceway cavity. The model results were also compared to previous literature studies of the same formulation, proving its

accuracy. As for the Nogami experiment, the reaction region was in agreement with the raceway shape cavity, with the full and partial combustions that depend on the oxygen being confined in the cavity and the solution loss reaction region extension where there is CO_2 available. There was observed an increase in the rate of the water-gas due to the rise of the hydrogen and water chemical species, making this reaction more relevant when submitted to blast furnace conditions. The PCI combustion presented expected results in terms of the reaction rates, but as the simulation assumed simplified conditions to their operation, the results were limited to confirm if the rates are being computed correctly. However, it was possible to observe differences in burnout as the ones reported in the literature on which the operating conditions were based.

As a base study involving indirect variables as the reaction rates, the present model was successful in implement a new combustion model in a commercial software package. The present study concludes that the combustion model equations taken from the literature were possible to be adapted, and now they are even more replicable once they were validated and the commercial software is user-friendly.

The implementation of the formulation that defined the combustion model in a 2D simulation now opens the path for more complex problems using a three-dimensional space, which takes more computational effort to be made.

The present study will be summed to the several studies developed to verify the combustion of coke and coals on experimental and industrial conditions, as a complementary tool to minimize testing costs and a tool to aid decision making.

8 FUTURE WORK

For further improvements, a 3D simulation for the validations could add more reliability and reality to the results.

An extension in the raceway formation method simulating more combinations of velocities with particle diameter variation, and vice versa, could be made to explore the full potential of the methodology. Also, investigate more auxiliary in conjunction with the granular model, as the turbulence interactions.

Perform simulations using a combination of parameters to promote more reliability to the results obtained.

The combustion model could be extended to consider more reactions, as silicon reactions.

A comparison between other combustion models could also be made, once FLUENT has the intrinsic particle combustion model, which considerate the internal structure of the particles.

Investigate the present model using a granular packed bed and a porous media packed bed could also be explored.

Improve the coal model in the blast furnace simulation to consider the details of the PCI lance.

Test the tuyere wall angle, once this could affect the gas flow and consequently the species mixture process.

Study a methodology to integrate the coke consumption with the raceway combustion.

The reaction rate model proposed for the coal combustion simulation could be made for other coals mixtures and also for charcoals.

REFERENCES

ABHALE, P. B.; VISWANATHAN, N. N.; SAXÉN, H. Numerical modelling of blast furnace – Evolution and recent trends. **Mineral Processing and Extractive Metallurgy**, 129, n. 2, p. 166-183, 2020/04/02 2020.

AJILKUMAR, A.; SUNDARARAJAN, T.; SHET, U. S. P. Numerical modeling of a steam-assisted tubular coal gasifier. **International Journal of Thermal Sciences**, 48, n. 2, p. 308-321, 2009/02/01/ 2009.

ALGANASH, B.; PAUL, M. C.; WATSON, I. A. Numerical investigation of the heterogeneous combustion processes of solid fuels. **Fuel**, 141, p. 236-249, 2015/02/01/ 2015.

ALGANASH, B. S. A. **Numerical investigation of the combustion processes of various combustion regimes**. 2015. 255 f. (Ph.D.) - Systems Power & Energy Research Division, University of Glasgow, Glasgow, Scotland.

ANSYS, I. ANSYS Fluent Customization Manual. 2017a.

ANSYS, I. ANSYS Fluent Theory Guide. 2017b.

ANSYS, I. ANSYS Fluent User's Guide. 2017c.

ARTHUR, J. R. Reactions between carbon and oxygen. **Transactions of the Faraday Society**, 47, n. 0, p. 164-178, 1951. 10.1039/TF9514700164.

AUSTIN, P. R.; NOGAMI, H.; YAGI, J.-i. A Mathematical Model for Blast Furnace Reaction Analysis Based on the Four Fluid Model. **ISIJ International**, 37, n. 8, p. 748-755, 1997.

BADZIOCH, S.; HAWKSLEY, P. G. W. Kinetics of Thermal Decomposition of Pulverized Coal Particles. **Industrial & Engineering Chemistry Process Design and Development**, 9, n. 4, p. 521-530, 1970/10/01 1970.

BALTAZAR, A. W. d. S.; CASTRO, J. A. d.; SILVA, A. J. d. Simulação da Combustão de carvão pulverizado em reator tubular nas condições das ventaneiras do Alto-Forno. **Tecnologia em Metalurgia, Materiais e Mineração**, 2, n. 4, p. 7-12, 2006.

BERMUDEZ, A.; FERRÍN, J.; LÓPEZ, O. **Mathematical modelling of pulverized coal furnaces**. Universidade de Santiago de Compostela, 2010.

BRASIL, I. A. **Relatório de Sustentabilidade**. Rio de Janeiro, RJ, p. 84. 2018.

BRASIL, I. A. **Anuário Estatístico**. Rio de Janeiro, RJ, p. 89. 2020.

CASTRO, J. A.; BALTAZAR, A. W. S.; SILVA, A. J. A Three Dimensional Three Phase Reactive FlowFor Simulating The Pulverized Coal Injection IntoThe Channel Of The Blast Furnace Raceway. **WIT Transactions on Engineering Sciences**, 2005.

CAVALIERE, P. **Ironmaking and Steelmaking Processes: Greenhouse Emissions, Control, and Reduction**. Springer International Publishing, 2016. 9783319395296.

DALLAVALLE, J. M. Micromeritics: the technology of fine particles. 1948.

DE CASTRO, J. A.; DA SILVA, A. J.; SASAKI, Y.; YAGI, J.-i. A Six-phases 3-D Model to Study Simultaneous Injection of High Rates of Pulverized Coal and Charcoal into the Blast Furnace with Oxygen Enrichment. **ISIJ International**, 51, n. 5, p. 748-758, 2011.

DE SOUZA BALTAZAR, A. W.; DE CASTRO, J. A.; DA SILVA, A. J. Modelagem e simulação computacional da injeção de carvão pulverizado no canal adutor da "raceway" de altos-fornos. **Estudos Tecnológicos em Engenharia**, 2, n. 2, p. 65-77, 2006.

DOLL, A. **Fitting Rosin-Rammler parameters to a sieve analysis - Calculation Cover Sheet**. 2014. Disponível em: https://www.sagmilling.com/articles?topic=modelling.

FU, D.; ZHENG, D.; ZHOU, C. Q.; D'ALESSIO, J. *et al.* Parametric Studies on PCI Performances. n. 38921, p. T20037-T20037-20010, 2011.

GARSIDE, J.; AL-DIBOUNI, M. R. Velocity-Voidage Relationships for Fluidization and Sedimentation in Solid-Liquid Systems. **Industrial & Engineering Chemistry Process Design and Development**, 16, n. 2, p. 206-214, 1977/04/01 1977.

GEERDES, M.; CHAIGNEAU, R.; KURUNOV, I. **Modern Blast Furnace Ironmaking: An Introduction**. Third Edition ed. IOS Press, 2015. 9781607500407.

GHOSH, A.; CHATTERJEE, A. **Iron Making and Steelmaking: Theory and Practice**. PHI Learning, 2008. 9788120332898.

GOSMAN, A. D.; LOANNIDES, E. Aspects of Computer Simulation of Liquid-Fueled Combustors. **Journal of Energy**, 7, n. 6, p. 482-490, 1983.

GU, M.; CHEN, G.; ZHANG, M.; HUANG, D. *et al.* Three-dimensional simulation of the pulverized coal combustion inside blast furnace tuyere. **Applied Mathematical Modelling**, 34, n. 11, p. 3536-3546, 2010/11/01/ 2010.

GUNN, D. J. Transfer of heat or mass to particles in fixed and fluidised beds. **International Journal of Heat and Mass Transfer**, 21, n. 4, p. 467-476, 1978/04/01/ 1978.

HOU, Q.; LI, J.; YU, A. CFD-DEM Study of Heat Transfer in the Reduction Shaft of Corex. **steel research international**, 86, n. 6, p. 626-635, 2015.

HOWARD, J. B.; WILLIAMS, G.; FINE, D., 1973, **Kinetics of carbon monoxide oxidation in postflame gases**. Elsevier. 975-986.

HOWELL, J. R.; MENGUC, M. P.; SIEGEL, R. **Thermal radiation heat transfer**. CRC press, 2010. 1439894558.

IRANNEZHAD, M. **A numerical study of reacting flows using finite rate chemistry**. Chalmers University of Technology, 2012. 9173857769.

ISHII, K. **Advanced Pulverized Coal Injection Technology and Blast Furnace Operation**. Elsevier Science, 2000. 9780080546353.

JAPAN, T. I. a. S. I. o. **Blast Furnace Phenomena And Modelling**. London: Springer Netherlands, 1987. 550[639] p.

KOBAYASHI, H.; HOWARD, J. B.; SAROFIM, A. F. Coal devolatilization at high temperatures. **Symposium (International) on Combustion**, 16, n. 1, p. 411-425, 1977/01/01/ 1977.

KUANG, S.; LI, Z.; YU, A. Review on Modeling and Simulation of Blast Furnace. **steel research international**, 89, n. 1, p. 1700071, 2018.

LI, A.; AHMADI, G. Dispersion and Deposition of Spherical Particles from Point Sources in a Turbulent Channel Flow. **Aerosol Science and Technology**, 16, n. 4, p. 209-226, 1992/01/01 1992.

LI, Y.; ZHANG, X.; ZHANG, J.; ZHOU, J. *et al.* Numerical simulation and optimization of pulverized coal injection with enriched oxygen into blast furnace. **Applied Thermal Engineering**, 67, n. 1, p. 72-79, 2014/06/01/ 2014.

MA, H. **Numerical Analysis of Raceway Formation and Combustion in a Blast Furnace With Pulverized Coal Injection**. Orientador: ZHOU, C. Q. 2017. 86 f. M.S.M.E. -, Purdue University, Ann Arbor.

MA, L.; JONES, J. M.; POURKASHANIAN, M.; WILLIAMS, A. Modelling the combustion of pulverized biomass in an industrial combustion test furnace. **Fuel**, 86, n. 12, p. 1959-1965, 2007/08/01/ 2007.

MACHADO, J. G. M. S.; OSÓRIO, E.; VILELA, A. C. F.; BABICH, A. *et al.* Reactivity and Conversion Behaviour of Brazilian and Imported Coals, Charcoal and Blends in view of their Injection into Blast Furnaces. **steel research international**, 81, n. 1, p. 9-16, 2010.

MAGNUSSEN, B. F. On the structure of turbulence and a generalized eddy dissipation concept for chemical reaction in turbulent flow. **AIAA, Aerospace Sciences Meeting**, January 01, 1981 1981.

MAGNUSSEN, B. F.; HJERTAGER, B. H. On mathematical modeling of turbulent combustion with special emphasis on soot formation and combustion. **Symposium (International) on Combustion**, 16, n. 1, p. 719-729, 1977/01/01/ 1977.

MAIER, C.; JORDAN, C.; FEILMAYR, C.; THALER, C. *et al.* Multi-scale modeling of hydrocarbon injection into the blast furnace raceway. *In*: 10th International Conference on CFD in Oil & Gas , Metallurgical and Process Industries, 2014, Trondheim, Norway. SINTEF Academic Press, 17-19th June. p. 189-196.

MALISKA, C. R. **Transferência de calor e mecânica dos fluidos computacional (2a. ed.)**. Grupo Gen - LTC, 2017. 9788521633358.

MIYASAKA, N.; KONDO, S.-i. The rate of cokes gasification by gas consisting of CO2, H2O, CO, H2 and N2. **Tetsu-to-Hagané**, 54, n. 14, p. 1427-1431, 1968.

MOJAMDAR, V.; GUPTA, G. S.; PUTHUKKUDI, A. Raceway Formation in a Moving Bed. **ISIJ International**, 58, n. 8, p. 1396-1401, 2018.

MONDAL, S. S.; SOM, S. K.; DASH, S. K. Numerical predictions on the influences of the air blast velocity, initial bed porosity and bed height on the shape and size of raceway zone in a blast furnace. **Journal of Physics D: Applied Physics**, 38, n. 8, p. 1301-1307, 2005/04/02 2005.

MORSI, S. A.; ALEXANDER, A. J. An investigation of particle trajectories in two-phase flow systems. **Journal of Fluid Mechanics**, 55, n. 2, p. 193-208, 2006.

MURAO, A.; FUKADA, K.; SATO, M.; MATSUNO, H. *et al.* Effect of Natural Gas Injection Point on Combustion and Gasification Efficiency of Pulverized Coal under Blast Furnace Condition. **ISIJ International**, 59, n. 12, p. 2165-2173, 2019.

NOGAMI, H.; YAMAOKA, H.; TAKATANI, K. Raceway Design for the Innovative Blast Furnace. **ISIJ International**, 44, n. 12, p. 2150-2158, 2004.

OKOSUN, T. **Numerical Simulation of Combustion in the Ironmaking Blast Furnace Raceway**. Orientador: ZHOU, C. Q. 2018. 169 f. Ph.D. -, Purdue University, Ann Arbor.

OKOSUN, T.; STREET, S. J.; ZHAO, J.; WU, B. *et al.* Influence of conveyance methods for pulverised coal injection in a blast furnace. **Ironmaking & Steelmaking**, 44, n. 7, p. 513-525, 2017/08/09 2017.

OKOSUN, T.; TANG, G.; FU, D.; SILAEN, A. K. *et al.* Numerical Simulation of Raceway Formation in Blast Furnace. *In*: The 7th International Conference on Computational Methods, 2016, California, Berkeley. 2016-05-24. p. 13.

OSBORNE, D. **The Coal Handbook: Towards Cleaner Production: Volume 2: Coal Utilisation**. Elsevier Science, 2013. 9781782421177.

PETERS, N. Premixed burning in diffusion flames—the flame zone model of libby and economos. **International Journal of Heat and Mass Transfer**, 22, n. 5, p. 691-703, 1979/05/01/ 1979.

RAJNEESH, S.; SARKAR, S.; GUPTA, G. S. Prediction of Raceway Size in Blast Furnace from Two Dimensional Experimental Correlations. **ISIJ International**, 44, n. 8, p. 1298-1307, 2004.

RAO, D. V. S. **Minerals and Coal Process Calculations**. CRC Press, Taylor & Francis Group, 2016. 9781138626621.

RAY, S.; GIROUX, L.; MACPHEE, T.; NG, K. W. *et al.* Evaluation of PCI coals in new injection facility at CanmetENERGY-Ottawa. **AISTech - Iron and Steel Technology Conference Proceedings**, 1, p. 926-937, 01/01 2015.

SAFFMAN, P. G. The lift on a small sphere in a slow shear flow. **Journal of Fluid Mechanics**, 22, n. 2, p. 385-400, 1965.

SAFRONOV, D.; RICHTER, A.; MEYER, B. Numerical Predictions of the shape and size of the Raceway Zone in a Blast Furnace. *In*: 12th International Conference on CFD in Oil & Gas, Metallurgical and Process Industries, 2017, Trondheim, NORWAY. SINTEF Academic Press, p. 531-540.

SAZHIN, S. S. Advanced models of fuel droplet heating and evaporation. **Progress in Energy and Combustion Science**, 32, n. 2, p. 162-214, 2006. Review.

SECRETARIA DE GEOLOGIA, M. e. T. M. **Anuário Estatístico: Setor Metalúrgico**. Ministério de Minas e Energia – MME. Brasília/Distrito Federal – Brasil, p. 73. 2019.

SEETHARAMAN, S. **Treatise on Process Metallurgy, Volume 3: Industrial Processes**. Elsevier Science, 2013. 9780080969893.

SELVARASU, N. K.; HUANG, D.; CHEN, Z.; GU, M. *et al.* Prediction of Raceways in a Blast Furnace. n. 47837, p. 297-303, 2006.

SHEN, Y. S.; GUO, B. Y.; YU, A. B.; AUSTIN, P. R. *et al.* Three-dimensional modelling of in-furnace coal/coke combustion in a blast furnace. **Fuel**, 90, n. 2, p. 728-738, 2011/02/01/ 2011.

SHIOZAWA, T. Numerical modelling of multiphase flow in raceway of ironmaking blast furnace. 2013.

SILAEN, A.; WANG, T. Effect of turbulence and devolatilization models on coal gasification simulation in an entrained-flow gasifier. **International Journal of Heat and Mass Transfer**, 53, n. 9, p. 2074-2091, 2010/04/01/ 2010.

SMITH, I. W. The combustion rates of coal chars: A review. **Symposium (International) on Combustion**, 19, n. 1, p. 1045-1065, 1982/01/01/ 1982.

SPALDING, D., 1971, **Mixing and chemical reaction in steady confined turbulent flames**. Elsevier. 649-657.

SYAMLAL, M.; O'BRIEN, T. Computer simulation of bubbles in a fluidized bed. **AIChE Symposium Series**, 85, p. 22-31, 01/01 1989.

THIELE, E. W. Relation between Catalytic Activity and Size of Particle. **Industrial & Engineering Chemistry**, 31, n. 7, p. 916-920, 1939/07/01 1939.

TURKDOGAN, E. T. Blast furnace reactions. **Metallurgical Transactions B**, 9, n. 2, p. 163-179, 1978/06/01 1978.

VEHEC, J. R. **Technology Roadmap Research Program for the Steel Industry**. ; American Iron and Steel Institute, p. Medium: ED; Size: 40 pages, 42,736 KB. 2010.

VERSTEEG, H. K.; MALALASEKERA, W. **An Introduction to Computational Fluid Dynamics: The Finite Volume Method**. Pearson Education Limited, 2007. 9780131274983.

WALKER, W.; GU, M.; D'ALESSIO, J.; MACFADYEN, N. *et al.* Methodology for the Numerical Simulation of Natural Gas, Coal, and Coke Combustion in a Blast Furnace. n. 48494, p. 215-223, 2008.

WIJAYANTA, A. T.; ALAM, M. S.; NAKASO, K.; FUKAI, J. *et al.* Combustibility of biochar injected into the raceway of a blast furnace. **Fuel Processing Technology**, 117, p. 53-59, 2014/01/01/ 2014a.

WIJAYANTA, A. T.; ALAM, M. S.; NAKASO, K.; FUKAI, J. *et al.* Numerical Study on Pulverized Biochar Injection in Blast Furnace. **ISIJ International**, 54, n. 7, p. 1521-1529, 2014b.

WU, D.; ZHOU, P.; YAN, H.; SHI, P. *et al.* Numerical investigation of the effects of size segregation on pulverized coal combustion in a blast furnace. **Powder Technology**, 342, p. 41-53, 2019/01/15/ 2019.

WU, Z. Fundamentals of pulverized coal combustion. 2005.

YU, D.; XU, M.; YU, Y.; LIU, X. Swelling Behavior of a Chinese Bituminous Coal at Different Pyrolysis Temperatures. **Energy & Fuels**, 19, n. 6, p. 2488-2494, 2005/11/01 2005.

ZHANG, Y.; WEI, X.-L.; ZHOU, L.-X.; SHENG, H.-Z. Simulation of coal combustion by AUSM turbulence-chemistry char combustion model and a full two-fluid model. **Fuel**, 84, n. 14, p. 1798-1804, 2005/10/01/ 2005.

ZHOU, C. Q. **CFD Modeling for High Rate Pulverized Coal Injection (PCI) to Blast Furnaces**. American Iron and Steel Institute. Pittsburgh, PA 15220: October 15, 2008, p. 107. 2008.